STUDY OF NOBLE GASES IN LUNAR EXOSPHERE USING THE CHACE-MIP OBSERVATION OF CHANDRAYAAN-1

Thesis submitted to
Cochin University of Science and Technology

In partial fulfillment of the requirements
for the award of

Doctor of Philosophy
in
Physics

UNDER THE FACULTY OF SCIENCES

by

Tirtha Pratim Das

Space Physics Laboratory
Vikram Sarabhai Space Centre
Indian Space Research Organisation
Thiruvananthapuram-695 022
INDIA

December 2016

DECLARATION

This is to declare that the work presented in this thesis has been carried out at the Space Physics Laboratory (SPL), Vikram Sarabhai Space Centre (VSSC), Indian Space Research Organisation (ISRO), Thiruvananthapuram, India, for the award of the degree of Doctor of Philosophy in Physics from the Cochin University of Science and Technology (CUSAT), Cochin, Kerala, India. This thesis is the outcome of the original work done by me and the work did not form any dissertation submitted for the award of any degree, diploma, associateship or any other title or recognition from any University/Institution.

December, 2016
Place: Thiruvananthapuram, India

TIRTHA PRATIM DAS

भारत सरकार
अंतरिक्ष विभाग
विक्रम साराभाई अंतरिक्ष केन्द्र
तिरुवनन्तपुरम-695 022
केरल, भारत
फोन : (0471) 2563663
फैक्स : (0471) 2706535
Mob: +91 9947149290
ई-मेल/Bhardwaj_SPL@yahoo.com
Website: http://SPL.GOV.IN

सत्यमेव जयते

Government of India
Department of Space
Vikram Sarabhai Space Centre
Thiruvananthapuram-695 022
Kerala, INDIA
Telephone : (0471) 2563663
(0471) 2562330 (D)
Fax : (0471) 2706535
e-mail: Anil_Bhardwaj@vssc.gov.in
Mobile : +91-9947149290

अन्तरिक्ष भौतिकी प्रयोगशाला
SPACE PHYSICS LABORATORY

डॉ. अनिल भारद्वाज/Dr. ANIL BHARDWAJ, FNA, FASc, FNASc
निदेशक, एसपीएल/DIRECTOR, SPL

CERTIFICATE

Certified that the thesis titled **Study of noble gases in Lunar exosphere using the CHACE-MIP observation of Chandrayaan-1** submitted by **Mr. Tirtha Pratim Das** (Ph.D. registration number 4181) to Cochin University of Science and Technology, Cochin, embodies the original results of the investigations carried out by him at the Space Physics Laboratory, Vikram Sarabhai Space Centre, Indian Space Research Organisation, Thiruvananthapuram. To the best of my knowledge this thesis is a bonafide record of research carried out by Mr. Tirtha Pratim Das, under my supervision. The work presented in this thesis has not been submitted for the award of any other degree, diploma or associateship to any other University or Institution.

VSSC - SPACE PHYSICS LABORATORY
GOVT. OF INDIA, DEPT. OF SPACE
Thiruvananthapuram-695 022

8/12/2016

अनिल भारद्वाज/Dr. Anil Bhardwaj
(सुपेरवाइसिंग मार्गदर्शक/Supervising Guide)
डॉ.अनिल भारद्वाज/Dr. Anil Bhardwaj
निदेशक/Director
अन्तरिक्ष भौतिकी प्रयोगशाला/Space Physics Laboratory
विक्रम साराभाई अंतरिक्ष केंद्र/Vikram Sarabhai Space Centre
अंतरिक्ष विभाग/Dept. of Space, भारत सरकार/Govt. of India
तिरुवनन्तपुरम/Thiruvananthapuram - 695 022

भारत सरकार
अंतरिक्ष विभाग
विक्रम साराभाई अंतरिक्ष केन्द्र
तिरुवनन्तपुरम-695 022
केरल, भारत
फोन : (0471) 2563663
फैक्स : (0471) 2706535
Mob: +91 9947149290
ई-मेल/Bhardwaj_SPL@yahoo.com
Website: http://SPL.GOV.IN

सत्यमेव जयते

Government of India
Department of Space
Vikram Sarabhai Space Centre
Thiruvananthapuram-695 022
Kerala, INDIA
Telephone : (0471) 2563663
(0471) 2562330 (D)
Fax : (0471) 2706535
e-mail: Anil_Bhardwaj@vssc.gov.in
Mobile : +91-9947149290

अन्तरिक्ष भौतिकी प्रयोगशाला
SPACE PHYSICS LABORATORY

डॉ. अनिल भारद्वाज/Dr. ANIL BHARDWAJ, FNA, FASc, FNASc
निदेशक, एसपीएल/DIRECTOR, SPL

CERTIFICATE

This is to certify that all the relevant corrections and modifications suggested by the audience during the Pre-synopsis seminar and recommended by the Doctoral Committee of **Mr. Tirtha Pratim Das** (PhD. registration number 4181) have been incorporated in the thesis.

8/12/2016

अनिल भारद्वाज/Dr. Anil Bhardwaj
(सुपेरवाइसिंग मार्गदर्शक/Supervising Guide)
डॉ.अनिल भारद्वाज/Dr. Anil Bhardwaj
निदेशक/Director
अन्तरिक्ष भौतिकी प्रयोगशाला/Space Physics Laboratory
विक्रम साराभाई अंतरिक्ष केंद्र/Vikram Sarabhai Space Centre
अंतरिक्ष विभाग/Dept. of Space, भारत सरकार/Govt. of India
तिरुवनन्तपुरम/Thiruvananthapuram - 695 022

DEDICATION

When the Guru and God both stand in front of me, who will I bow to first? Prostrations unto the Guru who bestowed me the path to God!

— *Sant Kabir*

This humble work is dedicated to my revered teachers, who built me with lot of love and care.

ACKNOWLEDGEMENT

Quoting *Guru Granth Sahib*, "Were there to rise a hundred Moons, and a thousand Suns; without the Guru, it will still be pitch darkness.". Despite his faith in the heritage of the Guru-disciple lineage, my Guru, Dr. Anil Bhardwaj, Director, Space Physics Laboratory (SPL), beleives that his disciples have to be self-sufficient, independent, and hence self-luminiscent. I am indebted to him and bow to him for showing me the way to the truth. No word can sufficiently describe his effective mentoring and strong influence on me to pave the way of continuous refinement. As an Internationally acclaimed planetary scientist of his own stature, mentor to numerous gems in this field, Dr. Anil Bhardwaj has been exceptionally kind to have accepted a person like me, with no extra-ordinary virtue, as his doctoral student. If I do not feel the touch of the Almightly in these flow of events, how else do I realize that how blessed am I?

While my Guru has introduced me to the Almighty in the form of joy and beauty to unveil the mysteries of the Universe, I have felt the touch of Almighty throughout my journey through various encouraging and challenging moments, shared with many people in an intricately weaven relationship. I am immensely grateful to all of them.

I am indebted to the Director, Vikram Sarabhai Space Centre (VSSC), ISRO, for granting me kind permission to pursue this doctoral work as a part-time student, registered in the Cochin University of Science and Technology (CUSAT).

My doctoral work is based on the in-situ measurement of the tenuous lunar exosphere using the Chandra's Altitudinal Composition Explorer (CHACE) payload housed in the Moon Impact Probe (MIP) in the Chandrayaan-1 mission (2008). The very idea of sending the impactor to the Moon in the maiden lunar mission of India was the brainchild of late Dr. A.P.J. Abdul Kalam, former President of India, a visionary technologist, who inspired innumerable souls like me. I bow to him for his great vision which facilitaed probing the Moon from close range. The CHACE experiment was the brainchild of Prof. R. Sridharan, the then Director of the SPL, who was also the principal investigator of the CHACE experiment in Chandrayaan-1/MIP mission. I was greatly inspired by him to study the subjects of mass spectrometry and lunar atmosphere during my initial days at SPL. It was Prof. R. Sridharan who showered his blessings on me and had strong faith on my abilities to carry out the project-related activities of time-bound nature leading to the realization of the CHACE payload. I gratefully acknowledge his deep influence on me, without which this thesis would not have materialized. I gratefully remember the affectionate, yet critical mentoring by Dr. K. Krishnamoorthy, ex-Director, SPL during my doctoral journey. Dr. Krishnamoorthy, even after his superannuation from SPL, while handling other scientific and administrative responsibilities in ISRO Head Quarters and later in Indian Institute of Science (IISc), Bangalore, have never forgotten to enquire about the progress of my research. I still feel his blessings in every step of my research. I thankfully recall and acknowledge numerous moments shared and discussions held with Dr. S. Maqbool Ahmed, who was the project manager of the CHACE payload, and currently the Head, Central Instrumentation Laboratory, Central University of Hyderabad.

I am thankful to Shri S V Mohankumar, who was my division head till August 2016, for his affectionate blessings for my doctoral journey. I have no words to express the support I have received from him. My present division head, Dr. K. Rajeev, who is also a member of

my Doctoral Committee, has made me indebted not only by his constant support, but also through his strong faith on my capabilities. In the same context, I fondly remember Late B Manojkumar, my first reporting officer in ISRO, whom I worked with from 2004 to 2006 during my service as a launch vehicle technologist in VSSC's Mechanisms and Vehicle Integration Testing (MVIT) entity. I remember with deep gratitude how much personal interest he used to take to ensure that I enrolled into the doctoral programme. I am sure that his immortal soul is constantly blessing me and giving me enough strength to stand on my own feet, just the way he used to mentor me during my tender years in ISRO. Had I not been fortunate enough to get these God-sent people as my bosses, today this research would not have seen the light of the day.

I take this opportunity to acknowledge the role of the Doctoral Committee for constant monitoring of the progress of this research work and keeping my doctoral journey in track. Gratefully acknowledged are the regular reviews conducted by the Academic Committee of SPL, Doctoral Committee and the CUSAT Research Committee, which ensured that this research brings out the best possible science. I express my deep sense of gratitude to Dr. Radhika Ramachandran, Chairperson, Academic Committee, SPL, for her constant support, blessings, valuable timely suggestions and encouragement. I am grateful to my examiners, viz. Dean of the Facilty of Sciences, CUSAT, Head of the Department of Physics, CUSAT, Prof. T. Rameshbabu, Department of Physics, CUSAT, Dr. George Joseph, VSSC and Dr. A K Anilkumar, VSSC, who spent their valuable time to have evaluated me during the process of my Ph.D. coursework examination.

I thankfully mention the important scientific discussions with Dr. Smitha Thampi, scientist, SPL, on my research topic. She has not only spared her valuable time for scientific discussions, but have also given many valueable suggestions to improve the thesis. The discussions held with Dr. Megha Upendra Bhatt, Research Associate, SPL are thankfully acknowledged for discussions on the origin and evolution of the Moon. Insightful scientific discussions with all my colleagues, especially with Dr. K. Rajeev, Dr. Tarun Kumar Pant, Ms. M B Dhanya, Dr. Prabha Nair, Dr. Geetha Ramkumar, Dr. K. Kishore Kumar, Dr. Suresh Babu, Dr. C Suresh Raju, Dr. Satheesh Thampi, Dr. Vipin K Yadav, Dr. Siddharth Sankar Das, Dr. Damu Bala Subrahamaniyam are gratefully acknowledged. I beg to be condoned for not being able to mention all the names, as the list is quite big. I am also thankful to our Research Fellows Ms. Shreedevi P R, Ms. Vrinda Mukundan, Mr. Abhinaw Alok for various supports. In fact, my each and every colleague from the scientic and engineering fields have their own contributions to enrich me through discussions, critical judgements, strong cooperation and most importantly, emotional cohesion, without which this reasearch would not have bloomed to completeness. They are the source of my inspiration and strength.

At this juncture, I would like to specially mention about Shri Madan Lal, the then Deputy Director of the Launch Vehicle Design Entity (LVDE) of VSSC, who was the first team leader of the MIP project. He ensured that MIP is developed with zero-defect perfection, within the project deadline. As a task master, he used to extract the best from us. Working with him for the MIP project is a cherishable memory of my life. Later, after the superannuation of Shri Madan Lal, Shri Y Ashok Kumar of the Avionics entity of VSSC became the team leader of MIP. Under the able guidance and leadership of Shri Ashok Kumar, MIP was delivered to the Chandrayaan-1 project. I fondly remember both Shri Madan Lal and Shri Ashok Kumar and acknowledge their immense contributions towards

the success of the MIP. It is my pleasure to recall the mathematical discussions on the MIP trajectory with Dr. R V Ramanan, who was with the Applied Mathematics Division of VSSC and is currently at the Indian Institute of Space Science and Technology (IIST). I thankfully mention about my colleagues with whom I have worked for the development of the CHACE instrument: Shri P. Pradeepkumar, Dr. P. Sreelatha, Ms. Supriya Gogulapati, Ms. Neha Naik and Shri Dinakar Prasad Vajja. Most of them, as well as Shri Abhishek J K are the copassangers of my current journey to explore the Martian and lunar exospheres in the Mars Orbiter Mission (MOM) and forthcoming Chandrayaan-2 mission, respectively. I must make special mention of Dr. Raghuram Susarla and Dr. Sonal Jain, who were the doctoral students of my guide, and currently doing active research in the Imperial College, London and Laboratory for Atmospheric and Space Physics (LASP), USA, respectively. Both of them have helped me in many respects during my research when they were in SPL. Dr. Sonal has been helpful to me even after he went aboard for his post-doctoral research.

I am immensely thankful to Dr. Neeraj Srivastava, scientist, Physical Research Laboratory (PRL), Ahmedabad and Ms. Indhu Varatharajan, the then project student working with Dr. Neeraj at PRL, for introducing me to the field of lunar geology during the Structured Training Programme (STP) on planetary exploration organised by ISRO, held at PRL. I am immensely thankful to Prof. S V S Murthy and Prof. S A Haider, PRL and Dr. P. Sreekumar, Director, Indian Institute of Astrophysics (IIA), Bangalore, for scientific discussions in the field of planetary science and instrumentation on several occasions, which helped me to get insight to my field of research. Thanks to the PLANEX programme at PRL, which gave me many opportunities to interact with scientists and technologists as well as students working in the field of planetary sciences. Dr. Bhala Sivaraman, scientist, PRL is fondly acknowledged for his constant encouragement and energizing friendship, which have helped me to love my field of research more passionately.

I hereby acknowledge the insightful scientific discussions on lunar exosphere over e mail with Dr. Richard Hodges, LASP, Colorado, USA and Dr. Dana Hurley, Applied Physics Laboratory, John Hopkins University, USA. Also gratefully acknowledged are the private communications with Dr. Paul Mahaffy, Principal Investigator of the Neutral Mass Spectrometer (NMS) experiment in NASA's LADEE mission to the Moon and Neutral Gas Ion Mass Spectrometer (NGIMS) experiment aboard the MAVEN mission to Mars, who is presently in the Goddard Space Flight Centre, NASA, USA.

I am also thankful to the Administrative Officer, Establishment section, VSSC and his able team for helping me to complete all the formalities during the process of my getting inducted into research. In the course of my doctoral journey, I have received complete cooperation from the SPL office; especially from Ms. P R Suseela, Ms. Sisira and Ms. C Geetha. They have helped me in all administrative matters. Ms. Sisira used to meticulously keep all the records of my research-related matters and also used to keep in touch with CUSAT to make me less bothered about the administrative formalities. The VSSC library has tremendous effect on me. The Head of the Library and Documentation Division and his able team have been regularly sending me updates on my field of research throughout my doctoral journey. I also acknowledge the kind cooperation of the staff of the CUSAT during the entire process of my doctoral work.

I take this opportunity to pay homage to all my teachers who have built me with so much love and care. It is difficult to name all of them here; yet, I choose to name a few of them. I would like to mention about Mr. Ananda Banerjee, who was the librarian at the St.

Lawrence High School, Kolkata, where I have studied till my plus-two standard. He has built my reading habit. Today when I receive the same warmth from Shri Narayanakutty, Head Library, VSSC and Dr. Rajendran, former head of the VSSC library, I remember my quality time spent with Mr. Ananda Banerjee at school library. I was strongly influenced by the moral teachings of late Father Andre Bruylanths, late Father Adrian Wavrail, Father K. Thottam, and many other teachers of the St. Lawrence High School. I fondly remember the contributions of all my teachers who tought me physics and mathematics during my graduate studies in the St. Xavier's College, Kolkata and post-graduate studies in the Institute of Radiophysics and Electronics, University of Calcutta. Especially, I would like to mention the great infleunces of late Dr. Sisir Kumar Bhanja of St. Xavier's College, Kolkata and Dr. Kiranmoy Sengupta of Dinabandhu Andrews College, Kolkata, on me, who unraveled the beauty of Physics to me during my graduation years. I carry within me all of them in my subconscious.

I thankfully acknowledge the contributions of my parents, Shri Tushar Kanti Das and Smt. Sumita Das and my parents in-law Shri Santosh Nandi and Smt. Papia Nandi, for their constant encouragement and especially for having strong faith on my capabilities. My wife Megha has taken the maximum pain; I remember, just after we got married, I was spending days and night in office, in connection with the test and evaluation of the qualification model (QM) of CHACE. She was thousands of kilometers away from her hometown, solely counting on my support, but had to bear with my entries and exits during odd hours of the day. Hats off to her perseverance and cooperation, without which I would not have been able to contribute to the development of CHACE. My son Meghtirtha, who is four years old now, keeps me busy at home, and hence forcefully provides me breaks from my research-related thoughts and anxiety. Hope one day he will understand how greatly he has helped me by doing this, once he grows up and cares to turn the pages of his papa's thesis.

Tirtha Pratim Das

December 2016

Contents

List of Figures

List of Tables

Journal publications

DIRECTLY RELATED TO THESIS

1. **Tirtha Pratim Das**, Smitha V. Thampi, M B Dhanya, Anil Bhardwaj, S M Ahmed and R Sridharan, Upper limit of helium-4 in the sunlit lunar exosphere during magnetotail passage under low solar wind condition: Result from CHACE aboard MIP in Chandrayaan-1, *Icarus*, 297, 189 – 194, doi: 10.1016/j.icarus.2017.07.001, 2017.

2. **Tirtha Pratim Das**., S. V. Thampi, A. Bhardwaj, S. M. Ahmed, and R. Sridharan, Observation of Ne at mid and high latitudes in the sunlit Lunar Exosphere: Results from CHACE aboard MIP/Chandrayaan-1, *Icarus*, 272, 206 – 211, doi: 10.1016/j.icarus.2016.02.030, 2016.

3. Thampi, S.V., R. Sridharan, **Tirtha Pratim Das**, S.M. Ahmed, J.A. Kamalakar, and A. Bhardwaj, The spatial distribution of molecular Hydrogen in the lunar atmosphere New results, *Planetary and Space Science*, 106, 142 – 147, doi: 10.1016/j.pss.2014.12.018, 2015.

4. Sridharan, R., **Tirtha Pratim Das**, S. M. Ahmed, G. Supriya, A. Bhardwaj, and J. A. Kamalakar, Spatial heterogeneity in the radiogenic activity of the lunar interior: Inferences from CHACE and LLRI on Chandrayaan-1, *Advances in Space Research*, 51, 168 – 178, doi: 10.1016/j.asr.2012.08.005, 2013a.

5. Sridharan, R, **Tirtha Pratim Das**, SM Ahmed, and Anil Bhardwaj, Indicators for localized regions of heavier species in the lunar surface from CHACE on Chandrayaan-1, *Current Science*, 105(11), 1470 – 1472, 2013b.

6. Sridharan, R., S. M. Ahmed, **Tirtha Pratim Das**, P. Sreelatha, P. Pradeepkumar, N. Naik, and G. Supriya, Direct evidence for water H_2O in the sunlit lunar ambience from CHACE on MIP of Chandrayaan I, *Planetary and Space Science*, 58, 947 – 950, doi: 10.1016/j.pss.2010.02.013, 2010a

7. Sridharan, R., S. M. Ahmed, **Tirtha Pratim Das**, P. Sreelatha, P. Pradeepkumar, N. Naik, and G. Supriya, The sunlit lunar atmosphere: A comprehensive study by CHACE on the Moon Impact Probe of Chandrayaan-1, *Planetary and Space Science*, 58, 1567 – 1577, doi: 10.1016/j.pss.2010.07.027, 2010b.

8. Ashok kumar, R. V. Ramanan, M. Mohan, B. Sunder, A. Varghese, R. Bagavathiappan, S. Aravamuthan, A. K. A. Samad, K. Ramaswamy, D. Muraleedharan, P. Haridasan, G. Sajitha, Padma, S. Joy, M. J. Lal, K. K. Mukundan, G. SunilKumar, S. R. Biju, B. S. SureshKumar, Rajendran, V. Murugesan, Reshmi, S. Chatterjee, M. Manohar, G. Murali, S. Raghavendran, M. Kalavathi, A. S. K. Kumar, S. A. Kuriakose, S. Paul, A. Verma, R. Sridharan, S. M. Ahmed, P. Sreelatha, **Tirtha Pratim Das**, P. P. Kumar, G. Supriya, and Neha Naik, The Moon Impact Probe on Chandrayaan-I, *Current Science*, 96(4), 540 – 543, 2009.

OTHER PUBLICATIONS

1. Bhardwaj, A., S. V. Thampi, **Tirtha Pratim Das**, M. B. Dhanya, N. Naik, D. P. Vajja, P. Pradeepkumar, P. Sreelatha, J. K. Abhishek, R. S. Thampi, V. K. Yadav, B. Sundar, A. Nandi, G. P. Padmanabhan and A.V. Aliyas, Observation of suprathermal argon in the exosphere of Mars, *Geophysical Research Letters*, 44(5), 2088–2095, doi:10.1002/2016GL072001, 2017

2. Bhardwaj, A., S. V. Thampi, **Tirtha Pratim Das**, M. B. Dhanya, N. Naik, D. P. Vajja, P. Pradeepkumar, P. Sreelatha, G. Supriya, J. K. Abhishek, S.V. Mohankumar, R. S. Thampi, V. K. Yadav, B. Sundar, A. Nandi, G. P. Padmanabhan and A.V. Aliyas, On the evening time exosphere of Mars: Result from MENCA aboard Mars Orbiter Mission, *Geophysical Research Letters*, 43(5),1862 – 1867, doi:10.1002/2016GL067707, 2016

3. Bhardwaj, A., S. V. Mohankumar, **Tirtha Pratim Das**, P. Pradeepkumar, P.Sreelatha, B. Sundar, A. Nandi, D. P. Vajja, M. B. Dhanya, N. Naik, G. Supriya, R. S. Thampi, G. P. Padmanabhan, V. K. Yadav, A. V. Aliyas, MENCA Experiment aboard India's Mars Orbiter Mission, *Current Science*, 109 (6), 1106 – 1113, doi: 10.18520/v109/i6/1106-1113, 2015

Presentations in Conferences/Workshops/Symposia

1. **Tirtha Pratim Das**, The lunar neutral exosphere and the CHACE-2 experiment aboard Chandrayaan-2 orbiter, Planex workshop on "Exploration of inner solar system objects", at PRL, Ahmedabad, 7-10 March, 2016, **(Invited lecture)**

2. **Tirtha Pratim Das**, MENCA data structure and analysis procedure, Mars Data Analysis (MDA) workshop, organised by ISRO-NASA Mars Working Group (INMWG), at ISRO Head Quarters, 23-25 February, 2016, **(Invited lecture)**

3. **Tirtha Pratim Das**, Smitha V. Thampi, Anil Bhardwaj, S .M. Ahmed, R. Sridharan, Distribution of neutral Ne-20 in the sunlit lunar exosphere, National Space Science Symposium, at VSSC, Trivandrum, 9-12 February 2016

4. Anil Bhardwaj, **Tirtha Pratim Das**, S.V. Mohankumar, Smitha V. Thampi, P. Pradeepkumar , P. Sreelatha, B. Sundar, Amarnath Nandi, Dinakar Prasad Vajja, M.B. Dhanya, Neha Naik, G. Supriya, R. Satheesh Thampi, G.Padma Padmanabhan, Vipin K. Yadav, A.V. Aliyas, Abhishek J K, CHACE-2 mass spectrometer aboard Chandrayaan-2 orbiter to study the lunar neutral exosphere, National Space Science Symposium,at VSSC, Trivandrum, 9-12 February 2016

5. **Tirtha Pratim Das**, MENCA aboard Mars Orbiter Mission, MOM data analysis workshop, at Physical Research Laboratory, Ahmedabad, 4-5 September, 2015, **(Invited lecture)**

6. **Tirtha Pratim Das**, MENCA experiment aboard the Mars Orbiter Mission, 20th National Conference on Atomic and Molecular Physics (NCAMP-20), at Indian Institute of Space Science and Technology, Trivandrum, 9-12 December, 2014.

7. **Tirtha Pratim Das**, MENCA experiment aboard the Mars Orbiter Mission: Science, Technology and Observations, Workshop on Mars Orbiter Mission: Data analysis and science plan, at Physical Research Laboratory, Ahmedabad, 20-21 August, 2014, **(Invited lecture)**

8. Anil Bhardwaj, S.V. Mohankumar, P. Sreelatha, P. Pradeepkumar, B. Sunder, **Tirtha Pratim Das**,Amarnath Nandi, Neha Naik, G. Supriya, R. Satheesh Thampi, G. P. Padmanabhan, Vipin K. Yadav, M. B. Dhanya, and A.V. Aliyas, An Orbiter-based in situ Study of the Lunar Exosphere : the CHACE-2 Experiment aboard Chandrayaan-2, National Space Science Symposium, 29 January - 1 February, 2014

9. **Tirtha Pratim Das**, Past and Future of the planet Earth : Do our neighbour planets have the clue ? National Seminar on Impact of Global Warming and Climate Change (at Christ University, Trivandrum Campus,22- 23 February 2013, **(Invited lecture)**

10. **Tirtha Pratim Das**, Anil Bhardwaj, R. Sridharan, S.M. Ahmed, S V Mohankumar, " Study of Lunar Atmosphere by CHACE aboard Chandrayaan-1: A Follow-up by The CHACE-2 onboard Chandrayaan-2, 39th COSPAR Scientific Assembly, at Mysore, India, 14-22 July 2012

11. R. Sridharan, **Tirtha Pratim Das**, S.M.Ahmed, Gogulapati Supriya, Anil Bhardwaj andJ.A. Kamalakar, Observations on possible spatial heterogeneity of lunar radiogenic activity by CHACE and its casual relation to lunar surface topography as measured by LLRI : Results from Chandrayaan-1; 17th National Space Science Symposium 2012 (NSSS2012), at SV University, Tirupati, 14th-17th February, 2012

12. **Tirtha Pratim Das**, Development of instruments for space applications, delivered at Challenges in Space Science Engineering [CSSE 2012], at Manipal University, 27th - 28th Jan 2012, **(Invited lecture)**

13. **Tirtha Pratim Das**, Dry Moon, Wet Moon : The story of discovery of water on Moon, delivered at Challenges in Space Science Engineering [CSSE 2012], at Manipal University, 27th - 28th Jan 2012, **(Invited lecture)**

14. **Tirtha Pratim Das**, Importance of Lunar research for the benefit of mankind : A long-term perspective; delivered at the National Energy Parliament, Priyadarshini Science and Technological Museum, Trivandrum, on 30 December, 2011, **(Invited lecture)**

15. R. Sridharan, **Tirtha Pratim Das**, S.M.Ahmed, Gogulapati Supriya, Anil Bhardwaj, Results from the CHACE Experiment in the MIP Chandrayaan-1; PLANEX Decadal Conference cum 07th Chandrayaan-1 Science Meet, at Physical Research Laboratory, Ahmedabad 12-14 December, 2011

16. **Tirtha Pratim Das**, Prasanna Mahavarkar, Gogulapati Supriya, Satheesh Thampi, P. Sreelatha, P. Pradeepkumar, Neha Naik, S V Mohankumar and Anil Bhardwaj, Accurate estimation of the total pressure using a mass spectrometer below the X-ray limit, International Conference on Innovative Science and Engineering Technology (ICISET 2011), at VVP Engineering college, Rajkot, 8-9 April, 2011

17. **Tirtha Pratim Das**, Gogulapati Supriya, Prasanna Mahavarkar, P. Sreelatha, P. Pradeepkumar, S V Mohankumar, Anil Bhardwaj and R Sridharan, Study on the water vapour desorption rate from space-borne mass spectrometers under simulated deep space vacuum, International Conference on Innovative Science and Engineering Technology (ICISET 2011), at VVP Engineering college, Rajkot, 8-9 April, 2011

18. **Tirtha Pratim Das**, In-situ study of the Martian upper atmosphere using neutral mass spectrometer, Brainstorming session on the exploration of Mars, at Physical Research Laboratory, Ahmedabad, 24 March 2011

19. **Tirtha Pratim Das**, Planetary exploration using rovers, at PLANEX workshop on 'Exploration of Mars and Moon', organised by Physical Research Laboratory, Ahmedabad, 3-7 January, 2011, **(Invited lecture)**

20. **Tirtha Pratim Das**, CHACE: In search of the lunar atmosphere, National Workshop on Atmospheric and Space Sciences (NWASS), University of Calcutta, 23-24 November, 2010, **(Invited lecture)**

21. **Tirtha Pratim Das**, CHACE in Moon Impact Probe on Chandrayaan 1 Mission, at COSPAR Capacity Building Workshop 2009: Planetary and Surface Sciences, at Harbin, China, on 17 September, 2009, **(Invited lecture)**

Acronyms

ALSEP	Apollo Lunar Surface Experiment Package
amu	Atomic Mass Unit
ARTEMIS	Acceleration, Reconnection, Turbulence and Electrodynamics of Moon's Interaction with the Sun
AS	Active Sun
AU	Astronomical Unit
B/A Gauge	Bayard-Alpert Gauge
CEM	Channel Electron Multiplier
CENA	Chandrayaan-1 Energetic Neutral Analyzer
CHACE	CHandra's Altitudinal Composition Explorer
CHACE-2	CHandra's Atmospheric Composition Explorer
DC	Direct Current
EMC	Electro Magnetic Compatibility
EMG	Electron Multiplier Gain
EMI	Electro Magnetic Interference
ENA	Energetic Neutral Atom
ESA	Electro Static Analyser
ETLS	Environmental Test Level Specifications
FC	Faraday Cup
FAT	Flight Aceptance Test
FWHM	Full Width at Half the Maximum
GRAIL	Gravity Recovery and Interior Laboratory
GSE	Geocentric Solar Ecliptic (Coordinate system)
HK	House Keeping
IBEX	Interstellar Boundary Explorer
IDSN	Indian Deep Space Network
IEA	Ion Energy Analyzer
IMA	Ion Mass Analyzer
IMF	Interplanetary Magnetic Field
IPD	Inter Planetary Dust
ISRO	Indian Space Research Organisation
KREEP	Potassium (K), Rare Earth Elements (REE) and Phosphorus (P)
LACE	Lunar Atmospheric Composition Experiment
LADEE	Lunar Atmospheric and Dust Environment Explorer
LAMP	Lyman Alpha Mapping Project
LCROSS	Lunar Crater Observation and Sensing Satellite
LExS	Lunar Exospheric Simulation (toolkit)
LHB	Late Heavy Bombardment
LISM	Local Inter Stellar Medium
LLRI	Lunar Laser Ranging Instrument
LMO	Lunar Magma Ocean
LOLA	Lunar Orbiter Laser Altimeter

LRO	Lunar Reconnaissance Orbiter
MAP	MAgnetic field and Plasma experiment
ME	Mean Earth (Coordinate system)
MIP	Moon Impact Probe
MTU	MIP Telemetry Unit
NAIF	Navigation and Ancillary Information Facility
NASA	National Aeronautics and Space Administration
NIST	National Institute of Standards and Technology
NMS	Neutral Mass Spectrometer
PACE	Plasma energy Angle and Composition Experiment
PAS	Photon Assisted Sputtering
PDA	Peak Detection Algorithm
PES	Potential Energy Surface
PFTBA	Per Fluoro Tri Butyl Amine
PSD	Photon Stimulated Desorption
PSR	Permanently Shadowed Region
QMA	Quadrupole Mass Analyzer
QMD	Quadrupole Mass Discrimination
QS	Quiet Sun
RA	Radar Altimeter
RF	Radio Frequency
SARA	Sub-KeV Atom Reflecting Analyzer
SBE	Surface Boundary Exosphere
SELENE	SElenological and Engineering Explorer
SPL	Space Physics Laboratory
SRC	Standard Room Conditions
SSDR	Solid State Data Recorder
SWID	Solar Wind Ion Detector
SWIM	Solar WInd Monitor
SZA	Solar Zenith Angle
UBT	UHF Band Transmitter
UHF	Ultra High Frequency
UTC	Coordinated Universal Time

Symbols

Δm	Full Width at Half the Maximum of a mass peak
Φ_0	Potential applied at the quadrupole rods
Φ_j	Thermal escape flux
$\Phi(x, y)$	Quadrupole potential energy surface
λ_{esc}	Escape parameter
ψ	Solar Zenith Angle
ω_p	Characteristic frequency of an ion
ω	Radio frequency applied at the quadrupole rods
θ	Colatitude
ϕ	subsolar longitude
$\dot{a},\ \ddot{a}$	Single and double time derivatives of a
e^-	electron
$\overrightarrow{E}$	Quadrupole electric field
G	Universal gravitational constant
H	Hamiltonian of an exospheric atom under the gravitational influence of a planet
i_2	molecule
i, j	atoms
i^+, j^+	ions
k	Boltzmann's constant
L_{E-M}	Angular momentum of the Earth-Moon system
m	Mass of a species
M_p	Mass of a planetary body
N_{ex}	Number density at the exobase
(p_i, q_i)	Generalized coordinates in the phase space
q	Electronic charge
r_0	Radius of the in-circle in the quadrupole mass analyzer
R	Radius of a celestial body
superscript *	represents energetic atom or molecule
T	Kinetic temperature of species, also lunar surface temperature
T_c	Temperature at the exobase
T_{scan}	Time to scan a mass range
U	DC component of the quadrupole potential
V	RF component of the quadrupole potential
v_{escape}	Escape velocity
v	Thermal velocity
$\bar{v_0}$	Most probable velocity
x, y	Position coordinates in Cartesian system
z	Arbitrary altitude

Preface

The atmosphere of the Earth's Moon is so tenuous that the gas atoms hardly collide, rendering it to the category of exosphere. An exosphere is the outermost region of any planetary atmosphere, where the mean free path between gas atoms and molecules exceeds the local scale height. The lunar exosphere is bounded on one side by its surface, and extend to thousands of kilometers before it merges with the interplanetary medium. This makes Moon a typical example of a Surface Boundary Exosphere (SBE) in the solar system. As an airless and globally non-magnetized obstacle to the torrents of photons and solar wind particles, Earth's Moon is a natural laboratory to study the interaction of Sun with the SBEs in the solar system. The lunar exosphere is a repository of a wealth of information about the lunar surface, interiors as well as different physical processes operative on the Moon.

The lunar exosphere is a result of the dynamic equilibrium between several source (influx of solar material, internal release, delivery from meteoritic bombardment) and sink (gravitational escape, ion escape, condensation loss) processes (*Stern*, 1999), as well as recycling of its constituents in the lunar surface (*Manka and Michel*, 1971). The lunar exosphere is also known to be highly variable, revealing a strong diurnal cycle (*Hodges*, 1975; *Benna et al.*, 2015) and responds promptly to the fluctuations in the solar wind flux (*Hurley et al.*, 2016). The lunar exosphere is also affected by the passage of the Moon through the Earth's magnetotail (*Wilson et al.*, 2006; *Colaprete et al.*, 2016) and meteoroid systems (*Colaprete et al.*, 2016).

The lunar atmosphere is known to weigh only about $\sim 10^7$ g (*Stern*, 1999). A typical lunar lander module releases commensurate material in the form of exhaust gases to the lunar exosphere. As for example, each Apollo lunar landing module had deposited rocket exhaust and spacecraft effluents totaling about 0.2 lunar atmosphere mass, which took few ionization timescales (few Earth-months) to get lost from the lunar atmosphere (*Vondrak*, 1988). Till date, several lunar landers have been sent and the frequency of such missions may increase. Under such repeated lunar base activities in future, the loss timescales will increase and the lunar exosphere may no longer remain pristine (*Vondrak*, 1988). It is, therefore, necessary to have a record of the neutral composition of the exosphere of the Moon in its present state. The need for reliable composition measurements of the pristine lunar exosphere has been stressed in the vision documents of space agencies (*Paulikas et al.*, 2007).

In this context, NASA's Apollo series of missions (1969-1972) were the pioneers in the field of observations on the surface density and composition of the low latitude lunar exosphere. Lunar exosphere was explored in terms of its total pressure (*Johnson et al.*, 1972), measured with Cold Cathode Gauge Experiments in Apollo-12, 14 and 15 as well as its night-side composition (*Hoffman et al.*, 1973), measured with the LACE

mass spectrometer in Apollo-17. The Chang'E-1 (*Wang et al.*, 2011) and Kaguya (*Yokota et al.*, 2009) missions explored the lunar ion exosphere from orbiting platforms, throwing some light on the neutral exosphere. India's maiden mission to Moon, Chandrayaan-1, carried aboard the Moon Impact Probe (MIP), a microsatellite, which was released from the spacecraft at 13.6°S, 14°E lunar coordinates at an altitude of 98 km, and made to impact close to the lunar South pole (*Kumar et al.*, 2009). MIP carried the CHandra's Altitudinal Composition Explorer (CHACE) mass spectrometer which conducted in-situ observations of the sunlit lunar exosphere at different latitudes and altitudes during the descent of the MIP. In addition, the Chandrayaan-1 studied the energetic neutrals from the Moon with the CENA instrument, which was a part of the orbiter-borne SARA instrument (*Bhardwaj et al.*, 2005; *Barabash et al.*, 2009). More recently, several lunar exospheric species have been studied at the day-night terminators using UV remote sensing with the Lyman Alpha Mapping Project (LAMP) instrument aboard the LRO spacecraft (*Cook et al.*, 2013), and also with the ejecta from the impact of the LCROSS impactor at the lunar South pole at UV wavelengths to explore the surface-bound constituents. The Neutral Mass Spectrometer (NMS) aboard the LADEE mission of NASA has concentrated on the diurnal variation of He, Ne and Ar in the lunar exosphere in the lower latitudes ($\pm 23°$) (*Benna et al.*, 2015). Very recently, the influence of the Solar Wind on the lunar He exosphere was studied through coordinated observations by LRO, LADEE and ARTEMIS (*Hurley et al.*, 2016).

Our present understanding on the complex nature of the lunar exosphere is based on the above observations, while model calculations are resorted to in order to answer the questions in the gap areas. The state-of-the-art in the field of lunar exospheric modelling is the Lunar Exospheric Simulation (LExS) toolkit (*Hodges and Mahaffy*, 2016), which has evolved over several decades from the initial Monte Carlo model by *Hodges et al.* (1972). This model requires realistic boundary conditions based on observations for more accurate modelling of the lunar exosphere.

Review of all the major observations on the noble gases in the lunar exosphere from the above-mentioned missions highlights the fact that the lunar daytime exosphere remained uncharacterized in terms of latitudinal and altitudinal variations. The solar forcing is latitude-dependent because of the variation of the surface obliquity. For example, the latitudinal variation of insolation level on the Moon results in latitudinal variation of the lunar surface temperature, which, in turn, affects the velocity distribution of thermally desorbed species in the lunar exosphere. The other solar forcings like solar wind implantation, sputtering and photon-stimulated desorption also vary with the latitudes. Hence, it is of utmost importance to investigate the latitudinal variation of the sunlit lunar exosphere. This was accomplished with the CHACE experiment aboard the MIP of Chandrayaan-1. The CHACE observations were carried out during lunar day, covering a mass range of 1 to 100 amu. Till date, the observations from CHACE are considered as the only information on the latitudinal and altitudinal distribution of the daytime lunar exosphere. The results of

the investigation carried out on the sunlit lunar exosphere presented in this work are based on the observations by CHACE.

This doctoral work addresses the latitudinal and altitudinal distribution of the major lunar exospheric noble gases (^{40}Ar, ^{20}Ne and ^{4}He) using CHACE/MIP/Chandrayaan-1 data. The study of the lunar noble gases is of paramount importance, as they the are potential tracers of the internal and surface processes. For example, on one hand, lunar Ne and a major portion of He are of solar wind origin (*Heiken et al.*, 1991; *Benna et al.*, 2015), implanted on the lunar surface, while $\sim$10-40% of the He is known to be endogenic (*Hodges*, 1975; *Hurley et al.*, 2016). On the other hand, Lunar Ar, which is dominantly ^{40}Ar, is a radiogenic daughter of the radioactive ^{40}K available in the interior of the Moon (*Heiken et al.*, 1991). He, the lightest among them, is lost mostly by thermal escape (*Stern*, 1999), whereas the major loss mechanisms of Ne and Ar include photoionization, electron impact ionization, charge exchange and ion-pick up by the solar wind (*Johnson et al.*, 1972). ^{40}Ar is also prone to be lost through cold trap condensation in the day-night terminators and the permanently shadowed regions on the lunar surface (*Heiken et al.*, 1991). The above-mentioned noble gases even exhibit different behaviours with respect to the diurnal variation of their surface density. While the surface density of Ar minimises at night due to condensation loss, He and Ne display maximum surface density post-midnight and pre-dawn respectively, due to their non-condensable nature under lunar temperature and pressure conditions.

In addition to these noble gases, the distribution of another non-condensable gas in the lunar exosphere, H_2, is also addressed. Lunar H_2 is a result of the conversion of the solar wind Hydrogen implanted in the regolith (*Hodges et al.*, 1972). The lunar regolith is a reservoir of atomic Hydrogen, which, by chemical sputtering, forms H_2. The H_2 molecule is sensitive to dissociation to H and also thermal escape. Hence, the study of the lunar H_2 provides clues on the lunar surface processes.

The thesis is organised into seven chapters. The first chapter briefly introduces the present knowledge about the lunar origin and evolution. The contributions of different lunar missions towards the current understanding of the lunar exosphere are presented. The second chapter describes the Moon Impact Probe (MIP) mission and the CHACE instrument. It presents the aspects of instrument calibration, characterization and parameterization, and data analysis. The third, fouth, fifth and sixth chapters present the scientific results on the distributions of ^{40}Ar, ^{20}Ne, ^{4}He and H_2, respectively. Finally, the seventh chapter summarises the scientific outcomes of the present work and discusses the questions that are still unresolved. These scientific results prompt the need of detailed exploration of the lunar exosphere using a sensitive mass spectrometer from a polar orbiting satellite.

Chapter 1

Introduction

O Moon! We should be able to know You through our intellect; You enlighten us through the right path.

—Rig Veda

1.1 Moon: Origin and evolution

Moon has been one of the oldest companions of the humankind through its journey of origin and evolution. It has been a time-keeper when there was neither clock nor calender, and thus had immense influence on almanac and agriculture; and the lunar calender is still in use. Tidally locked with Earth, it rotates in synchronism with Earth so that only a single side of the Moon is visible from the Earth (*Heiken et al.*, 1991). Moon has inspired our literature, influenced our mood and psyche, and hence has been an inseparable entity of the mankind through ages. In Indian mythology, Moon is considered a deity and the ancient Indian text, the *Rigveda*, prays to the Moon deity to unveil his mystery to the mankind through intellect and wisdom.

Human knowledge has evolved through a long journey from the realm of mythology to logical science. From the concept of a flat Earth, the concept of the spherical Earth has evolved. From the Earth-centric solar system, humankind has adopted the concept of the Sun-centric solar system. The invention of telescope had pushed the horizon of observations dramatically; the birth of astronomy helped mankind to view things in a larger perspective. Quite naturally, early astronomers found the Moon to be their first focus. The early studies of natural sciences bifurcated to more specialized fields of astrophysics and astrochemistry, which served as potential tools to extrapolate back to the origin of the

Table 1.1: *Orbital and physical parameters of Moon. From de Pater and Lissauer (2010); Greeley (2013)*

Attribute	*Value*
Perigee	356400 to 370400 km
Apogee	404000 to 406700 km
Eccentricity	0.0549
Orbital period	27.321 d (d=Earth day)
Sidereal rotation period[1]	27.321 d (synchronous)
Synodic period[2]	29.530 d
Inclination	5.145 ° to the ecliptic
Mean radius	1737.1 km ($\sim$ 27 % of Earth's mean radius)
Equatorial radius	1738.1 km
Polar radius	1736.0 km
Mass	7.342×10^{22} kg ($\sim$ 1.23 % of Earth's mass)
Moment of interia ratio[3]	0.393
Mean density	3.344 g cm^{-3} ($\sim$ 60 % of Earth's mean density)
Surface gravity	1.622 m s^{-2} ($\sim$ 16.55 % of Earth's surface gravity)
Surface escape velocity	2.38 km s^{-1} ($\sim$ 21.2 % of the Earth's surface escape velocity)
Bond albedo [4]	0.123

[1] Sidereal rotation period is the time Moon takes to orbit 360° around the Earth relative to the fixed stars.

[2] Synodic period is the periodicity of the lunar phases, i.e. the time between two consecutive full-Moons. As the Earth moves in its own orbit, the synodic period of the Moon is greater than its sidereal period because it has to travel further in its orbit around Earth in order to reach the next full-Moon condition.

[3] Moment of interia ratio is a dimensionless quantity. For a spherical body of moment of inertia I, mass M and radius R, the moment of interia ratio is defined as I/MR^2. Refer subsection 1.1.1 for more details.

[4] Bond albedo is the ratio of the total (integrated over frequency) radiation reflected or scattered by an object to the total (integrated over frequency) incident radiation.

solar system and eventually the Universe. Several hypotheses were formulated and many of them did not stand the test of time; while some of them stood firmly and formed the pillars of our current understanding of the Universe. One such hypothesis is the *nebular hypothesis* (*Woolfson*, 1993; *Montmerle et al.*, 2006) on the origin of the solar system.

Table 1.1 summarises the physical parameters of the Moon.

1.1.1 Lunar origin: a brief history

According to the nebular hypothesis, the solar system was formed out of a rotating giant molecular cloud and dust, called the solar nebula. The gravitational contraction of the solar

nebula gave rise to the proto-Sun at the centre, surrounded by swirling ice, dust and rocks. The swirling ice, dust and rocks were gravitationally bound to the proto-Sun forming a proto-planetary disc. Terrestrial planet accretion in our solar system is understood to have happened in three stages (*Canup*, 2004). First, the random collisions between the fragments in the proto-planetary disc led to the formation of kilometer-sized planetesimals. In the second step, the planetesimals coalesced to form planetary embryos, which were about 1 to 10 % of the Earth's mass. In the third step, tens to hundreds of the planetary embryos coalesced to form the proto-planets. The energy deposited by accretion resulted into melting of the proto-planets. The heavier species in the melt sank more towards the centre of the planet while the lighter ones were buoyant and floated up. This process is referred to as 'planetary differentiation'. Thus, the crust of the terrestrial planets are composed of lesser dense materials than their mantles and core. The gas giants were formed by the formation of planetary embryos bigger than a critical mass (*Mizuno*, 1980), which accreted large amount of gas from the protostellar disk (*Stevenson*, 1982; *Pollack et al.*, 1996; *Inaba et al.*, 2003). Regarding the formation of the ice giants Uranus and Neptune, it is currently believed that a chain of events, viz. disk instability leading to the formation of gas giant protoplanets, coagulation and settling of dust grains to form icerock cores at their centers, and photoevaporation of their gaseous envelopes, is responsible for their formation (*Boss et al.*, 2002).

Thus, each proto-planet in the inner solar system (from Mercury at 0.38 AU to Mars at 1.52 AU) underwent a long process of evolution through cooling of the molten magma and bombardment by the meteoroids. They are believed to have lost their primary atmospheres paving the way for the secondary atmospheres. The Moon was formed by the last giant impact experienced by Earth. *Jacobson et al.* (2014) dated this impact based on the concentration of Highly Siderophile Elements (HSE) in Earth's mantle relative to the HSE abundances in chondritic meteorites and concluded that the Moon was formed after 95 $\pm$ 32 My of the formation of the solar system.

Earth's Moon has some interesting features, which make it unique. Unlike the other natural satellites in the solar system, the ratio of the radius of the Moon to its host planet, the Earth, is significantly large ($\sim$ 0.27) and the composition of the lunar crust resembles the composition of the Earth's mantle (*Geiss and Rossi*, 2013). The moment of interia ratio is an important index that tells about the radial distribution of mass in a celestial body. For a spherical body of moment of inertia I, mass M and radius R, the moment of interia ratio is defined as I/MR^2. The ratio is 0.667 for a hollow sphere, 0.4 for a homogeneous sphere and less than 0.4 for a centrally massive sphere. How much less is this ratio from 0.4 is a measure of the concentration of mass in the core of the celestial body. The moment of inertia ratio of the Moon is $\sim$ 0.393, only slightly less than that of an ideal homogeneous sphere (*Yoder*, 1995). The moment of inertia ratio for Earth is 0.33 (*Yoder*, 1995), which suggests that Earth has a relatively bigger core than Moon. For

Moon, the radial distribution of mass is relatively uniform as compared with the Earth, which indicates a relatively smaller higher density central core. The moment of interta ratio of the Moon, along with the lunar seismic data suggests that the average density of the Moon is 3.344 $\pm$ 0.003 g cm^{-3}, with a lower density crust (density 2.85 g cm^{-3}) of about few tens of kilometers thickness and an iron core (density 8 g cm^{-3}) with a radius less than 300-400 km (*de Pater and Lissauer*, 2010). Thus, any successful theory on the lunar origin must have to satisfy the constraints posed by celestial dynamics, geophysics and geochemistry. The hypotheses on the birth of the Moon have undergone evolution over time, from the pre-Apollo era till date, and have later been constrained by observations.

Pre-Apollo hypotheses on the lunar origin

The three hypotheses on the lunar origin that predominated prior to the Apollo era were capture, fission and co-accretion (*Wood*, 1986; *Boss*, 1986; *Canup*, 2004). None of these models were able to account for all the major characteristics of the Moon as well as the Earth-Moon system. The capture hypothesis (*Singer*, 1986; *Urey*, 1966) suggested that the Moon was formed independently and later gravitationally captured during the very early history of the Earth. This could explain differences in chemical compositions between Moon and Earth. However, the capture hypothesis could not explain Moon's capture in its present orbit. The fission hypothesis (*Darwin*, 1879) suggested that the rapidly spinning Earth became rotationally unstable while it was still molten and thus a chunk of material flung out of the equatorial region, thereby forming the Moon. The fission hypothesis requires very high value of the angular momentum of the Earth-Moon system. The angular momentum of the Earth-Moon system ($L_{E-M} = 3.5 \times 10^{41}$ g cm^2 s^{-1}) is known to be fairly conserved for the last 4.5 Gy (also called Ga or Giga annum, meaning Billion years) (*Canup and Asphaug*, 2001) and therefore the above hypothesis was not plausible. The co-accretion hypothesis (*Schmidt et al.*, 1959) suggested that the Moon grew simultaneously with the Earth by accretion of smaller material from the solar nebula. The coformation theory, however, did not explain: i) the iron depletion in Moon and ii) the Earth-Moon angular momentum. It should be noted that growth by multiple small impacts typically would result into smaller angular momentum and slow planetary rotation, unlike what is encountered with the Earth-Moon system.

Later, the observations from the Apollo series of missions by NASA, especially the careful analyses of the returned lunar samples provided the first set of observational constraints, guiding the hypotheses on the lunar origin and evolution.

Post-Apollo hypothesis: Giant impact

Initially, solar system is believed to have experienced chaotic dynamics of colliding debris and the materials left-over during the formation of the solar system. Based on geophysical and geochemical evidences, it is believed that about 4.5 Gy (Billion years) ago, while the Earth was still differentiating, it was impacted by a Mars-sized rock (*Melosh and Sonett*, 1986; *Canup and Asphaug*, 2001), often referred to as *Theia* (*Geiss and Rossi*, 2013), and a part of the proto-Earth was ripped off. Computer simulations (*Melosh and Kipp*, 1986; *Kipp and Melosh*, 1986*a*,*b*) suggest that both the impactor and the Earth had metallic cores, surrounded by silicate mantles at the time of the giant impact. As a result, the metallic cores of both the bodies coalesced in the Earth while the ejected silicate material were gravitationally bound to the Earth. Accretion of these impact-generated fragments formed the proto-Moon, rotating round the Earth. This is known as the giant impact hypothesis on the origin of the Moon. Although the mantles of the Moon and Earth have similar compositions (*Geiss and Rossi*, 2013), lunar samples are found to be more depleted in volatiles than the terrestrial rocks, which is explained by the preferential accretion of the volatile-rich melt by the proto-Earth rather than the growing Moon (*Canup et al.*, 2015). In the sense of randomness of chances, the giant impact was a very fortuitous event that made Earth's Moon a reality.

In the post Apollo era, with the lunar samples available for radioactive dating, it was anticipated that all the questions about the origin of the Moon would be permanently answered. This would have been the case had Moon been a perfectly homogeneous body with no separation of minerals by the planetary differentiation process. As we will see in the next section, Moon has undergone the differentiation process which has obscured many clues of its origin. The striking similarity between the Earth and the Moon in terms of their Oxygen isotope composition is one of the important constraints of a Giant impact hypothesis (*Canup*, 2012; *Geiss and Rossi*, 2013), which suggests an impactor of comparable size with that of the proto-Earth (at the time of the impact) with impactor to total mass ratio of ~ 0.45.

Recent studies (*Wang and Jacobsen*, 2016) based on high precision potassium isotope (^{41}K and ^{39}K) data indicate that the lunar rocks are enriched in ^{41}K, by ~ 0.4 parts per thousand, which is attributed to isotopic fractionation owing to incomplete condensation of the potassium vapour during the lunar formation. From the extent of the isotopic fractionation, *Wang and Jacobsen* (2016) predicted that the Moon condensed at a pressure of more than 10 bar. This study is suggestive of an extremely violent giant impact, which led to the vapourization of the impactor as well as a substantial part of the Earth's mantle. The resultant vapours underwent thorough mixing and its subsequent condensation caused the formation of the Moon. This explains the idential isotopic composition of the Earth and the Moon.

In the view of the high energy involved in the giant impact, the giant impact hypothesis requires a higher (by a factor of ~ 2) post-impact angular momentum of the Earth-Moon system as compared to the present value. The subsequent shedding of this additional angular momentum of the Earth-Moon system is attributed to the process of evection resonance with the Sun (*Canup*, 2012, 2014). Evection resonance occured when the precession period of the periapsis of the Moon matched with the orbital period of the Earth (*Ćuk and Stewart*, 2012; *Noordeh et al.*, 2014). As the early Moon's orbit expanded due to tidal interactions with the Earth, evection resonance took place. As a result, the orbital eccentricity of the Moon increased and the angular momentum of the Earth-Moon system decreased reaching up to the present value of the angular momentum that has been conserved for last 4.5 Gy (*Canup and Asphaug*, 2001).

Thanks to the remote sensing and in-situ measurements of the lunar surface; it has now become possible to characterize the Moon globally and arrive at realistic constraints for the models. The giant impact hypothesis suggests that the Moon was completely or at least partially molten in its early formation stage, which was known as the Lunar Magma Ocean.

1.1.2 The Lunar Magma Ocean (LMO)

During the process of solidification of the molten magma, the low density aluminium-rich plagioclase rock anorthosite buoyantly floated while the heavier material sunk beneath. Due to this process of differentiation, the upper crust of the Moon is rich in lighter minerals, like plagioclase feldspar ($CaAl_2Si_2O_8$), while the deeper part of the crust and the mantle are rich in heavier minerals, like (Mg, Fe)SiO_3 (pyroxene) and (Mg, Fe)$_2SiO_4$ (olivine). The LMO hypothesis suggests that the process of differentiation started through solidification of magma and first produced mantle, rich in olivine and pyroxenes. Plagioclase began to crystallize late when more than 75 % of the LMO was solid (*Warren*, 1985). The thickness of the lunar crust is beleived to be directly proportional to the extent of melting (*Warren*, 1985). It was suggested by *Elkins-Tanton et al.* (2011) that a magma ocean of $\sim$ 1000 km depth is consistent with the creation of an anorthositic crust of 40-50 km thickness. Recently, the GRAIL spacecraft, using the gravity data, suggested that the lunar crustal thickness is $\sim$ 34 to 43 km (*Wieczorek et al.*, 2013). The GRAIL data also suggested that the thickness of the LMO was $\sim$ 200 to 300 km (*Andrews-Hanna et al.*, 2013). *Elkins-Tanton et al.* (2011) further suggested that in the first $\sim$ 1000 years, about 80$\%$ (by volume) of the magma ocean was solidified, with the process of complete solidification of the magma having been gradual that took another few tens of millions of years.

The gradual solidification of the molten magma ocean gave rise to a gravitationally unstable stratigraphy with higher density at the top, supported by lower density regions at the bottom of mantle. This induced Rayleigh-Taylor instability, which lead to an

'overturn'of the mantle stratigraphy. The time of this stratigraphy-overturn is inversely proportional to the thickness of the solidified layer. As a result of the mantle overturn, much of the iron- and titanium-bearing material sank to greater depth with a possible exception of some titanium-bearing materials, which did not participate in the process of overturn, remained under the solidified lower crust, thus increasing the titanium heterogeneity in the lunar upper mantle (*Elkins-Tanton et al.* (2011), and the references therein).

During the gradual solidification of the molten magma, different minerals are believed to have cystallized in a sequence, within the magma, determined by the chamical composition and pressure (*Taylor*, 2011). Last in the sequence of crystallization could be the crystallographically incompatible elements that were not incorporated into most of the minerals that crystallized (*Geiss and Rossi* (2013), and references therein). They were Potassium (K), Rare Earth Elements (REE) and Phosphorus (P), collectively known as KREEP, which became progressively abundant in the magma as the crystallization process continued.

1.1.3 Formation of basins and Lunar maria

Although the Moon was cooling first radiatively and later conductively through the conductive plagioclase lid at the upper crust, it was still hot due to the radioactive decay of isotopes such as ^{232}Th and ^{238}U and the process of accretion and differentiation. That is believed to be the period when impacts on the planets by the solar system debris were common. Such impacts created the big basins (such as Imbrium, Crisium, Serenitatis, etc.) with upturned rims on the Moon. The lunar samples returned by Apollo provided the timing of the basin formation, which dates back to the Late Heavy Bombardment (LHB), about 3.8 to 4 Gy ago, which is considered the window in the lunar chronology that experienced brief pulse of impacts by large objects. Many of the impacts created fissures (cracks) on the lunar surface, through which hot mantle material rose to the surface. The impact basins were filled with the molten lava. It crystallized to form the basalt rock. The composition of the basalt rock varied since they were a result of the magma from different depths of the lunar interior. Basalts are dark, fine-grained volcanic rocks, and they formed the large, smooth and dark regions visible on the lunar surface, known as lunar maria (see Figure 1.1). In Latin, 'maria' means 'sea'; and the early astronomers found a resemblance between the smooth basaltic regions and the Earth's sea surface. These regions are smooth as they are relatively young and hence less cratered than the lunar highlands. Radiometric dating suggested that the mare basalts are 3.0 to 3.9 Gy old (*Geiss and Rossi*, 2013).

1.1.4 The 'recent' Moon

As the interior of the Moon cooled down, volcanism decreased. Although it is believed that Moon is geologically inactive since last $\sim$ 1 Gy, there have been evidences of recent lunar volcanism from remote sensing measurements, which date to about 100 Ma (*Braden et al.*, 2014), and sporadic occurrences of Transient Lunar Phenomena (*Crotts*, 2008). The striking of the lunar surface by meteoroids still continue which break the rocks to form dust (regolith) that cover the lunar surface.

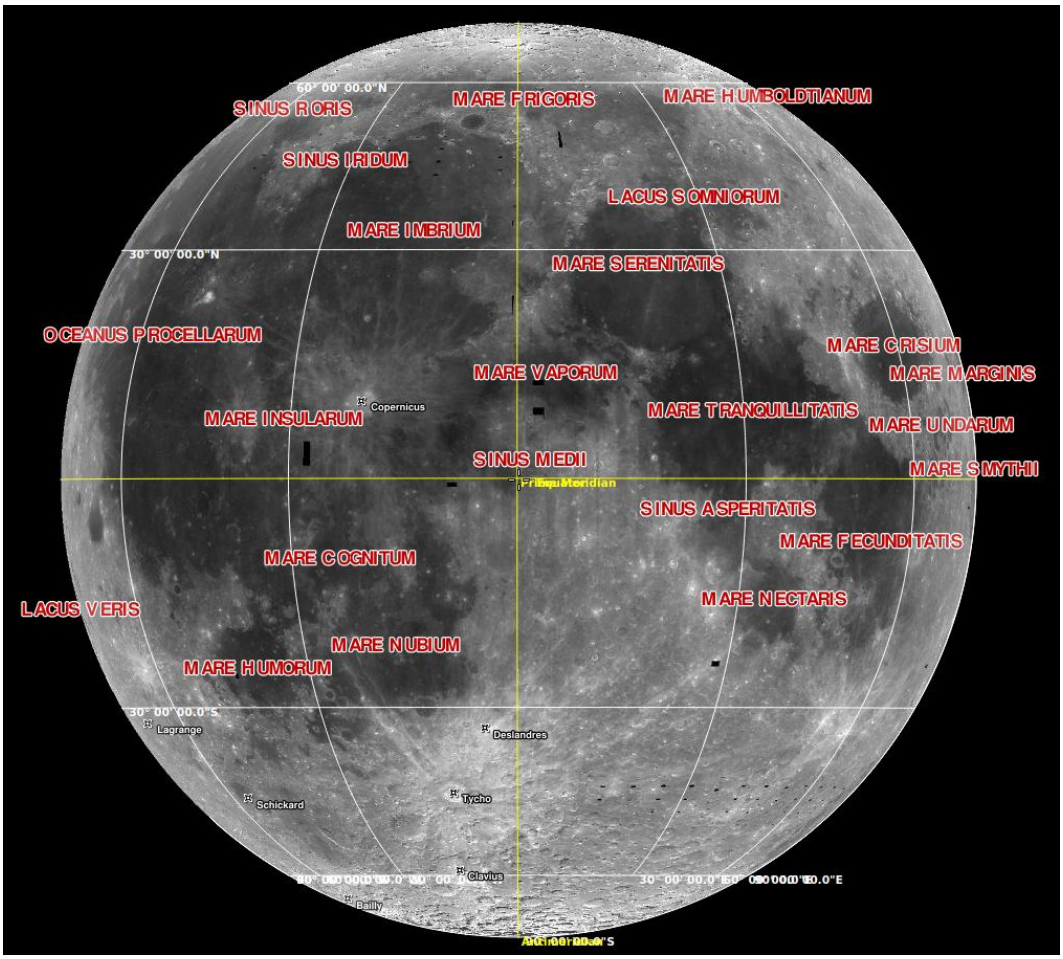

Figure 1.1: Moon, as seen from the Earth. The yellow coloured vertical and horizontal lines represent the lunar prime meridian and equator respectively. The dark regions are Mare Basalts, formed by the solidification of the molten magma that oozed from the interior through fissures. They are relatively younger (3.0 to 3.9 Ga) than the highlands (relatively brighter regions). [Taken from Marble virtual globe (http://edu.kde.org/marble)].

To summarize, lunar history is divided into five periods, viz.: 1) the pre-Nectarian period, 2) Nectarian period, 3) Imbrian period, 4) Eratosthenian period, and 5) Copernican period (*Harland*, 1990; *Hiesinger et al.*, 2003; *Greeley*, 2013). The pre-Nectarian period is represented by the ancient heavily cratered highlands. No geologic formations have been mapped for this era (*Greeley*, 2013). The Nectarian period marks its beginning with the

formation of the Nectaris impact basin. The Imbrian period began with the formation of the Imbrium basin. The Imbrian period witnessed extensive eruptions of mare basalts and subsequent flooding of the floors of the impact basins. The Eratosthanian and Copernican periods are based on mapping and relative age determinations of crater deposits from the impact craters Eratosthenes and Copernicus. The Eratosthenian era craters are fresh with sharp crater rims and identifiable secondary craters. Copernican era craters are sufficiently young and are not optically mature. Figure 1.2 shows a schematic of the evolution of the Moon.

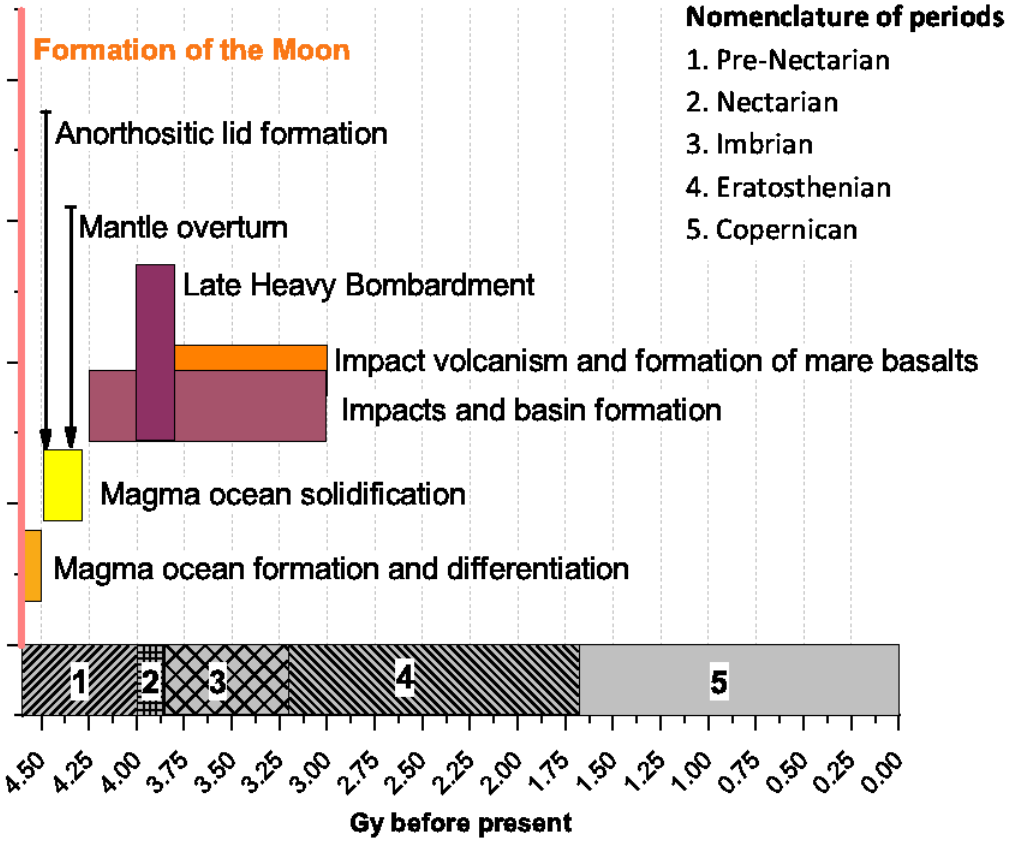

Figure 1.2: A schematic of the time evolution of the Moon. The time scales are from *Elkins-Tanton et al.* (2011); *Stern* (1999); *Greeley* (2013)

As the Moon underwent significant geological evolution since its birth, there has also been a substantial evolution of the lunar atmosphere. The present state of the lunar atmosphere is a result of an evolution since 4.5 Gy, closely connected with its geological and thermal evolution, and influenced by impacts with solar system debris.

1.2 Evolution of the lunar atmosphere

The young Moon is believed to have had a very thick atmosphere, owing to the vapour pressure of the molten magma ocean material. As the magma ocean gradually cooled and

solidified, the pressure decreased. Over this background pressure, there were episodic increases of pressure due to meteoritic bombardment. This is discussed in detail by *Stern* (1999), who has divided the pathway of the evolution of the lunar atmosphere in three epochs and presented a schematic illustration of this evolution, as presented in Fig 1.3.

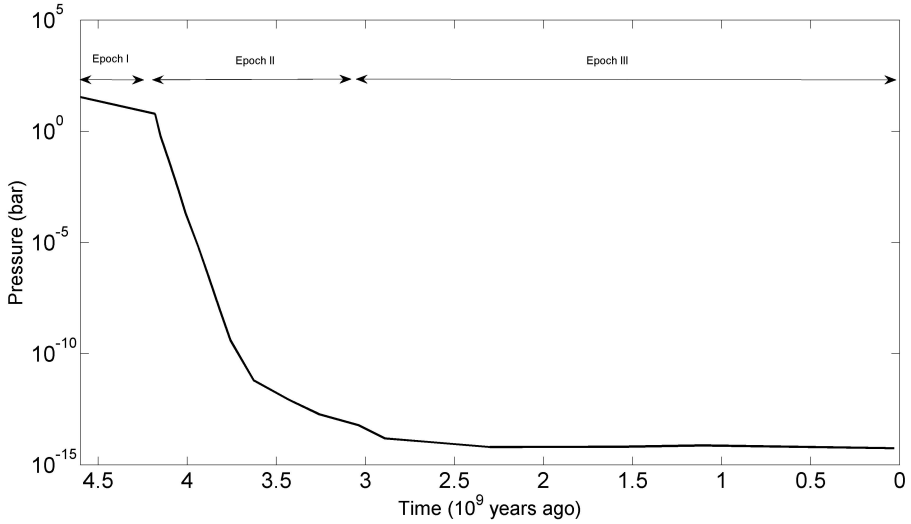

Figure 1.3: A schematic of the evolution of the lunar atmosphere since its formation (redrawn from Stern, 1999). Epoch II and III witnessed episodic increase of the atmospheric pressure due to the release of gases as a result of bombardment of meteorites.

1.2.1 Epoch I: From $\sim$ 4.57 Gy to $\sim$ 4.4 Gy

Prior to the formation of the lunar crust ($\sim$ 4.4 Gy ago), the lunar atmosphere was thick, governed by the vapour pressure of the rocks in the molten magma ocean, at temperatures 1000 to 2000 K. The rock vapours primarily consisted of Silicon, Aluminium, Magnesium, Sulphur, Iron Oxides as well as volatiles like Hydrogen Sulphide. This resulted into a rock vapour pressure-limited atmospheric pressure of $\sim 10^2$ bar, much like the present atmospheric pressure of Venus. The escape of this atmosphere must have been dominated by the Jeans process (escape of atoms from the lunar gravity by acquiring enough thermal energy) (*Vondrak*, 1974; *Stern*, 1999) and scavenging by the solar wind and the solar UV photons (*Stern*, 1999).

1.2.2 Epoch II: From $\sim$ 4.4 Gy to $\sim$ 3.1 Gy

This era represents the window when the lunar crust is solidified ($\sim$ 4.4 Gy ago) and volcanism associated with occasional large crater- or basin-forming impacts predominated ($\sim$ 3.8-3.4 Gy) (*Stern* (1999) and the references therein). These impacts either punctured the crust releasing the internal gases and/or caused ablation of the materials at the point

of impact releasing gases to the lunar atmosphere. The mare volcanism and hence the formation of mare basalts continued till $\sim$ 3.1 Gy. In this epoch, the initial rock vapour pressure-limited atmosphere went on declining by thermal or Jean's loss and other non-thermal loss mechanisms, as described in details in section 1.3.2. During that era the lunar atmosphere was supported by internal releases aided by volcanism and impacts.

1.2.3 Epoch III: Last $\sim$ 3.1 Gy

About $\sim$ 3.1 Gy ago, the mare volcanism ceased (*Stern*, 1999). By that time, the larger impacts also became less frequent. The mean time before successive impacts for 10 m-class of impactors, which are capable of generating a substantial transient atmosphere, became 100-200 years. Model calculations suggest that these impacts generate vapours of 1-5 times of the impactor mass, with characteristic vapour temperature of 2000-5000 K. This is less than the temperature ($\sim$ 16,000 K) required by the vapours to escape the lunar gravity. Also, the ionization effects are not very effective at vapour temperatures below $\sim$ 20,000 K. As a result, all the impact generated vapours essentially remain as neutral gases in the lunar atmosphere. As *Vondrak* (1974, 1988) calculated, transient lunar atmospheres with masses $\sim 10^{10}$ g decline in a few days back to normalcy. Considering the mean time before such transient atmosphere-forming impacts and their characteristic loss time, the duty ratio for significant lunar atmospheric transient above the current background environment is only $\sim$ 0.1-3$\%$. Hence, the time-averaged value of the present lunar atmospheric pressure suggests that it is extremely tenuous and falls under the category of exosphere.

The term exosphere is the outermost part of any planetary atmosphere where the atoms rarely collide with each other. Exosphere is defined as the region where the mean free path of the gas atoms or molecules is larger than the local scale height (*Chamberlain*, 1963). The term exobase refers to the bottom of the exosphere where the mean free path of the gas atoms and molecules just exceeds the local scale height. In the absence of collisions, the trajectories of the exospheric neutral particles are governed by the gravitation of the planet and solar radiation pressure (*Bishop and Chamberlain*, 1989; *Beth et al.*, 2016*a*,*b*). In the collisionless regime, the dynamics of a species is driven solely by its kinetics, which dictates whether a species will be ballistic, satellite, or escaping (*Chamberlain*, 1963). Ballistic particles are the ones which are gravitationally bound to the host planet, with their orbits intersecting the exobase. The satellite particles are also gravitationally bound to the host planet, but they have stable orbits above the exobase. The escaping particles, as the name suggests, are the ones that escape the gravitational pull of the planet.

The exobase of Earth is located at an altitude of $\sim$ 550 km (*Angerami and Thomas*, 1964), while that on Mars is at $\sim$ 200 km (*Yagi et al.*, 2012). There are celestial bodies whose exospheres are bounded on one side by their surfaces; typical examples of such Surface Boundary Exospheres (SBE) in the solar system include Earth's Moon, Mercury,

Saturn's satellite Enceladus, asteroids etc.. Earth's Moon is the closest SBE to the Earth and hence a natural laboratory to study the physical processes characteristic to the SBEs in the solar system.

1.3 The Lunar Exosphere

Initially, polarimetric studies indicated an upper limit of 10^{-9} to 10^{-10} bar for the lunar surface pressure (*Dollfus*, 1956). It was generally believed that any lunar atmosphere would have been lost to space due to non-thermal processes, like the ion pick-up by the solar wind (*Herring and Licht*, 1959; *Hinton and Taeusch*, 1964). The Apollo series of measurements returned the first set of data on the lunar atmospheric composition near the surface. Yet, these experiments did not yield useful data from the sunlit side due to the saturation of the cold cathode gauges and mass spectrometers presumably due to the contamination and degassing from the space modules (*Hoffman et al.*, 1972; *Stern*, 1999). After the Apollo missions, the limited set of in-situ observation data available on the lunar exosphere are from the Chandra's Altitudinal Composition Explorer (CHACE) instrument aboard the Moon Impact Probe (MIP) in the Chandrayaan-1 mission in 2008 (*Kumar et al.*, 2009) and the Neutral Mass Spectrometer (NMS) instrument aboard the Lunar Atmospheric and Dust Environment Explorer (LADEE) mission in 2013-2014 time frame (*Benna et al.*, 2015).

The lunar neutral exosphere is a result of a dynamic equilibrium between several source and sink processes. The species that constitute the lunar neutral exosphere, if classified on the basis of their energetics, form two classes, viz. thermal and non-thermal. The thermal species are the ones, whose energy (and hence velocity) distribution follows the Maxwell-Boltzmann distribution. The Maxwell-Boltzmann velocity distribution of gases is given by:

$$f(v)dv = N \left(\frac{2}{\pi}\right)^{1/2} \left(\frac{m}{kT}\right)^{3/2} v^2 \, exp\left(\frac{-mv^2}{2kT}\right) dv \tag{1.1}$$

Here, v is the velocity of the species, m is its mass, N is its local number density and T is the kinetic temperature.

The Maxwell-Boltzmann distribution suggests that the most probable velocity of a particle at a temperature T is given by

$$\bar{v}_0 = \sqrt{2kT/m} \tag{1.2}$$

The non-thermal species, on the other hand, are characterized by higher kinetic temperatures and do not follow the Maxwell-Boltzmann distribution. The energy distribution

of the species in any planetary atmosphere is, therefore, a signature of the process it has undergone. As for example, the energy distribution of the species originated by the process of charged particle sputtering is different from that of the thermalized species; the former follow the Sigmund distribution (refer subsection 1.3.1), while the latter follow the Maxwell-Boltzmann distribution.

The scematic in Figure 1.4 summarises the source and sink processes of the lunar exosphere.

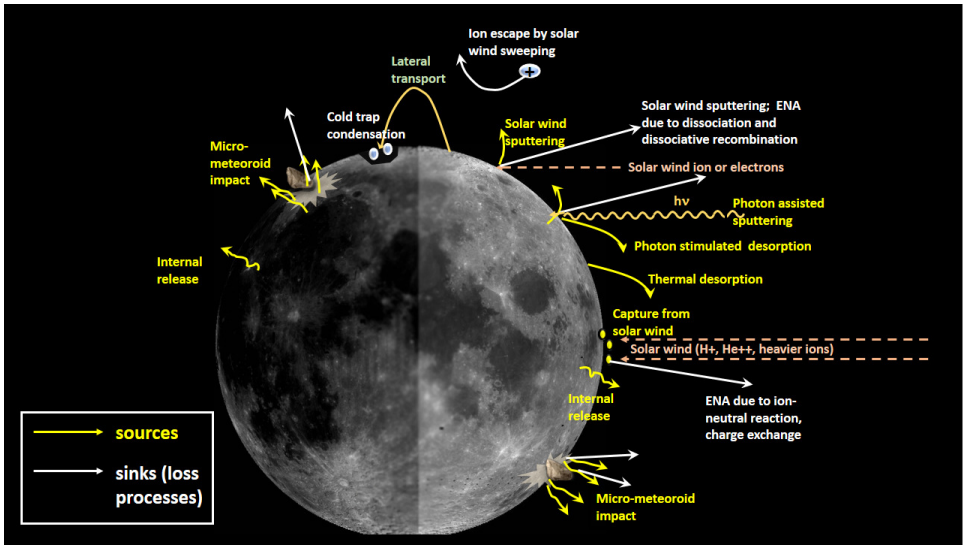

Figure 1.4: Schematic showing the source and sink processes in the Lunar exosphere

1.3.1 Source processes

In the lunar exosphere, different source mechanisms are important for different species. Also, in general, there may be multiple sources and sinks of a given species (*Stern*, 1999). The sources of the lunar exosphere include Solar wind capture and subsequent desorption, Internal release, Impact vapourization and sputtering. Their relative importance is dependent on the species. As for example, for lunar Helium is mostly of solar wind origin, while there is an internal release source which accounts for the rest. For ^{40}Ar, on the other hand, it is the internal release process that is the only substantial source, since solar wind contains mostly ^{36}Ar rather than ^{40}Ar (*Wieler*, 2002). When it comes to ^{20}Ne, it is completely from the solar wind. H_2 is mostly due to the chemical sputtering of solar H atoms on the lunar surface. The sources of the lunar exosphere are briefly discussed below.

- **Thermal desorption**

  Thermal desorption refers to the process of sublimation of the atoms from the adsorption wells on grains at the uppermost layer of the surface or within the uppermost

regolith, i.e. to the depth that is in thermal contact with the diurnal cycle. The adsorbed atoms acquire thermal energy from solar radiation, which, in turn, is converted to their vibrational energy (phonons) under van der Waals potential at the adsorption site. The thermal desorption rate is the inverse of the residence time of the adsorbed atom in the potential well, which is given by (*Hunten et al.*, 1988)

$$\tau \;=\; \tau_0 \, exp\left(\frac{D_0}{kT}\right) \tag{1.3}$$

Here τ_0 is the vibration period of the adsorbed atom for the van der Waals potential, D_0 is the heat of adsorption, k is the Boltzmann constant, and T is the surface temperature. τ_0 is a property of the adsorbing material and not of the species (*Grava et al.*, 2015*b*). Thus, although initiated by photons (solar radiation), thermal desorption is fundamentally a phonon-induced process.

Armand (1977) has formulated the classical theory of thermal desorption which says that although the velocity distribution of the thermally desorbed particles is Maxwellian at the crystal temperature regardless of the interaction potential (between the surface and the adsorbed atom, often called the adatom), the total desorption rate depends on the vibrational frequency of the adatom and the surface-adatom interaction, which, in turn, depends on the surface binding energy. The Armand distribution of the thermal desorption rate is thus a Maxwellian, modified by a prefactor, accounting for the vibrational frequency of the adatom and the surface-adatom interaction.

- **Photon Stimulated Desorption (PSD)**

  While thermal desorption is a phonon-induced process, PSD is induced by photons. In PSD, the photon energy is absorbed by an atom on the surface and it is excited to a new electronic state, where its binding energy to the surface is reduced (*Townsend*, 1979). If the thermal lattice energy is sufficient to overcome the new binding energy, the atom undergoes PSD (*Townsend*, 1979). PSD is also known as the major source of the lunar Na and K exosphere (*Colaprete et al.*, 2016).

- **Capture of solar wind particles**

  In the absence of a global magnetic field, the charged particles from the solar wind are implanted onto the surface. A substantial fraction of them may be neutralized, and upon acquiring thermal energy from insolation and/or meteoroid impacts, these are released from the surface and become a part of the lunar exosphere. Examples include the lunar Hydrogen, Helium, Neon, Argon-36 (*Stern*, 1999), as well as heavier elements, like Krypton and Xenon, that were implanted on the surface of the Moon (*Wieler*, 2002). In fact, the lunar soil acts as a substrate that collects the solar wind particles, which can be used to study the abundances of different elements in the solar wind (*Wieler*, 2002).

- **Sputtering**

  The term sputtering refers to the process of ejection of a species from a lattice site in the upper few mono-layers of a surface, due to the injection of a discrete impulse of energy. The solar wind is known to sputter material from the regolith and to implant material in and around the regolith. Effective yield obtained from the analysis of lunar samples indicates sputtering erosion of 10-100 g s^{-1} for the whole Moon (*Arnold*, 1979). Sputtering may be stimulated by different sources, like Photon Assisted Sputtering (PAS), charged particle sputtering (due to incident energetic electrons, protons or alpha particles) or chemical sputtering.

  In PAS, a photon bombards a surface atom and imparts energy, but no momentum (*Townsend*, 1979). If the lattice vibration energy (phonon energy) overcomes the binding energy, the atom is liberated from the surface. The liberated atom has the energy in the thermal range (*Townsend*, 1979).

  In charge particle sputtering, the incident ion or electron imparts both energy and momentum to the surface atom. The incident ion undergoes a series of collisions on the surface, and atoms that recoil with sufficient energy undergo secondary collisions, thereby creating secondary recoiling atoms. Some of the atoms are backscattered through the surface. If they have sufficient energy to overcome the surface binding energy, they are liberated as sputtered atoms. The atoms ejected by sputtering have an energy distribution extending from thermal to high energies. The energy distribution for particles sputtered from a solid is given as (*Sigmund*, 1969):

$$f(E_e) = \frac{6E_b}{3 - 8\sqrt{E_b/E_c}} \frac{E_e}{(E_e + E_b)^3} \left(1 - \sqrt{\frac{E_e + E_b}{E_c}}\right) \tag{1.4}$$

  Here, E_e is the energy of the sputtered species, E_b is its surface binding energy and E_c is the cut-off energy, which is the maximum energy that can be imparted to a sputtered particle by a projectile particle. E_c is given by

$$E_c = E_i \frac{4M_1M_2}{(M_1 + M_2)^2} \tag{1.5}$$

  Here, E_i is the energy of the projectile, and $M_{1,2}$ represent the masses of the projectile and the target respectively (in atomic mass unit).

  The cut-off energy depends on the masses of the projectile ion and the target atom as well as on the energy of the projectile. According to the Sigmund distribution given by equation 1.4, the most probable velocity is given by

$$\sqrt{E_b/m_{sputtered}}$$

Here $m_{sputtered}$ is the mass of the sputtered species in kg. As for example, for Oxygen, E_b = 2.0 eV and the most probable velocity is 3.47 km s^{-1}, which exceeds the lunar surface escape velocity of 2.38 km s^{-1}. Sputtered Oxygen atoms in the lunar exosphere have been reported by *Vorburger et al.* (2014) from the CENA/SARA observations of Chandrayaan-1. Figure 1.5 shows a plot of the Sigmund distribution function along with the Maxwell-Boltzmann energy distribution function.

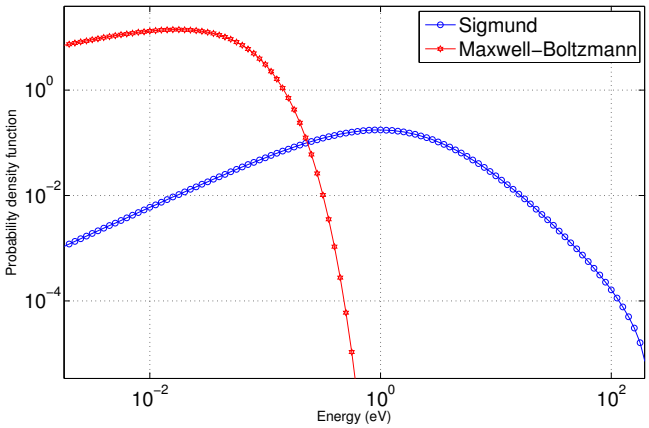

Figure 1.5: The energy distribution of sputtered Oxygen atoms, given by the Sigmund distribution function, (equation 1.4) for proton projectiles with 1 keV energy and surface binding energy of 2 eV, is plotted with open stars. The Sigmund distribution function, at higher energies, falls off with E_e^{-2} variation. The Maxwell-Boltzmann energy distribution function followed by thermal atoms, given by $2(E/\pi)^{1/2}(kT)^{-3/2}e^{-E/kT}$, with T=400 K (typical value of the dayside lunar surface temperature at equator) is co-plotted (open circles) for comparison. The Maxwell-Boltzmann distribution falls off exponentially with energy.

Sputtering by solar wind protons of 1 keV energy causes maximum yield for the O, Si, Ca and Fe atoms in the energy range of 1 to 10 eV (*Wurz et al.*, 2007). Due to their larger scale height, the sputtered species dominate the exosphere at altitudes exceeding a few 1000 km (*Wurz et al.*, 2007).

Solar wind sputtering is believed to be a minor source of the lunar exosphere, which accounts for $\sim 10^{-3}$ % of the lunar day-side total exospheric density (*Wurz et al.*, 2007).

Chemical sputtering, on the other hand, results when a chemical reaction on the surface is exothermic and has sufficient excess energy to desorb an atom or molecular fragment onto a ballistic trajectory.

Recently, the contribution of the self-sputtering process to the lunar exosphere has been reported (*Poppe et al.*, 2013), where the newly born ions from the exosphere cause sputtering of additional neutrals from the lunar surface. The contribution of self-sputtering, however, is an order of magnitude less than the solar wind sputtering.

- **Meteoritic impacts**

  Meteoritic impacts onto the lunar surface at velocities above a few km s^{-1} (average lunar meteorite impact velocity is about 15 km s^{-1} (*Stern*, 1999)) produce both a cloud of impact-generated vapour and a source of hot or even molten surface material that subsequently outgasses until it cools. The yield depends on several factors, like the energetics of collision, composition of the target site and impactor, surface temperature, rock/soil ratio, compaction state, etc. The micrometeroid impacts on the Moon contribute to the Na, K, Li, Si, Ca, Al, Mg and Fe exospheres (*Berezhnoy*, 2013; *Colaprete et al.*, 2016).

- **Internal release**

  Gases, like ^{40}Ar, ^{222}Rn are released from the lunar interior by the process of volcanism, radiogenic activity, crustal diffusion or seismically induced seepage (*Hodges*, 1977; *Stern*, 1999; *Killen*, 2002). Evidences of recent (age few tens of My) tectonically induced shallow moonquakes have been found from Lunar Reconnaissance Orbiter and Chandrayaan-1 images (*Senthil Kumar et al.*, 2016). The impact due to volcanism in the geologically recent years ($\sim$ 100 My) has not been found to be very significant (*Braden et al.*, 2014). Data from the Apollo seismic network stations had reported only very minor (10^7-10^9 erg) tidal, stress-driven events over a period of six years (*Nakamura et al.*, 1979). Correlation between these stress-driven seismic events and Ar releases detected by the Apollo 17 LACE surface mass spectrometer have been reported by *Hodges and Hoffman* (1975) and Rn production has been found to be correlated with the mare-highland boundaries.

- **Release due to dielectric breakdown**

  Jordan et al. (2017) recently suggested that the large solar energetic particle (SEP) events may cause charged particles penetrate the lunar regolith, cause sufficient charging, leading to dielectric breakdown in the upper 1 mm of the lunar regolith in the Permanently Shadowed Regions (PSR). The PSRs are regions in higher lunar latitudes where the maximum solar declination could be as low as 1.54° (*Williams et al.*, 2017) so that solar radiation can never reach there. This phenomenon is believed to cause vapourization and melting in the coldest PSRs with production rates up to 1.8 to 3.5 $\times$ 10^{-7} kg m^2 y^1 , which is comparable to that produced by meteoroid impacts.

The above-mentioned sources are balanced by a set of sinks, which maintain the lunar exosphere in a dynamic equilibrium.

1.3.2 Sink processes

A species is able to escape the gravitational pull of a planetary body if it has energy excess to the gravitational binding energy. This excess energy may come as a result of various thermal and non-thermal processes. The relative importance of the sink processes varies from species to species. For lighter non-condensable species like Helium and H_2, it is the Jeans escape (*Jeans*, 1923) that plays a significant role. ^{40}Ar, on the other hand, is vulnerable to ionization loss (photoionization (*Huebner et al.*, 1992) and charge exchange (*Nakai et al.*, 1987)) and condensation trapping. ^{20}Ne is vulnerable to photoionization loss (*Huebner et al.*, 1992), but not condensation trapping.

- **Thermal or Jeans escape**

  Jeans escape (*Jeans*, 1923), also known as thermal or gravitational escape, is important for lighter species (H and He), where the thermal energy of an atom exceeds the gravitational binding energy. At and below the exobase (for the Moon the exobase is at its surface) the particle velocities are distributed according to the Maxwell-Boltzmann distribution (*Chamberlain*, 1963; *Armand*, 1977), given by equation 1.1. The parameter that underpins the degree of vulnerability of an atom to undergo Jeans escape is the *escape parameter* λ_{esc}, which is the ratio of the potential to the kinetic energy of the atom. Lesser the gravitational potential energy compared to the thermal kinetic energy, lesser is the value of the escape parameter and more vulnerable is the species to undergo Jeans or thermal escape.

  The escape parameter λ_{esc} is given by

$$\lambda_{esc} = \frac{GMm}{kT(R+z)} = \frac{(R+z)}{H(z)} = \left(\frac{v_{esc}}{v_0}\right)^2 \tag{1.6}$$

  Here, G is the Universal gravitational constant, M is the planetary mass, m is the mass of a given species (proton rest mass multiplied by the mass of the species in atomic mass unit), R is the radius of the planet and z is an arbitrary height above the surface. $H(z)$ represents the local scale height.

  Integration of the upward flux (velocity multiplied by the number density) assuming the Maxwell-Boltzmann velocity distribution above the exobase leads to the *Jeans formula* for the thermal escape flux (in m^{-2} s^{-1}), given by:

$$\Phi_J = \frac{N_{ex} v_0}{2\sqrt{\pi}} \left(1 + \lambda_{esc}\right) exp\left(\lambda_{esc}\right) \tag{1.7}$$

  Here N_{ex} refers to the number density of the species at the exobase. For surface boundary exospheres like Moon, it represents the surface number density.

The typical parameters for Moon are:

R= R_M = 1735×10^3 m
M = 7.342×10^{22} kg
T = 390 K, the equatorial surface temperature for sunlit lunar hemisphere
z = 0, since moon has a surface boundary exosphere
v_{esc} = 2.38×10^3 m s^{-1}
For a surface density of N_{ex} = 1×10^9 m^{-3}, for Helium (amu 4) over the equatorial region in the sunlit hemisphere of the Moon, substituting the above parameters in equations 1.6 and 1.7, λ_{esc} = 3.47 and Φ_J = 4.98×10^{10} m^{-2} s^{-1} = 4.98×10^6 cm^{-2} s^{-1}. This is the thermal evaporation rate of the Helium atoms. Thermal loss is less significant for the heavier species; which can be understood by comparing the values of the λ_{esc} for few species, calculated based on the above-mentioned lunar parameters, as shown in Table 1.2.

Table 1.2: *Calculated values of thermal escape parameter λ_{esc} for few species*

Species	*Value of λ_{esc}*
Hydrogen atom (amu 1)	0.87
Hydrogen molecule (amu 2)	1.74
Helium (amu 4)	3.47
Oxygen (amu 16)	13.90
Neon (amu 20)	17.38
Argon (amu 40)	34.77

The value of the escape parameter is directly proportional to the mass of the species. Lunar surface escape velocity (2.38 km s^{-1}) corresponds to an energy requirement of 0.03 eV/amu, equivalently 226 K amu^{-1} for a species to escape (*Stern*, 1999). Exceptions to this occur even in the collisionless regime, if during the process of escape, radiation pressure retards the velocity below the local escape speed (*Bishop and Chamberlain*, 1989; *Beth et al.*, 2016*a*,*b*), or the species is ionized and recycled to the Moon (*Manka and Michel*, 1971).

- **Non-thermal loss processes**

  Non-thermal loss processes include several physical and chemical processes. Some of them include knocking out of the atmospheric species by the solar wind particles, pick-up by the solar wind fields, etc. Like Jeans escape, these are also permanent removal processes of atmospheric species. Table 1.3 presents a list of different non-thermal processes that lead to the loss of atmospheric species.

- **Impact loss**

  Impacts by micrometeoroids may impart sufficient energy to the surface and ablate materials from the impact zone. The temperature of the vapor escaping the impact site follows a Maxwellian distribution with characteristic temperatures of 2000-5000 K, while the vapor produced by the outgassing of the ablated material produces a weighted average Maxwellian with temperatures up to $\sim$ 3000 K (*Stern* (1999) and the references therein). The ablated materials may escape if excess energy is available to circumvent the gravitational barrier. This is also a permanent removal process.

- **Condensation loss**

  Condensation occurs primarily on the lunar nightside or in the PSRs, where the solar radiation can never reach (*Paige et al.*, 2010*a*). A typical example is the trapping of Hydrogen-bearing molecules in the lunar PSR (*Lawrence et al.*, 2015) and polar regions (*Sanin et al.*, 2017). The species are adsorbed in a shallow potential well with lattice residence times comparable to or in excess of the 14-day lunar night. Condensible lunar atmospheric species include Ar, Na, and K, as well as the H_2O. Condensed species may undergo sublimation after sunrise and are released by the process of thermal desorption, and hence the condensation loss is considered a temporary sink (*Stern*, 1999). In contrary, if a condensible gas finds its way to a permanently shadowed polar cold trap, then it may be permanently lost until and unless it gathers sufficient energy from any external stimulus (meteoritic impact or SEP-induced dielectric breakdown) to be re-leleased.

- **Chemical loss**

  Collisions between exospheric atoms or molecules with the surface can result in chemical reactions leading to its bonding to the surface before being ballistically ejected again (*Stern*, 1999). It is believed to be an important loss mechanism for H^+, He, and O from solar wind impingement on the Moon.

The relative importances of the above-mentioned source and sink processes depend on the species as well as the environment they are exposed to, the understanding of which culminates to the modelling of the lunar exosphere. Lunar exospheric modelling aims at the complete understanding of the source and sink processes of the lunar exosphere, its composition and variability as well as dynamics.

Table 1.3: *Non-thermal escape processes [Taken from de Pater and Lissauer (2010)]*

Nomenclature used: i_2=molecule; i, j=atoms; i^+, j^+=ions; e^-=electron; superscript * represents energetic atom or molecule

Non-thermal escape	*Description*
Dissociation	A neutral molecule may be dissociated by UV photon or energetic electron The products may have excess energy to escape the gravity. 1. i_2+h$\nu \rightarrow i^*$+i^* 2. i_2+$e^{-*} \rightarrow i^*$+i^*+e^-
Dissociative recombination	A molecular ion may be dissociated by electron impact (EI), and the product may escape the gravity. i_2^*+$e^- \rightarrow i^*$+i^*
Ion-neutral reaction	When an atomic ion interacts with a neutral molecule, the reaction may produce an ionic molecule and a fast atom, which may eventually escape. i_2+$j^+ \rightarrow ij^+$+i^*
Charge exchange	When an energetic ion interacts with a heavier neutral atom, the ion loses its charge but retains its kinetic energy (Resonant charge exchange). Thus, the former ion becomes an energetic neutral atom, which may escape the gravity. i+ $j^{+*} \rightarrow i^+$+ j^*
Sputtering	When a fast ion (case 1) or an atom (case 2) 'knocks on' an atmospheric atom, it may gain sufficient energy to escape the gravity. In case the product does not have excess energy to escape, it remains gravitationally bound, thereby forming a corona. For surface boundary exospheres (like Moon), significant sputtering occurs at the surface. 1. i+$j^{+*} \rightarrow i^*$+j^{+*} 2. i+$j^* \rightarrow i^*$+j^*
Solar wind sweeping	In the absence of a global magnetic field (similar to that in Moon), charged particles in the atmosphere may interact with the solar wind directly. and are swept out by the solar wind fields.

1.4 Modelling of the Lunar exosphere

In his classical model, *Chamberlain* (1963) treated the dynamics of ballistic, satellite and escaping particles. *Hartle* (1971) generalized the Chamberlain model of planetary exosphere by allowing arbitrary variations of density and temperature over the exobase. For the case of the Moon, the exobase is right at the lunar surface and hence the surface temperature plays an important role in determining the desorption and velocity distribution of the lunar species. In early 1970s, the exospheric transport model did not provide a detailed description of the diurnal variation of the light species on the Moon, as *Hodges et al.* (1972) pointed out, which was attributed to the inherent difficulties in accounting for the large diurnal variation of the lunar surface temperature. *Hodges et al.* (1972) used the then available lunar surface temperature models, which were based on thermal property data acquired at the Apollo 15 and 17 landing sites. Among these two, the temperature model based on Apollo-17 measurements were considered to be well suited to compare between theory and experiments because of the simultaneous availability of the in-situ atmospheric composition data from the LACE mass spectrometer.

The Monte Carlo model used by *Hodges et al.* (1972) was meant to trace the paths of a succession of individual particles since their creation, till escape. For lighter species, like H, H_2, and He, the scale heights exceed the vertical scales of orographic features and hence the lunar surface was assumed to be smooth with constant gravitational potential. For the solar wind-borne species, like H^+ and He^{++}, their influx was assumed to vary as the cosine of the lunar-centric angle from the subsolar point to the point of interest.

In the Monte Carlo model, the origin of a lunar species is chosen randomly by fixing the co-latitude (θ_0) and the longitude (ϕ_0). Based on the temperature model, the surface temperature (T) at the location (θ_0, ϕ_0) is determined. The velocity v of the species is randomly chosen based on the Maxwell-Boltzmann velocity distribution with characteristic temperature T. The velocity components are randomly chosen from three Gaussian deviates. The magnitude of the velocity (v) is then compared with the lunar surface escape velocity (v_e). If $v \geq v_e$, an escape event is recorded and a new particle is created. In case the particle did not escape, its point of impact on the lunar surface is computed based on orbital mechanics. The loop repeats itself by treating the point of impact as the point of origin for the next iteration.

Since Moon's is a Surface Boundary Exosphere, it is sensitive to the orograhic features, gravitational anomalies and surface temperature fluctuations. The lunar exospheric model underwent evolution with the advancement of knowledge in the field of lunar surface science. As a result, the Monte Carlo model by *Hodges et al.* (1972) evolved to the Lunar Exospheric Simulation (LExS) toolkit (*Hodges and Mahaffy*, 2016). As for example, the lunar terrain varies by $\sim$20 km in altitude (*Hodges and Mahaffy*, 2016), which is comparable with the lunar exospheric scale heights. To accommodate this, the lunar

exospheric model has undergone refinement by adopting the lunar topographic model derived from Lunar Orbiter Laser Altimeter (LOLA) data with lateral resolution of 500 m. This makes the LExS model capable of accounting for the effects of topography on insolation. Thus, the spatial variations of the lunar surface temperature near the terminator, the poles, in small craters and otherwise rough terrain are accounted for in the LExS. The incorporation of topographical model has enhanced the computational accuracy of the orographical effects on the points of origin and impact as well as the extents of the ballistic trajectories of the species over the terrain.

As mentioned, another important factor that governs the density and dynamics of the lunar exospheric species is the surface temperature. The lunar exospheric model is further refined by the incorporation of the surface temperature model (*Hurley et al.*, 2015), based on the mapping of the lunar infrared albedo by the Diviner Lunar Radiometer aboard LRO (*Paige et al.*, 2010*a*,*b*). For a point on the lunar surface with colatitude θ and longiture ϕ with solar zenith angle ψ, the surface temperature is given by the following set of analytic functions, as proposed by *Hurley et al.* (2015):

$$T(\psi) \;=\; 392\, cos^{1/4}(\psi) \qquad for \;\; \psi < 90^{\circ} \tag{1.8}$$

$$T(\theta, \phi) \;=\; \sum (a_i \phi^i) \;+ 35(sin(\theta) - 1) \qquad for \;\; \psi > 90^{\circ} \tag{1.9}$$

Here i runs from 0 to 5 with the coefficients given by

$$a \;=\; [444.738, -448.937, 239.668, -63.8844, 8.34064, -0.423502]$$

This yields an equatorial day-side temperature as 392K. At equator, the function suggests 130 K surface temperature at post-dusk and 95 K at pre-dawn. More detailed results on the lunar surface temperarture mapping based on the Diviner radiometer measurements are also reported recently (*Williams et al.*, 2017).

The LExS toolkit is being refined with the progress of knowledge of the lunar science (private communication with Dr. R. R. Hodges). In-situ and remote sensing observations of the lunar exosphere play a major role in the refining of the lunar exospheric model. Figure 1.6 presents a summary and time-line of the lunar missions that have contributed to the present understanding of the lunar exosphere. The next section presents a brief discussion on the observations on the lunar exosphere made by several lunar missions.

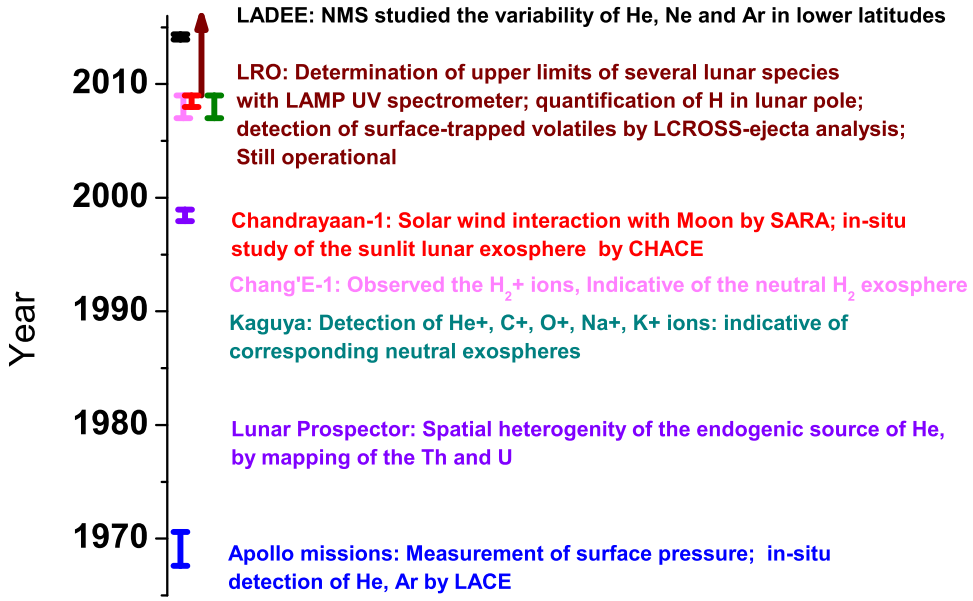

Figure 1.6: Summary and time-line of the lunar missions that have contributed to the present understanding of the lunar exosphere. The only three missions that conducted in-situ study of the lunar neutral exosphere are Apollo (LACE in Apollo-17) in 1972-1973, Chandrayaan-1 (CHACE aboard MIP) in 2008 and LADEE (the NMS) in 2013-2014.

1.5 Observations on the lunar exosphere

1.5.1 The Apollo observations (1969-1972)

The three Cold Cathode Gauge Experiments (CCGE), flown in the the Apollo-12, 14 and 15 Surface Experiment Packages determined the surface density of $\sim 10^7$ atoms cm^{-3} and $\sim 10^5$ atoms cm^{-3} during the lunar day and night, respectively (*Johnson et al.*, 1972). Since there was no in-situ composition measurement at the time of the Cold Cathode Gauge experiments, the reported surface densities were with the assumption that molecular Nitrogen (N_2) dominated the composition. Hence, an uncertainty by a factor of two was associated with the surface density reported by the Cold Cathode Gauge, in order to accommodate the relative ionization sensitivities of the potential lunar species. The Apollo instruments got saturated during lunar day, leaving a gap in the measurement of the day side pressures. However, there had been no ambiguity in the night time values due to the prevailing low temperatures.

In-situ detection of the lunar exospheric noble gases traces back to the Apollo era, when the mass spectrometers flown aboard the Apollo 15 and 16 spacecraft probed the

lunar exosphere (*Hoffman et al.*, 1972), but with limited success. A significant step to study the lunar exospheric composition was accomplished by the Lunar Atmospheric Composition Experiment (LACE) (*Hoffman et al.*, 1973), deployed on the Taurus-Littrow Valley with its entrance aperture oriented upward to intercept and measure the downward flux of the lunar exospheric gases. LACE was a magnetic sector mass spectrometer, which was a part of the Apollo Lunar Surface Experiment Package (ALSEP) in the Apollo-17 mission. LACE analyzed the constituents of the lunar neutral exosphere at the surface. The LACE instrument ran into saturation during lunar days and hence provided useful scientific information only during lunar nights. Starting from December 1972, it continued to operate for nine lunations before it developed some anomaly in the instrument during the tenth lunation (October 1973) (*Hoffman*, 1975). The noble gases detected unambiguously in the lunar exosphere were Helium and Argon. Figure 1.7 shows the diurnal variation of He and Ar as observed by LACE. It is observed that He and Ar have different diurnal variability because of the fact that the former is non-condensable while the latter is condensable under lunar temperature and pressure conditions. Ar density minimizes at night because of the condensation loss, while the He density maximizes post-midnight. The ^{20}Ne signature, on the other hand, observed by LACE was believed to be contaminated by the signal of $H_2^{18}O$ from Apollo equipment (*Hodges et al.*, 1973).

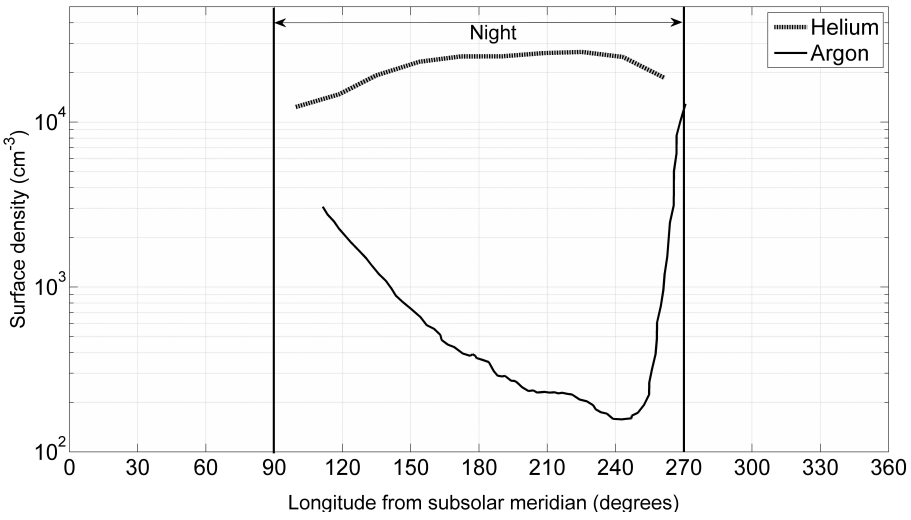

Figure 1.7: Trends of diurnal variation of the lunar He and Ar as observed by LACE. The He values are averaged over ten lunations. The Ar measurements correspond to 20 July to 3 August 1973. Subsolar meridian of 180° represents local midnight. Succesful observations by LACE were limited to the lunar nightside. Redrawn based on the Figs. 2 and 3 from *Stern* (1999). Original data are from *Hodges* (1975).

The absence of species, like H, C and N, in the lunar exosphere is attributed to their conversion to H_2, CH_4 and NH_3 (*Hodges et al.*, 1972). Further, the usage of LACE data for setting up an upper limit for the H_2 had been supported by the ultraviolet spectrometer, which is free of contamination. Though the Apollo 17 mass spectrometer detected species

with atomic mass 16, 18 and 44, more favorably during pre-sunrise conditions (*Hodges*, 1975), they were considered of terrestrial origin carried along with the instrument.

On the other hand, the mass spectrometers flown in the orbiters Apollo 15 and 16 were believed to have been so heavily dominated by the contaminants from the orbiter module, that no detection or upper limits could be obtained (*Hodges et al.*, 1972). Therefore, all the in-situ measurements attempted in the past had the problem of possible contamination. The UV observations aboard Apollo-17, meant to detect resonance fluorescence emissions characteristic of lunar exospheric species, did not yield any significant positive results (*Fastie et al.*, 1973). It was inferred that nearly 100 percent of the solar wind protons should have been converted into H_2 and have arrived at upper limits for H, O, C, N, Kr, Xe, H_2 and CO. No significant improvement was reported even by revisiting the Apollo-17 UV spectrometer data with improved resonance fluorescence g-factors (*Feldman and Morrison*, 1991).

1.5.2 Observations by Lunar Prospector (1998-1999)

NASA's Lunar Prospector mission was launched on 7 January 1998 and it continued till 31 July 1999. Lunar Prospector conducted remote sensing of the Moon from a 100 km polar orbit. Two important findings of the mission as far as the lunar exosphere is concerned was the mapping of the radioactive materials (*Lawrence et al.*, 1999), like Thorium, Uranium and Potassium on the lunar surface. The radioactive decay process is an endogenic source of the lunar He atoms (*Heiken et al.*, 1991; *Hodges*, 1975; *Benna et al.*, 2015) with a supply rate of $\sim (4.5 \pm 1.2) \times 10^6$ atoms cm^{-2} s^{-1} (*Grava et al.*, 2015*a*). The Lunar Prospector neutron spectrometer conducted high resolution mapping of the polar Hydrogen in the permanently shadowed regions in the lunar poles (*Lawrence et al.*, 2015).

1.5.3 Observations by Kaguya (2007-2009)

The Japanese mission Kaguya (SELENE) was launched on 14 September 2007 and it continued to operate until 10 June 2009. Kaguya studied the Moon from a 100 km circular, and later from a 30-50 km polar orbit. The MAP (MAgnetic field and Plasma experiment) was a suit of scientifc instruments aboard Kaguya.

The Ion Mass Analyzer (IMA) of the MAP-PACE detected reflected/scattered solar wind ions with energies of $\sim$ 1 keV, while the IEA detected the solar wind ions (with energy $\sim$ 2 keV) directly. The origin of the ions with energy ranging between 10 to 800 eV detected by IMA was attributed to the lunar surface and exosphere.

The detected lunar ions were composed of He^+, C^+, O^+, Na^+ and K^+ (*Yokota et al.*, 2009). The Na and K exospheres of Moon was found earlier (*Potter and Morgan*, 1988),

using ground based spectroscopy. Model simulations have been used to understand the corresponding neutral exospheres from these ion measurements (*Hartle et al.*, 2009).

In addition to the detection of the lunar ions, the Gamma Ray Spectrometer aboard Kaguya yielded high resolution maps of the radioactive Thorium, Uranium and Potassium on the lunar surface (*Hasebe et al.*, 2009; *Kobayashi et al.*, 2010; *Yamashita et al.*, 2010), which are localized endogenic sources of the lunar exospheric He atoms. These maps have helped to understand the distribution of the endogenic sources of He in the lunar exosphere.

1.5.4 Observations by Chang'E-1 (2007-2009)

The Chinese lunar mission ChangE-1 was launched on 24 October 2007; it was operated until 01 March 2009. Chang'E-1 carried onboard Solar Wind Ion Detectors (SWID, consisting of two mutually perpendicular Electro Static Analysers (ESA), both viewing up towards the space (*Wang et al.*, 2011). The energy-time spectrogram of the SWID revealed parallel curve (PC) structures. In the parallel curve (PC) structures, a component is due to a flux of ions with energy $\sim$ 8 times greater than the solar wind proton energy (*Wang et al.*, 2011).

Energy analysis showed that the ions had m/q = 2, indicative of either H_2^+ or He^{2+} ions. Based on the comparison between the observed flux of the ions and the possible H_2^+ or He^{2+} flux levels estimated based on the production rates of H_2^+ and He^{2+}, it was inferred that the observed pick-up ions were H_2^+, which originated from the ionizing processes like photoionization, charge exchange, electron impact ionization, etc. of the lunar neutral H_2. This was the first observation of the lunar pick-up H_2^+ ions, which served as an evidence for the lunar neutral H_2 exosphere.

1.5.5 Observations by Chandrayaan-1 (2008-2009)

The Indian mission to Moon Chandrayaan-1 was launched on 22 October 2008, it reached the lunar orbit on 8 November 2008 and subsequently it was operational for a period of ten months. Chandrayaan-1 carried a piggyback 34 kg microsatellite called the Moon Impact Probe (MIP) (*Kumar et al.*, 2009), which was released from an altitude of 98 km to the lunar surface on 14 November 2008. MIP carried a neutral mass spectrometer called Chandra's Altitudinal Composition Explorer (CHACE), which conducted in-situ studies of the altitudinal and latitudinal distribution and composition of the sunlit lunar exosphere with 1 to 100 amu mass range. The observations made by CHACE about the distribution of the lunar exospheric Ar, Ne, He and H_2 form the the basis of the research presented in this thesis.

In addition to CHACE, there were ten more experiments in the Chandrayaan-1 orbiter exploring the Lunar ambience and also the surface features of the Moon (*Goswami and Annadurai*, 2009). Chandrayaan-1 observed the Moon to study its mineralogy at visible and infrared wavelengths with instruments Hyper Spectral Imager (HySI) covering 400 nm to 950 nm wavelength range (with 15 nm resolution); infrared spectrometer SIR-2 covering 900 nm to 2400 nm wavelength (with 6 nm resolution) and the Moon Mineralogy Mapper (M^3) covering the wavelength range of 700 nm to 3000 nm (with 10 nm resolution). The M^3 instrument inferred the presence of water ice on the lunar surface in the higher latitudes and the polar regions based on the remote sensing of the spectral signature of OH (*Pieters et al.*, 2009). There were High Energy X ray (HEX) and Chandrayaan-1 X ray Spectrometer (C1XS) experiments aboard Chandrayaan-1 for the study of transportation of volatiles and study of the fluorescent signatures of minerals, respectively. The RAdioation DOse Monitoring (RADOM) studied the lunar radiation environment. The Mini-Synthetic Aperture Radar (Mini-SAR) instrument was used for the subsurface studies. The Terrain Mapping Camera (TMC) and Lunar Laser Ranging Instrument (LLRI) were optical instruments for mapping of the lunar terrain and studying the surface topography. The Sub-keV Atom Reflecting Analyzer (SARA) experiment onboard Chandrayaan-1 consisted of two sensors, *viz.* CENA (Chandrayaan-1 Energetic Neutral Atom Analyzer) and SWIM (Solar Wind Monitor) (*Bhardwaj et al.*, 2005; *Barabash et al.*, 2009). CENA detected energetic neutral atoms (ENAs), while the SWIM measured ions of solar wind origin. The SARA suit of instruments provided clues to the solar wind forcing on the Moon and has provided important results on the lunar exosphere.

The SARA experiment discovered substantial and sustained backscattering of solar wind protons from lunar surface as energetic neutral Hydrogen atom contributing to the neutral Hydrogen exosphere of the Moon (*Wieser et al.*, 2009; *Vorburger et al.*, 2013; *Bhardwaj et al.*, 2015). They also suggested the entry of solar wind protons to the lunar wake region (*Futaana et al.*, 2010; *Dhanya et al.*, 2013), which may cause sputtering of neutrals from the night-side lunar surface thereby contributing to the night-side exosphere (*Vorburger et al.*, 2016; *Dhanya et al.*, 2016). The CENA instrument indicated the backscatter of a fraction of the solar wind alpha particles as energetic He atom (*Vorburger et al.*, 2014).

1.5.6 Observations by LAMP/LRO (2009-present)

A more recent lunar mission had been the NASA's LRO mission, which was launched on 18 June 2009. The Lyman Alpha Mapping Project (LAMP) far-ultraviolet (FUV) spectrograph aboard LRO (*Gladstone et al.*, 2010*a*) detected several lunar exospheric species including the major noble gases in its limb viewing mode. It covers a wavelength range of 57.5 nm to 196.5 nm (*Stern et al.*, 2012). LAMP observed the lunar exosphere by

viewing the sunlit part of the exosphere while the lunar surface was dark.

Lunar H_2 was detected by the LAMP in the vapour plume emanated from the impact of the LCROSS into the permanently shadowed Cabeus crater (*Gladstone et al.*, 2010*b*). In addition to this, the regular LAMP observations at Lyman and Werner bands detected lunar exospheric H_2 (*Cook et al.*, 2013; *Stern et al.*, 2013).

Helium was detetecd by LAMP in the lunar exosphere using the 58.4 nm emission ($1s2p \rightarrow 1s^2$) line (*Stern et al.*, 2012). LAMP inferred the Helium surface density of $\sim 2 \times 10^4\ cm^{-3}$ (*Feldman et al.*, 2012) during local dawn. LAMP results further suggested that instead of all the alpha particles from the solar wind incident on the lunar surface being thermalized, a significant fraction ($\sim$50%) of them escape as suprathermal Helium or backscattered from the lunar surface.

LAMP also studied the lunar Argon at 104.8 and 106.7 nm fluorescent emission ($3s^23p^54s \rightarrow 3s^23p^6$) wavelengths, corresponding to the fluorescent emission of the sunlit Argon in the lunar exosphere in the background of the dark surface. An upper limit of 2.3 $\times$ 10^4 cm^{-3} is reported for Argon (*Cook et al.*, 2013), which is $\sim$1.5 times lower than the upper limit given by LACE (*Hodges and Hoffman*, 1975).

For lunar Neon, *Cook et al.* (2013) reported an upper limit of 4400 cm^{-3} for its surface number density based on the observation of 63 nm ($2s^22p^54s \rightarrow 2s^22p^6$) and 73.5 nm ($2s^22p^53s \rightarrow 2s^22p^6$) spectral lines from the LAMP instrument.

The LAMP instrument also yielded the upper limits of the surface densities for some of the species (*Cook et al.*, 2013; *Feldman et al.*, 2012; *Stern et al.*, 2013), a summary of which is presented in Table 1.5.

Recently, *Sanin et al.* (2017) presented polar maps of the Moons inferred hydrogen abundance based on Lunar Exploration Neutron Detector (LEND) instrument.

1.5.7 Observations by LCROSS (2009)

The Lunar Crater Observation and Sensing Satellite (LCROSS) sent an impactor to strike the Cabeus crater (84.675°S, 311.281°E) on 9 October 2009, nearly at the local noon (LST of 11:34 hours), in order to explore the volatiles trapped in the lunar polar soil. The plume generated by the LCROSS impact was observed with the LAMP instrument aboard the LRO. The far-ultraviolet emissions from the fluorescence of sunlight by molecular hydrogen (H_2) and carbon monoxide (CO), as well as resonantly scattered sunlight from atomic mercury (Hg) with contributions from calcium (Ca) and magnesium (Mg) were observed. The observed signatures were well simulated by expansion of a vapour cloud at a temperarture of $\sim$ 1000 K, containing $\sim$570 kg of CO, $\sim$140 kg of H_2, $\sim$160 kg of Ca, $\sim$120 kg of Hg, and $\sim$40 kg of Mg (*Gladstone et al.*, 2010*b*). The ejecta plume also

showed the signatures of other volatile compounds, like H_2O, H_2S, NH_3, SO_2, C_2H_4, CO_2, CH_3OH, CH_4, OH (*Colaprete et al.*, 2010) and Na (*Killen et al.*, 2010).

Table 1.5: *The derived upper limits of surface densities some of the lunar species at day-night terminators from LAMP. Adopted from Cook et al. (2013); Feldman et al. (2012); Stern et al. (2013)*

Species	*Wavelength (nm)*	*Surface density (cm^{-3})*
	Species discussed in this thesis	
He	58.4	2.0×10^4
Ne	63.05	4.4×10^3
Ar	104.82	2.3×10^4
H_2	Lyman and Werner bands	1.2×10^3
	Other species detected	
H	102.57	24
B	182.57	0.46
C	165.69	1.6
C^+	133.57	0.63
N	113.5	340
N^+	108.57	130
O	130.49	5.4
O^+	83.45	680
Mg	182.79	3.4
Al	176.64	1.1
Si	184.55	0.90
P	177.5	4.2
S	180.73	2.3
Cl	133.57	15
Ca	188.32	16
Sc	174.47	24
Mn	178.53	78
Fe	185.17	45
Co	182.24	41
Zn	158.96	220
As	189.04	1.4
Xe	146.96	3.0×10^3
Au	187.98	1.1×10^3
Hg	184.95	39
CO	151.0	710

1.5.8 Observations by NMS/LADEE

The Lunar Atmospheric and Dust Environment Explorer (LADEE) (*Elphic et al.*, 2014) conducted in-situ studies of the equatorial (limited to $\pm 23^{\circ}$ latitude) lunar exosphere from December 2013 to April 2014 covering an altitude range of 61 km down to 4 km. LADEE carried the Neutral Mass Spectrometer (NMS) instrument that studied the lunar exosphere in the mass range of 2 to 150 amu. In spite of the wide mass range covered, emphasis has been given only to the noble gases detected by the instrument. LADEE has discovered the presence of Ne in the lunar exosphere and has studied the distribution and variabilities of He, Ne and Ar in the equatorial latitudes (*Benna et al.*, 2015). Figure 1.8 shows the diurnal variation of the surface density of He and Ne derived from the NMS observations. It is observed that, since both He and Ne are non-condensable under lunar temperature and pressure conditions, the behaviour of their diurnal variations are similar. He maximizes between 2 and 3 AM local time while Ne maximizes just before sunrise.

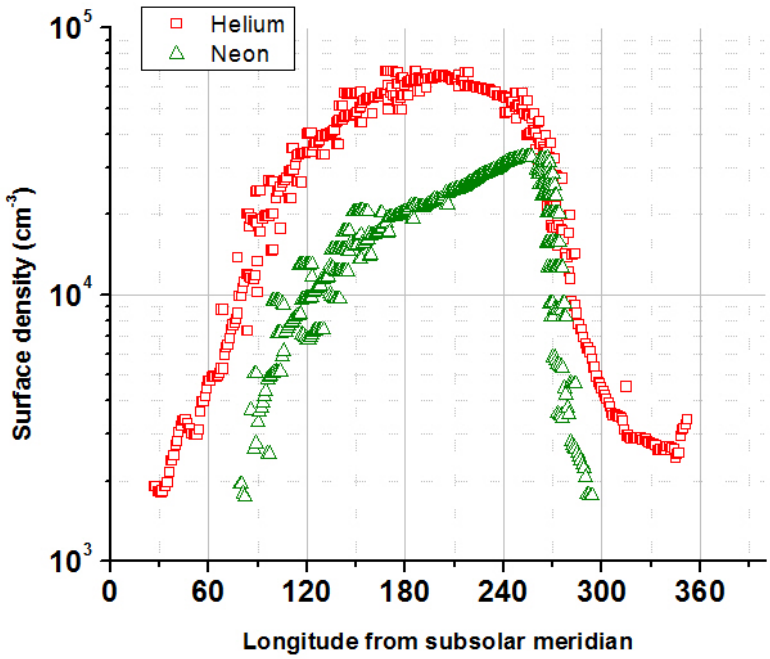

Figure 1.8: Diurnal variation of the surface density of He and Ne as derived from the NMS observations. The longitudes from the subsolar meridian 90°, 180° and 270° represent local dusk, midnight and dawn, respectively. [Redrawn based on the Figures 2 a and c from *Benna et al.* (2015)].

It is also confirmed by NMS that the exospheric He is controlled by solar wind and by endogenous radiogenic sources. In spite of the significant differences in the source strengths due to the higher lifetime (few months) of Ne as compared with He (few days), the nightside concentrations of Ne and He are comparable (*Benna et al.*, 2015). Localized enhancement of Ar is observed at the Western maria, coincident with the potassium-rich

KREEP (Potassium, Rear Earth Elements and Phosphorus) regions, vindicating the close interaction between the surface and the exosphere, characteristic to the surface boundary exospheres (*Benna et al.*, 2015).

The NMS data have also revealed synodic and semiannual oscillations of ^{40}Ar of the lunar exosphere (*Hodges and Mahaffy*, 2016). The semiannual oscillation of Ar is found to be consistent with condensation loss in the seasonal cold traps at the poles due to the obliquity of the Moon. The results show that the exospheric morphology depends on the energetics of desorption of atoms from soil grains. It also brought out the importance of the surface-exosphere interaction process.

The Ultraviolet Spectrometer (UVS) aboard LADEE brought out the variabilities of the lunar exosphere during the passage of the Moon through the Earth's magnetotail and meteoroid systems by studying the resonant scattering from exospheric Na and K. Factor of ~ 2 enhancement of the Na and K exospheres during the passage of the Moon through three meteoroid systems are reported (*Colaprete et al.*, 2016).

1.5.9 Coordinated observations

The LAMP UV spectrometer aboard LRO and the NMS aboard LADEE were simultaneously operated during the five-month span of the LADEE mission to study the lunar Helium exosphere. The "Acceleration, Reconnection, Turbulence and Electrodynamics of Moon's Interaction with the Sun"(ARTEMIS) mission simultaneously monitored the solar wind alpha particle flux to the Moon (*Hurley et al.*, 2016). The correlation between the fluctations of the solar wind alpha particle flux and the variations in the lunar exospheric He was studied. It was found that the solar wind contributes 64 ± 5 % of the He to the lunar exosphere, while the remaining may be endogenic to Moon, arising out of radioactive decay of ^{232}Th and ^{238}U. It was also suggested through these coordinated observations that 63 ± 6 % of the incident solar wind alpha particles are converted to the thermalized He atoms by surface-interactions, while the rest may be backscattered as He^{++} or Energetic Neutral Atoms (ENA) (*Vorburger et al.*, 2014; *Hurley et al.*, 2016; *Grava et al.*, 2016).

1.6 Motivation and scope of the present work

The noble gases are good tracers to study the different processes in the lunar exosphere since they do not react to form compounds. Reviewing all the major findings on the lunar neutral exosphere, it stands out that the day-time lunar exosphere remains uncharacterized in terms of the latitudinal and altitudinal variations of the noble gases. Study of the latitudinal variation of the noble gases in the day-time lunar exosphere is important, as it highlights the variation of the lunar surface temperature due to the variation of the solar

incidence angle, thereby affecting the dynamics of the lunar species by modulating their velocity distributions. The latitudinal variation of the surface obliquity also brings in a variation of the flux level of the solar wind as well as EUV photons on the surface, which, in turn, influences several source and sink mechanisms in the lunar exosphere.

The present work focuses on the latitudinal and altitudinal distribution of the lunar exospheric noble gases during lunar daytime, based on the in-situ observations of the dayside lunar exosphere by CHACE aboard MIP in Chandrayaan-1. This include studies on the spatial distribution of ^{4}He, ^{20}Ne and ^{40}Ar in the lunar exosphere. In addition to the noble gases, results on the lunar H_2 are also discussed. Lunar H_2 is a result of the conversion of the solar wind Hydrogen implanted to the regolith (*Hodges et al.*, 1972; *Hurley et al.*, 2017). Hence the lunar regolith is a reservoir of the lunar H_2. The H_2 molecule is sensitive to dissociation to H and thermal escape. Hence, the study of the lunar H_2 provides clues on the lunar surface processes.

The **second chapter** presents the instrumentation and operation details of the CHACE instrument and the MIP. The working principle and the development of CHACE as well as the critical aspects of its calibration, testing and space qualification are also discussed in this chapter. The observation and the analysis methodology are also included in this chapter.

The **third chapter** deals with the Lunar Argon, which is mostly ^{40}Ar, while the solar wind Argon is rich in ^{36}Ar (*Wieler*, 2002). This is because the lunar ^{40}Ar is a result of the radioactive decay of the ^{40}K in the lunar interior, which upon release into the exosphere remains gravitationally bound. Hence, the study of ^{40}Ar tells about the internal release processes of gases from the Moon. ^{40}Ar is condensable under the prevailing lunar ambient temperature and pressure conditions in the night side and also in the permanently shadowed regions and hence it has close interaction with the regolith through the process of adsorption and desorption. The observation of CHACE on the ^{40}Ar is presented and the ^{40}Ar: ^{36}Ar ratio is computed along the 14°E lunar meridian. An altitude versus latitude map of the lunar Ar along the above-mentioned meridian is also described. The new results presented in this chapter are the spatial heterogeneity of the radiogenic activity of the lunar interior and its possible relation to the surface topography.

The **fourth chapter** discusses about the observations on lunar exospheric Ne. Lunar Ne is derived from the solar wind and is primarily lost through photoionization. Ne is non-condensable under the lunar temperature and pressure conditions. It is shown from the CHACE observations that Ne obeys the law of exospheric equilibrium for non-condensable gases, originally proposed by *Hodges and Johnson* (1968). The new results presented in this chapter include an empirical relation between the lunar Ne surface density and surface temperature. The empirical relation provides a first order estimate on the surface density of Ne using the surface temperature information.

The **fifth chapter** deals with the observation of He. Lunar He, which is mostly ^{4}He, is derived primarily from the solar wind alpha particle flux, although there is a secondary endogenic source of the lunar He owing to the radioactive decay of ^{232}Th and ^{238}U (*Heiken et al.*, 1991; *Hodges*, 1975; *Benna et al.*, 2015). The abundance of the lunar He directly depends on the solar wind alpha particle flux; decreases during the day-time due to the expansion of the He-corona and Jeans escape; and also decreases during the passage of the Moon through Earth's magnetotail due to the shielding of Moon from the solar wind. When CHACE conducted the in-situ study of the lunar exospheric constituents, the solar wind alpha particle flux levels were low, the surface was sunlit and the Moon was within the Earth's magnetotail. Thus, the number density of He was found to be mostly below the detection limit of CHACE. The outcome of this study is the proposed upper limit of the surface density of He in the sunlit lunar exosphere, when Moon is in Earth's magnetotail, and solar wind alpha particle flux is low. This result is expected to provide realistic constraints to the lunar He exosphere models under such an extreme condition.

The **sixth chapter** presents the observations of CHACE on the lunar exospheric H_2. It is known that the solar wind implants H^+ on the lunar regolith, a part of which is converted to H_2 (*Hodges et al.*, 1972; *Crider and Vondrak*, 2002; *Hurley et al.*, 2017), thus making the lunar regolith a reservoir of the H_2 gas. Hence, although not a noble gas, the lunar H_2 provides valuable information on the surface processes on the Moon. This chapter presents the variation of the surface density of H_2 with latitude. An altitude versus latitude map of the lunar H_2 along the 14°E meridian is also presented.

Finally, the **seventh chapter** summarises the major scientific findings of the present work. The scientific outcome of this research is expected to add value to the understanding of the composition and distribution of the noble gases in the sunlit lunar exosphere, by setting realistic boundary conditions for the lunar exospheric models. This chapter also discusses the open questions on the global characterization of the lunar exosphere and its variabilities. A polar orbiting satellite with a mass spectrometer aboard may address the yet-unsolved issues and advance our knowledge on the lunar exosphere.

Chapter 2

Moon Impact Probe and the CHACE experiment

It is a capital mistake to theorize before one has data.

—Sherlock Holmes

2.1 The MIP aboard Chandrayaan-1

2.1.1 Introduction

In this chapter, the MIP and the CHACE instrument are described. This includes a semi-analytical description of the physics of a transmission type Quadrupole Mass Analyzer (QMA), which is followed by a description on the CHACE instrumentation, along with its calibration, test & evaluation, mission operation and data analysis aspects.

2.1.2 The Moon Impact Probe Mission

The MIP was a 375 mm $\times$ 375 mm $\times$ 470 mm microsatellite with mass $\sim$ 34 kg (*Kumar et al.*, 2009) attached as a piggyback to the Chandrayaan-1 orbiter, as shown in Figure 2.1. MIP consisted of three payloads, viz. Moon Imaging System (MIS) to take colour pictures of the Moon, a Radar Altimeter (RA) to measure the instantaneous altitude of the MIP during its descend, and Chandra's Altitudinal Composition Explorer (CHACE) — the quadrupole mass spectrometer to conduct in-situ measurements of the composition of the lunar neutral exosphere (*Kumar et al.*, 2009; *Goswami and Annadurai*, 2009). Figure 2.2 shows the location of the CHACE instrument inside the MIP.

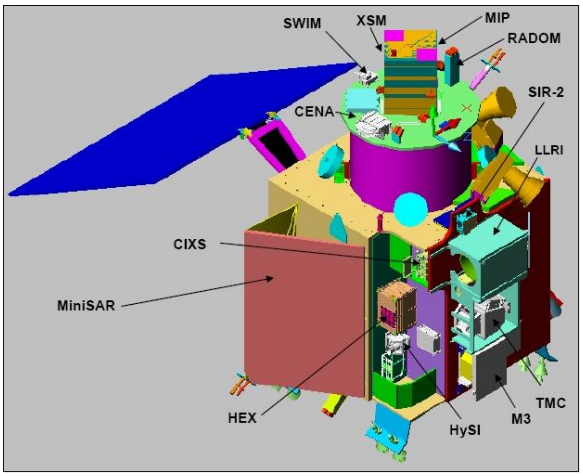

Figure 2.1: Schematic of Chandrayaan-1 with the MIP attached as a piggyback microsatellite on the top deck.

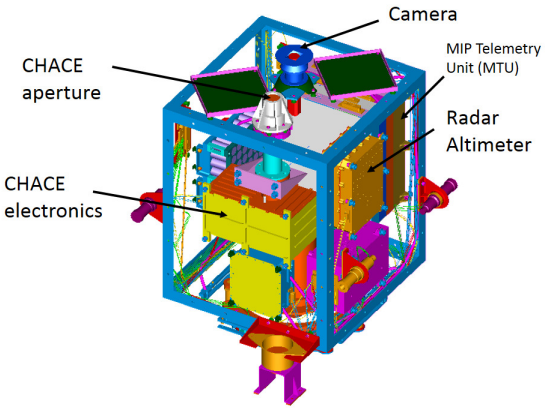

Figure 2.2: Schematic of the MIP showing the payloads.

2.2 The CHACE instrument

CHACE is developed at Space Physics Laboratory (SPL), VSSC (with the collaboration of other entities in VSSC), around a laboratory-grade open source neutral mass spectrometer with a transmission type Quadrupole Mass Analyzer (QMA) and a Bayard-Alpert (B/A) gauge. It consists of a cylindrical sensor probe, attached to the electronics. The aperture of the sensor protrudes out of the MIP top deck, while the sensor and the electronics were inside the MIP, as shown in Figure 2.2. Figure 2.3 shows the picture of the flight model of the CHACE instrument. Table 2.1 presents the specifications of the CHACE instrument.

In the following subsection, a semi-analytical description of the working principle of a transmission-type QMA will be presented. It will be followed by a description of the QMA of CHACE and an overall system-level description of the payload.

Figure 2.3: Flight model of the CHACE instrument.

Table 2.1: *Specifications of the CHACE instrument*

Mass range	1 to 100 amu
Mass resolution	1 amu
Sensors	QMA, B/A Gauge
Detector	Faraday Cup, Channel Electron Multiplier (CEM)
Interfaces	Power and data (RS232)
Instrument mass	3.15 kg
Raw power	25 W

2.2.1 Physics of the transmission-type QMA

A quadrupole mass spectrometer is a path-stability based instrument to analyze the composition of different gas atoms and molecules. This is often referred to as a transmission quadrupole (*Young*, 2002) as opposed to quadrupole traps. A quadrupole mass spectrometer has potential space applications because of its compact size, non-requirement of any magnetic field and a linear mass axis (*Dawson*, 1976; *Young*, 2002). The electric field used in the QMA varies typically from 10^2 V m^{-1} to 10^4 V m^{-1} for filtering the ions in the mass range of 1 to 100 amu, and because of this electric field the force experienced by the ions inside the QMA is typically 10^2 to 10^4 times greater than that experienced by them due to the Earth's magnetic field. Therefore, the trajectories of the ions inside the QMA are decided by the applied electric field.

Here, the basic theory of the transmission QMA (*Dawson*, 1976) will be introduced in a semi-analytical approach, before the specific details of the QMA of CHACE are addressed.

A QMA consists of four conductive rods, ideally of hyperbolic cross section, arranged at an angular separation of 90°, as shown in Figure 2.4. Cartesian coordinate system is adopted for the description of the QMA, as shown in the figure, with the cross section of the rods in the x-y plane while the z axis is normal to the x-y plane, directed towards the reader (right handed coordinate system). The minimum distance between two opposite rods is denoted by $2r_0$.

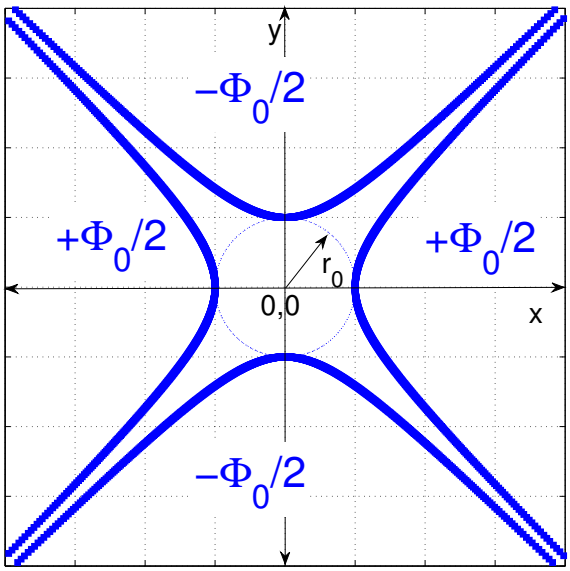

Figure 2.4: Cross section of the Quadrupole Mass Analyser rods with hyperbolic geometry

All the four rods are applied with electric potentials. Let us assume that the potentials applied at the top and bottom rods in Figure 2.4 be $-\Phi_0/2$ and that at the left and right rods be $+\Phi_0/2$. Thus, the opposite pair of rods are applied with potentials of opposite polarities. We first assume that these potentials are constant with respect to time (i.e. DC potentials).

A quadrupole field is expressed as a linear function of the position coordinates (x,y). In Cartesian coordinate system, the quadrupole electric field is expressed in the x-y plane as

$$\overrightarrow{E} = \hat{i}\lambda x + \hat{j}\sigma y \tag{2.1}$$

where λ, σ are arbitrary constants, while $\hat{i}$ and $\hat{j}$ represent the unit vectors along the x and y axes, respectively.

The quadrupole potential function, say, $\Phi(x, y)$ in the region enclosed by the four quadrupole rods, obeys Laplace's equation assuming the presence of no space charge, and hence,

$$\overrightarrow{\nabla}.\overrightarrow{E} = 0 \tag{2.2}$$

and since field is the negative gradient of the potential,

$$\Phi = -\frac{1}{2}\left(\lambda x^2 + \sigma y^2\right) \tag{2.3}$$

The constraint posed by the Laplace's equation eliminates one of the two arbitrary constants in the Equation (2.3) as

$$\lambda + \sigma = 0 \tag{2.4}$$

Thus, the potential energy function retains only one arbitrary constant and is expressed as

$$\Phi = \frac{\lambda}{2}\left(y^2 - x^2\right) \tag{2.5}$$

The second arbitrary constant is eliminated by imposing the following boundary conditions:

At $x = 0$, $y = \pm r_0$ the potential $\Phi = -\Phi_0/2$. This yields $\lambda = -\frac{\Phi_0}{r_0^2}$. Thus, Equation (2.5) reduces to

$$\Phi(x, y) = \frac{\Phi_0}{2r_0^2}\left(x^2 - y^2\right) \tag{2.6}$$

Let us now introduce a positive ion (hereafter will be referred to as ion) with mass m and charge q in the space under the influence of the quadrupole field given by Equation (2.6). The force experienced by the ion in the x and y directions are given by:

$$m\ddot{x} = qE_x = -q\frac{\partial \Phi}{\partial x} = -q\frac{\Phi_0}{r_0^2 x} \tag{2.7}$$

$$m\ddot{y} = qE_y = -q\frac{\partial \Phi}{\partial y} = +q\frac{\Phi_0}{r_0^2 x} \tag{2.8}$$

The equations of motion of the ion in the x and y directions are, respectively:

$$\ddot{x} + \left(q/mr_0^2\right)\Phi_0 x = 0 \tag{2.9}$$

and

$$\ddot{y} - \left(q/mr_0^2\right)\Phi_0 y = 0 \tag{2.10}$$

Note the differences in sign in equations (2.9) and (2.10). As we have assumed Φ_0 to be constant, the motion of the ion in the x direction will be simple harmonic, with characteristic frequency of

$$\omega_p = \sqrt{\frac{q}{mr_0^2}\Phi_0} \tag{2.11}$$

A notable feature of the above equation is that the characteristic frequency ω_p of the ion is inversely proportional to the square root of its mass per unit charge. Heavier the ion, lesser will be the characteristic frequency. For lighter ions, the characteristic frequency will be greater.

At the same time, the motion of the ion along the y direction will be unstable, i.e. the solution of y will diverge with time. This may be visualized as a ball on a saddle (see Fig. 2.5). The saddle is concave along the x direction and convex along the y direction. Hence, if the ball is disturbed from its equilibrium and confined to move only along the x direction, it will execute simple harmonic oscillation with frequency ω_p. Along the y direction, the ball will roll out of the saddle and will never restore equilibrium. This is depicted by Figure 2.5, which is a computer simulation of the Potential Energy Surface (PES) with the values of the potential colour-coded. Geometrical and RF parameters of the CHACE instrument are used for the simulation. The ion mass is taken as 28 amu for the calculation of the potentials.

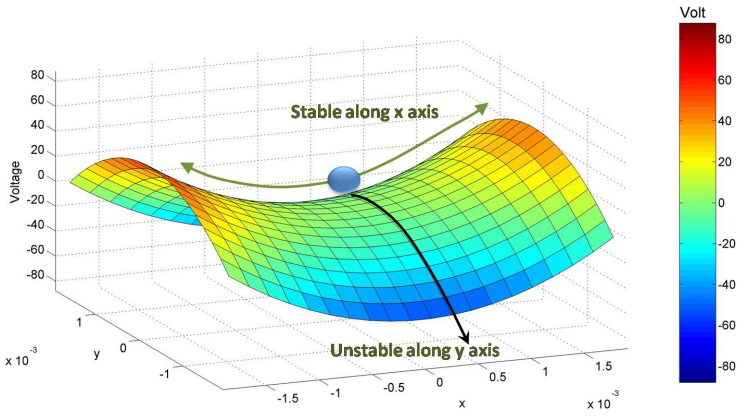

Figure 2.5: Computer simulated saddle-shaped Potential Energy Surface (PES) inside the QMA with a constant potential. A charged particle may be looked upon as a ball resting on the saddle. It is stable along the x direction with characteristic frequency ω_p, while unstable along the y direction.

Let us now assume that the potential Φ_0 is a periodic function of time and is of the following form.

$$\Phi_0 = U - V\ cos(\omega t) \tag{2.12}$$

Here, U and V respectively represent the DC potential and the amplitude of the time-varying component of the potential. Since the frequency ω is usually few MHz, it is customary to refer the time varying component as the RF component. Hereafter, the quantity V will be referred to as the amplitude of the RF component of the quadrupole potential.

The entire story of stability of an ion in a quadrupole field revolves around two

frequencies, viz. the characteristic frequency (ω_p) of the particle and the frequency (ω) of the RF (*Dawson*, 1976). How will these two frequencies interact is dictated by U and V. The stability of an ion in the quadrupole field demands that its trajectory does not fall prey to the interplay between the DC and RF so that either of them may resonate with the particle characteristic frequency and render it unstable.

If Φ_0 is periodic in time, the trajectories of the ion along both x and y directions are alternately deflected towards and away from zero. The ion may be stable, i.e. confined to the region enclosed by the quadrupole rods without being deflected away, under certain conditions. Qualitatively, the ion will remain stable (confined) if the periodicity of the RF is short enough and the ion is heavy enough that it can not respond sufficiently during the part of the cycle that makes the PES convex, which would have made it unstable. As an analogy, whenever the ball on the saddle is about to roll down the lower slopes of the saddle, the latter is inverted. If the frequency of this convex-to-concave conversion is suitable for confining an ion with a given mass-to-charge ratio within the radius of r_0 from the origin, it will be stable along both the x and y directions in the x-y plane.

In practice, it is easier to operate the QMA at a fixed RF frequency. Stability for ions of different mass is achieved by changing the depth of the PES. For confining heavier ions, more depth (or curvature) of the PES is required than the lighter ions. This calls for increasing the potentials U and V, which increases the curvature of the PES and facilitates stabilizing the heavier ions. For lighter ions, relatively less curvature of the PES (hence lesser values of the U and V) are necessary. Figure 2.6 shows computer simulation of the PES for RF phases of 0° (top panel) and 180° (bottom panel).

The lighter ions have higher mobilities (mobility is the velocity acquired per unit field strength, which is inversely proportional to the mass of the particle) than the heavier ions. Hence, the lighter ions respond more to the RF component while the heavier ions respond more to the direct component. In other words, the characteristic frequency (ω_p) of the heavier ions is small while that of the lighter ions is high. Hence, the heavier ions tend to resonate with the low frequency (i.e. respond more to the direct component with zero frequency) while the lighter ions resonate with higher frequencies (i.e. the RF). Mass filtering is accomplished by the simultaneous modulation of the RF and direct components along both the x and y directions.

Suppose, in a given half cycle, the RF component is larger than the direct component. Thus, the right and left quadrupole rods (refer Fig. 2.4) have negative potentials due to the RF component and the ion (positive) will be attracted towards them. The lighter ions have greater mobility and they are able to follow the RF. Hence, the lighter ions have unstable trajectories along the x direction. As the heavier ions have lesser mobilities, they do not respond to the RF sufficiently enough to get deflected. Thus, for this half cycle, the x direction is equivalent to a high pass mass filter. At the same time, in the y direction,

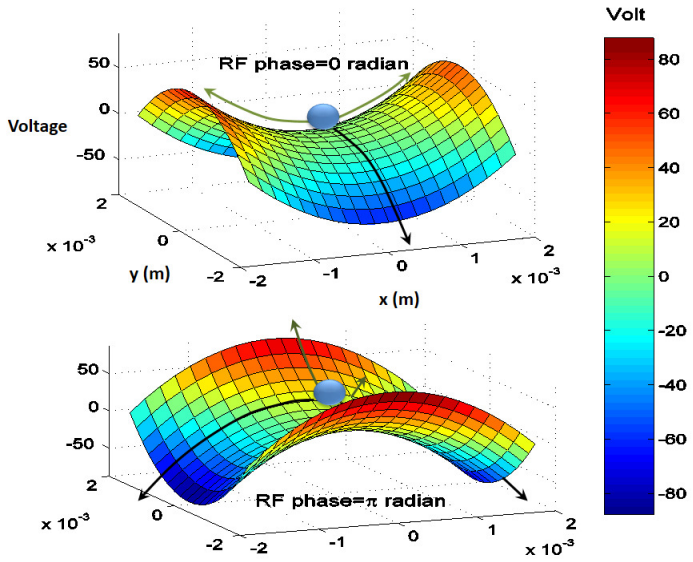

Figure 2.6: Computer simulated PES inside the QMA with the assumption of an RF component. Simulations depict the PES at the RF phases of 0° (top panel) and 180° (bottom panel). The simulation is carried out for a species with m/q=28 amu and using the CHACE geometrical and RF parameters. It shows that in one half cycle, the ion is stable along the x direction, while in the next half cycle it is stable in the y direction.

heavy ions are unstable because of the defocussing effect of the direct component (the direct component is at a lower potential and the heavier ions tend to be attracted) of the top and bottom rods. However, some lighter ions are stabilized in the y direction by the RF component provided certain conditions are met. The conditions are that the mass (and hence the mobility) of the lighter ions are such that their trajectories are 'self-correcting' and hence, never fall prey to the combination of the amplitude and the frequency of the RF component which could have rendered them unstable. This means that the lighter ions must correct their trajectories whenever the amplitude of oscillation in the y direction tends to increase. Hence, the RF component acts as a high pass mass filter while the direct component acts as a low pass mass filter. Thus, the y direction acts as a low pass mass filter. The two directions (x and y) collectively give rise to a mass filter with a certain pass band.

Substituting equation (2.12) in equations (2.9) and (2.10) , the equations of motion for a time-varying potential assume the following form.

$$\ddot{x} + \left(q/mr_0^2\right)\left(U - Vcos(\omega t)\right)x = 0 \tag{2.13}$$

and

$$\ddot{y} - \left(q/mr_0^2\right)\left(U - Vcos(\omega t)\right)y = 0 \tag{2.14}$$

Using the transformations given by equations 2.15, 2.16 and 2.17, the equations (2.13) and (2.14) are combined into a single equation, given by equation 2.18.

$$a_u = a_x = -a_y = \frac{4qU}{m\omega^2 r_0^2} \tag{2.15}$$

$$q_u = q_x = -q_y = \frac{2qV}{m\omega^2 r_0^2} \tag{2.16}$$

$$\xi = \frac{\omega\, t}{2} \tag{2.17}$$

and $u = x, y$.

Equations (2.13) and (2.14) are thus reduced to the form

$$\frac{d^2u}{d\xi^2} + \{a_u - 2q_u \cos(\xi - \xi_0)\}\, u = 0 \tag{2.18}$$

Here, ξ_0 accounts for the initial phase of the RF as seen by the ion when it was introduced to the quadrupole field.

Equation (2.18) is known as the Mathieu differential equation.

Solution of the Mathieu differential equation yields both stable and unstable trajectories. The unstable trajectories are those for which

$$\lim_{t\to\infty} u = \infty \tag{2.19}$$

During the motion of an ion in the x-y plane under the influence of the quadrupole field, if a negative potential gradient is applied along the positive z direction, the ion experiences a motion in the z direction as well. As a result, while responding to the transverse (x-y) quadrupole field, the ion also moves from the entrance of the QMA to the exit, where a detector with radius R_D is placed. If the trajectory of the ion is such that $\sqrt{x^2+y^2} > R_D$ at the exit of the QMA, it does not reach the detector and hence no current is produced. The stable trajectories are the ones for which $\sqrt{x^2+y^2} < R_D$. Figure 2.7 shows a computer simulation of the ion trajectories with purely axial initial velocity, obtained by numerically solving the Mathieu differential equation using Runge-Kutta method (*Scarborough*, 1966) under the influence of both the transverse quadrupole field and the axial electric field. The combination of DC and RF components of the quadrupole potential are such that an ion with m/q=1 amu has a stable trajectory while an ion with m/q=2 amu is rendered unstable.

The condition for stability of a solution depends on the parameters a_u and q_u. A detailed mathematical analysis on the stability conditions of the solution of the Mathieu's equation is given in *Dawson* (1976). In short, Mathieu's equation yields stable solution

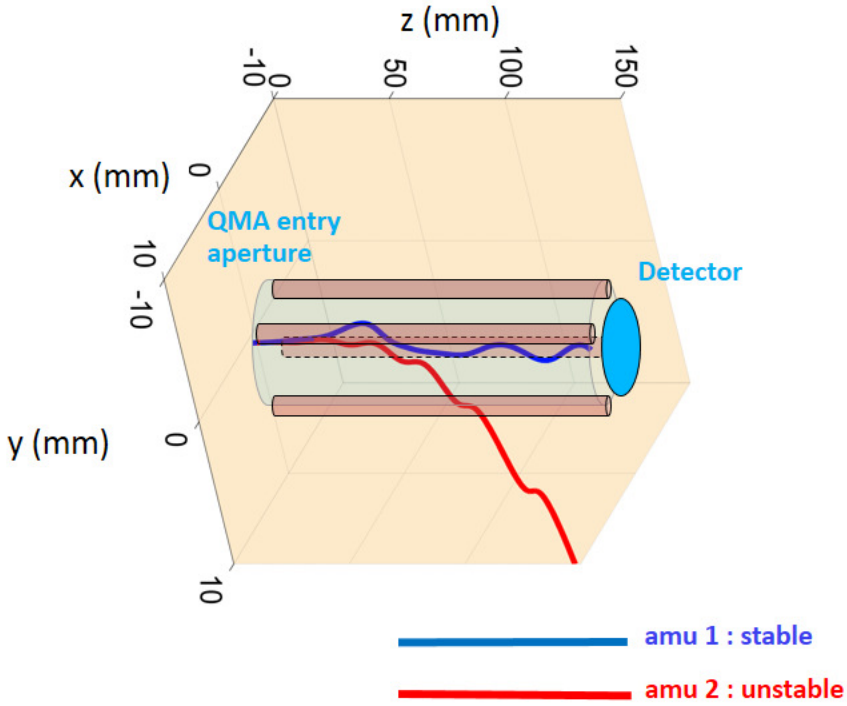

Figure 2.7: Computer simulated trajectories of two species with m/q=1 and 2 amu, computed by numerically solving the Mathieu equation. The ions are moving from the QMA entry aperture (left) towards the detector (right). The combination of the DC and RF potentials rendered amu 1 ions stable and the amu 2 unstable.

for certain combinations of (a_u, q_u) and hence (U, V). The set of values of (a_u, q_u) for which an ion of a given mass-to-charge ratio (m/q) is stable in the x-y plane in both x and y directions, constitute the Paul stability regions in the (a_u, q_u) plane. Equivalently, the combination of values of (U, V) for the stability of an ion constitute the Paul stability regions in the (U, V) plane. Figure 2.8 shows a simplified picture of the stability regions.

The top panel (a) of Fig. 2.8 shows the start and stop times of a mass scan. A mass scan is achieved by linearly varying the values of U and V from a minimum to a maximum depending on the mass range of interest. The quantity T_{scan} denotes the time taken by the QMA to complete the scanning of the entire mass range. The second panel (b) shows the (U, V) plane. Three triangular regions are shown for three masses, viz. m_1, m_2 and m_n. The area enclosed by each triangular region in the (U, V) plane contains the combinations of U and V for which the ions of the corresponding mass (to be more accurate, the mass-to-charge ratio) will have stable path along both the x and y directions. These triangular regions represent Paul stability regions. The panel also shows a straight line passing through the origin (U=V=0) that intersects the triangular regions near their respective vertices. It is along that line, called the operating line or bias curve, the quantities U and V are ramped simultaneously. The ramping of U and V is done in a way such that the ratio U/V remains constant. This process tunes the pass-band of the QMA mass filter from

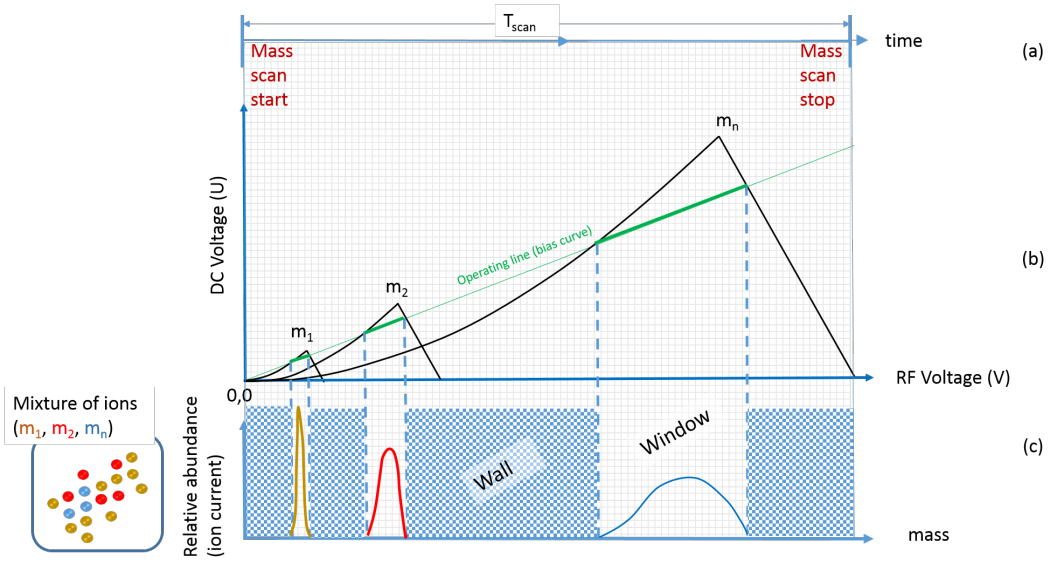

Figure 2.8: The top panel (a) shows the time axis; T_{scan} represents the time required to complete a mass scan. Panel (b) shows that mass scanning is achieved by ramping U and V simultaneously and proportionally. Ions with a given mass-to-charge ratio are stable and hence pass through the QMA when the bias curve intersects the triangular regions called the Paul stability regions. Panel (c) shows that how a mixture of ions pass through the mass filter and constitute output current proportional to their relative abundances at the detector.

lighter to the heavier ions. The segments of the operating line that pass through the Paul stability regions are shown with thicker lines.

The third panel (c) in Figure 2.8 shows the mass axis along the abscissa as mass since both U and V are proportional to the mass of the stable ions. The y axis shows the current generated at the detector by the incidence of the path-stable ions onto it. The current generated at the detector due to the ions with a given m/q is equivalent to their relative abundance in the medium. It is shown in the figure that during the ramping of U and V whenever the bias curve intersects the Paul stability regions (shown with thicker segments of the bias curve), it offers an opportunity to a group of ions with the correct m/q to be stable. If such ions are present in the medium, they travel to the detector through the QMA and constitute an output current. In the Figure 2.8, these regions are labeled as 'window'regions. The 'wall'regions are those where the bias curve does not intersect th Paul stability regions and no ion is stable in the x-y plane. Hence no current is formed at the detector by the ions. The third panel further shows that a mixture of three kinds of ions (with masses m_1, m_2 and m_n), thus mass-filtered, constitute peaks at the respective window slots; the peak amplitude is determined by their relative abundances. The shape of the peaks, especially the Full Width at Half the Maximum (FWHM), which is often denoted by Δm, depends on the width of the regions of the bias curve that intersect the Paul stability regions. The resolution of a peak is given by $R = m/\Delta m$. For a sharp peak (high resolution), the quantity Δm should be small. This is accomplished

by increasing the slope of the bias curve in the (U, V) plane. A trade-off is often made between the resolution and throughput (transmitivity of the ions through the QMA). For higher resolution, transmitivity is poor and vice versa. The ratio U/V=0.168 offers the maximum resolution of the mass filter (*Young*, 2002; *Dawson*, 1976).

2.2.2 The CHACE sensor probe and electronics

In practice, it is easier to machine quadrupole rods with circular cross sections rather than hyperbolic cross sections. In CHACE, circular rods are used for the QMA. The use of circular rods instead of hyperbolic rods introduce sixth order distortion in the quadrupole potential, which affect the sensitivity of the system at higher resolving powers (*Dawson*, 1976). This distortion is minimized by using circular rods with radius $1.148r_0$, which fairly approximate the electric field of a hyperbolic rod system. This geometry, along with a grounded circular housing of radius $3.54r_0$ keep the distortion negligible and hence there is practically no effect on the data acquired by CHACE. Figure 2.9 shows the cross section of a QMA with circular cross section quadrupole rods.

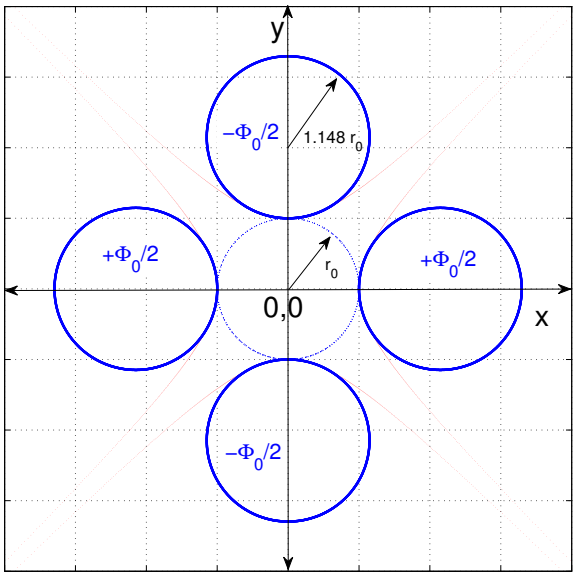

Figure 2.9: Quadrupole rods of circular geometry are easier to machine than the hyperbolic rods. The circular rods with radius 1.148 times r_0 (radius of the in-circle touching the quadrupole rods) fairly reproduce the quadrupole field as done by the ideal hyperbolic geometry rods.

Figure 2.10 shows the block diagram of the CHACE instrument. The sensor probe consists of an electron impact ionization source; two sensors, *viz.* a transmission-type QMA for mass filtering and a Bayard-Alpert (B/A) gauge to measure the total pressure; and a detector assembly comprising a Faraday Cup (FC) and a Channel Electron Multiplier (CEM). The CEM has a rectangular aperture of 9 mm $\times$ 4 mm dimension, consisting of a glass tube of curved geometry with the channel length of 25 mm, coated with a high

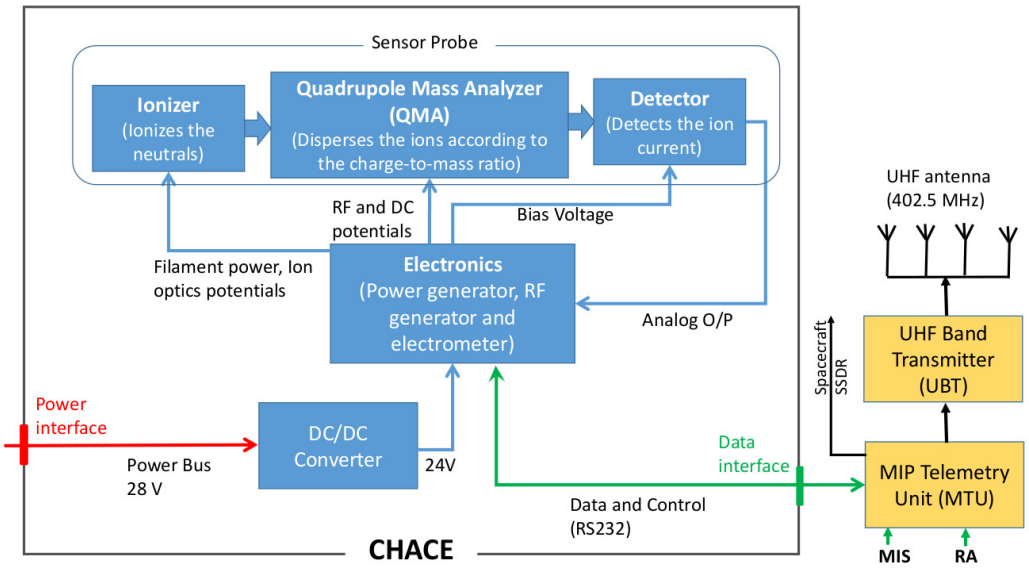

Figure 2.10: Block diagram of the CHACE instrument. The MTU is responsible for multiplexing the data from CHACE, Moon Imaging System (MIS) and the Radar Altimeter (RA). The data are transmitted through the UHF transmitter and antennae to Chandrayaan-1 orbiter.

resistance film. The CEM is placed off-axis (Benninghoven configuration) in order to eliminate any possibility of generation of spurious output current by the direct incidence of photons or high energy particles (*Dawson*, 1976). A schematic of the sensor probe of CHACE is shown in Figure 2.11.

The ionizer consists of a cylindrical ionization source grid region (see label 2 in Fig. 2.11). The neutrals ionized within the ionization source grid region are focused by the focus grids to enter the QMA for subsequent mass filtering.

In CHACE, the potentials U and V are ramped simultaneously up to 47 V and 278 V, respectively, at the RF frequency of 2.304 MHz to scan the mass range of 1 to 100 amu with 1 amu mass resolution. The Digital-to-Analog Converter (DAC) step is equivalent to 0.11 amu, and hence each mass bin of 1 amu width is divided into 9 equispaced samples. Thus, a mass spectrum contains 900 equispaced data samples covering the range of 1 to 100 amu. Figure 2.12 is an example of a laboratory mass spectrum of the residual gases in a vacuum chamber evacuated with a turbo molecular pump.

The x-axis of the mass spectrum is the mass-to-charge ratio. However, assuming single ionization of the neutrals the x-axis may be treated as the mass axis. It is observed that the residual gas spectrum is dominated by the signature of water vapour (H_2O), i.e. amu 18, and its dissociated products amu 1 (atomic H) and amu 17 (OH), along with amu 28 (N_2 plus CO), amu 32 (O_2) and amu 44 (CO_2).

The ions formed outside the ionization source grid region in the ionizer are collected by the B/A gauge collector giving rise to a line current which is calibrated to the total

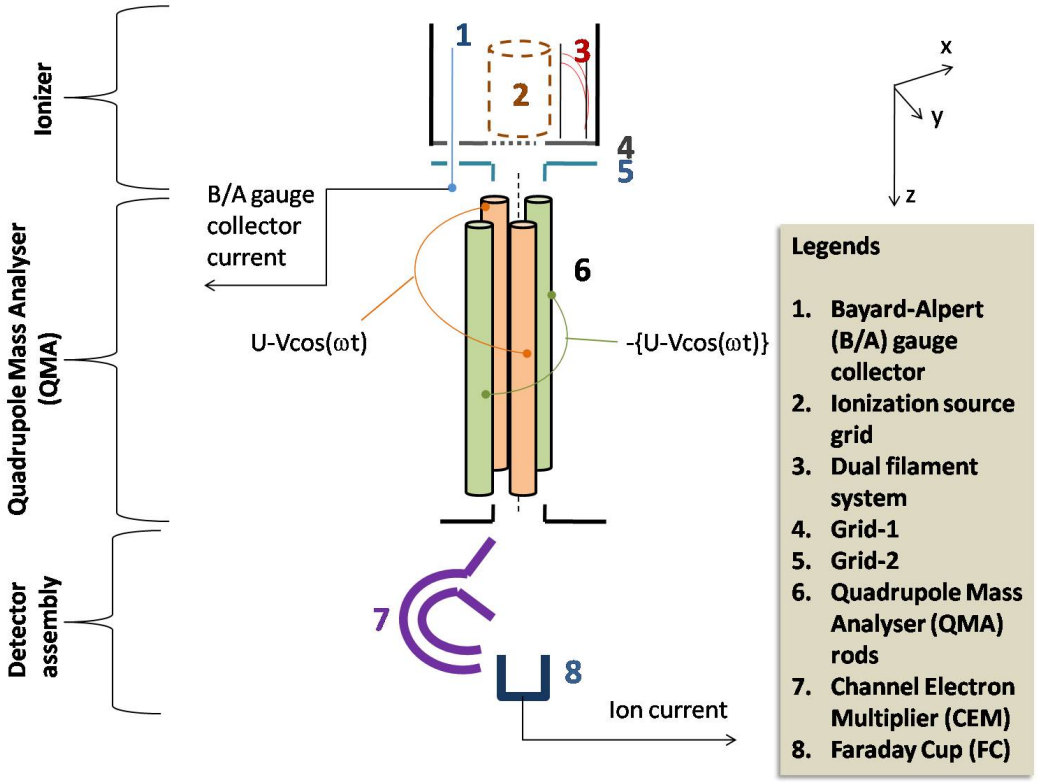

Figure 2.11: Schematic diagram of the sensor probe of the CHACE instrument.

pressure in a N_2 dominated medium at 300 K temperature.

The CHACE electronics caters to four important functions. First, it supplies electrical power to the different subsystems in the sensor probe that include the electrodes, filaments, ion optics, quadrupole potentials and the detector assembly. Secondly, it generates RF of 2.304 MHz frequency for the QMA. Thirdly, it receives the ion current and does the necessary signal conditioning, which include current to voltage conversion and digitization. Fourth, it sends the digitized data to the MIP Telemetry Unit (MTU) through the RS232 interface. The MTU contains the firmware to control and command the CHACE electronics. Upon switch ON, the initialization code containing the instrument parameters stored in the MTU is pushed to the CHACE electronics. Once initialized, the filament is turned on gradually and the QMA operation starts. The science and the house keeping (HK) data of the CHACE instrument are sent to the MTU, which, in turn, interface to the UHF transmitter of the MIP for subsequent transmission to the Chandrayaan-1 spacecraft. MTU also contains a hard-line interface to write the data directly into the Solid State Data Recorder (SSDR) in the spacecraft before the MIP-separation.

Apart from the RS232 data interface, CHACE has power interface with the MIP battery. It receives 28 V through the MIP power bus and uses the regulated 24 V output.

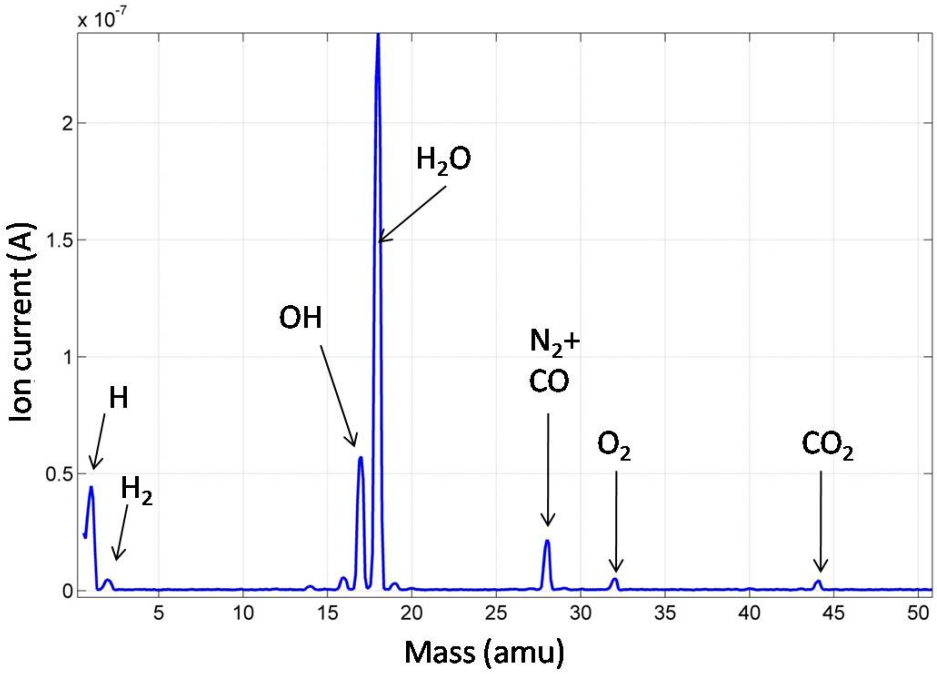

Figure 2.12: A laboratory spectrum acquired by the CHACE instrument. The signatures of the major residual gases in the chamber are seen in the spectrum.

2.2.3 Development philosophy

During the development of the CHACE experiment, there was no reliable in-situ measurement of the sunlit side of the lunar exosphere. Based on the measurements of the lunar atmospheric pressure at the surface by the Cold Cathode gauges in Apollo 12, 14 and 15 missions (*Stern*, 1999), total pressure of $\sim 10^{-10}$ Torr was expected in the sunlit lunar exosphere.

The challenge was to conduct in-situ measurement of the tenuous lunar exosphere and configure the instrument suitably to cover the expected range of pressures with adequate dynamic range, without resorting to higher integration time as that would have limited the spatial resolution of the measurements. In general, the major considerations for the development of the CHACE instrument included the following:

1. Sensitivity to measure the tenuous exosphere of the Moon.

2. Collection of sufficient number of mass spectra since the CHACE was a one-time experiment.

3. Cleanliness to minimize the effect of outgassing from the instrument.

4. Structural integrity of the payload for avoiding field imperfections and accurate measurement of the ion current.

The sensitivity of CHACE was ensured by the careful choice of the operating parameters, through numerous characterization experiments conducted in the ultra high vacuum condition (pressure $\sim 10^{-8}$ to 10^{-9} Torr). The cleanliness of the instrument was ensured by the careful choice of materials of low outgassing property, ultrasonic cleaning and baking of the sensor probe prior to the assembly in the clean room and vacuum-isolation of the sensor probe while integrating with the MIP.

Ruggedization of the payload was of paramount importance in order to eliminate any possibility of permanent deformation of the ion optics and/or the quadrupole rods due to the mechanical distrubances during the launch phase. The structural dynamics of the sensor was studied using finite element model and the ruggedization scheme was worked out. The overall payload design was conducted based on the prescribed environmental test levels for the lunar mission using PSLV core alone configuration. The CHACE sensor was suitably ruggedized using ceramic material in order to protect its mechanical precision. The electronic components were protected from mechanical disturbances by using potting compounds. All materials that were used for the process of ruggesdization underwent necessary tests for outgassing properties and were accepted as per quality protocols for flight.

2.2.4 Operating parameters

The major parameters that determine the performance of the CHACE instrument include the focus voltage, electron energy, mass scan rate and the CEM bias voltage.

1. **Focus voltage** (FV)
   Focus voltage is the voltage applied at the electrode marked with label 5 with respect to the one marked with label 4 in the Figure 2.11. A negative FV attracts the positive ions from the source grid (label 2) to the entrance of the QMA. This potential focuses the mixture of ions with different mass-to-charge ratio to the entrance aperture of the QMA. Figure 2.13 shows the result of the characterization of the focus voltage with respect to the ion current corresponding to amu 28. Based on the results, the optimized focus voltage of -30 V was used for CHACE.

2. **Electron energy**
   The term electron energy in the present context refers to the energy imparted to the thermionic electrons emitted from the dual filament system by the application of a potential. The Coulomb interaction between the energetic electrons and the valence electrons of the neutrals causes ionization of the neutrals in the ionizer region. Most of the atomic and molecular species have their electron impact ionization cross section maximum in the range of $\sim$ 60-100 eV (*Lotz*, 1968; *Montanari and Miraglia*, 2014). CHACE used 70 eV electron energy to ionize the neutrals.

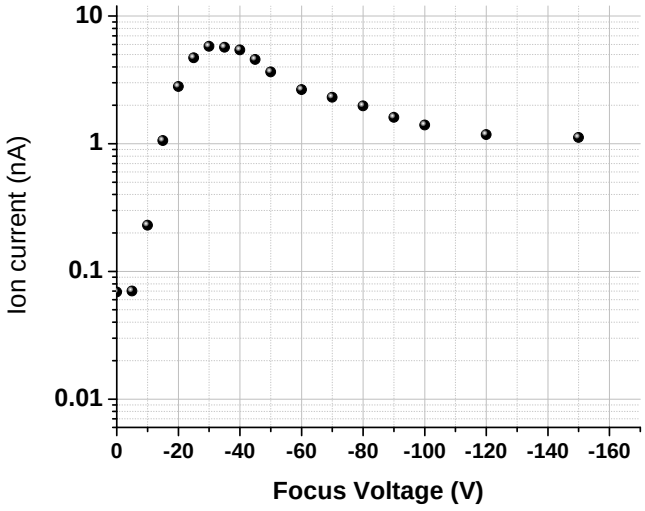

Figure 2.13: Variation of the ion current for amu 28 (N_2) for different focus voltages.

3. **Mass scan rate**
   Mass scan rate refers to the rate at which a mass spectrum (ranging from amu 1 to 100) is scanned. Faster the scan, higher is the noise level and the spectrum acquisition time is less. For slower scans, on the other hand, the noise level is lower but the time required to acquire a spectrum is more. The spectrum acquisition time of CHACE was chosen based on the criteria: 1) the noise level should be low enough to sample the tenuous lunar exosphere, and 2) The spatial resolution, when translated to the ground trace, should be better than 10 km, in order to study the dependence of the exosphere on the spatial variabilities of the lunar surface. Based on these considerations, a mass can rate of $\sim$4 s was chosen. Taking the motion of the MIP in consideration, this translated to a ground trace of $\sim$6.5 km on the lunar surface.

4. **CEM bias voltage**
   The input of the CEM is biased with a negative voltage in the range of 10^3 Volt. The positive ions that reach the input of the CEM detector create a cascade of electrons. These electrons exit the CEM at a potential of $\sim$ -150 V DC with respect to the ground and are attracted to the Faraday cup held at virtual ground. The current produced at the Faraday cup is a measure of the abundance of the corresponding neutrals in the medium. An increase in the CEM bias voltage causes enhancement in the electron multiplication at the CEM, resulting into a higher gain, thus enhancing the value of the current at the Faraday cup output. As a result, the sensitivity of detection of a given species is increased.

   Initially, the SNR increases because of the increase in the CEM gain with increase in the CEM bias voltage; then attains a plateau; and subsequently decreases with

further increase in the bias voltage (refer the inset of Fig.2.14 for the variation of SNR of amu 28 with CEM bias voltage at a total pressure of 4×10^{-9} Torr). That is because of the saturation of the CEM gain and increase in the shot noise in the CEM detector with increase in the bias voltage. Hence, there exists an optimum value of the CEM bias voltage, for which the SNR is maximum. The optimum bias voltage of the CEM depends on total pressure. For higher pressure, the optimal value of the CEM bias voltage is less. This is because of the ionization of neutrals within the CEM that causes saturation of the CEM gain even at comparatively lower bias voltages. Experiments were conducted at different levels of total pressure and the optimum values of CEM bias voltage were obtained. Figure 2.14 shows the variation of the optimum CEM voltage with total pressure. A detailed description of the figure is provided in the caption. The CEM of CHACE was biased at 1800 V for the total pressure of 10^{-10} Torr expected at the lunar day-side.

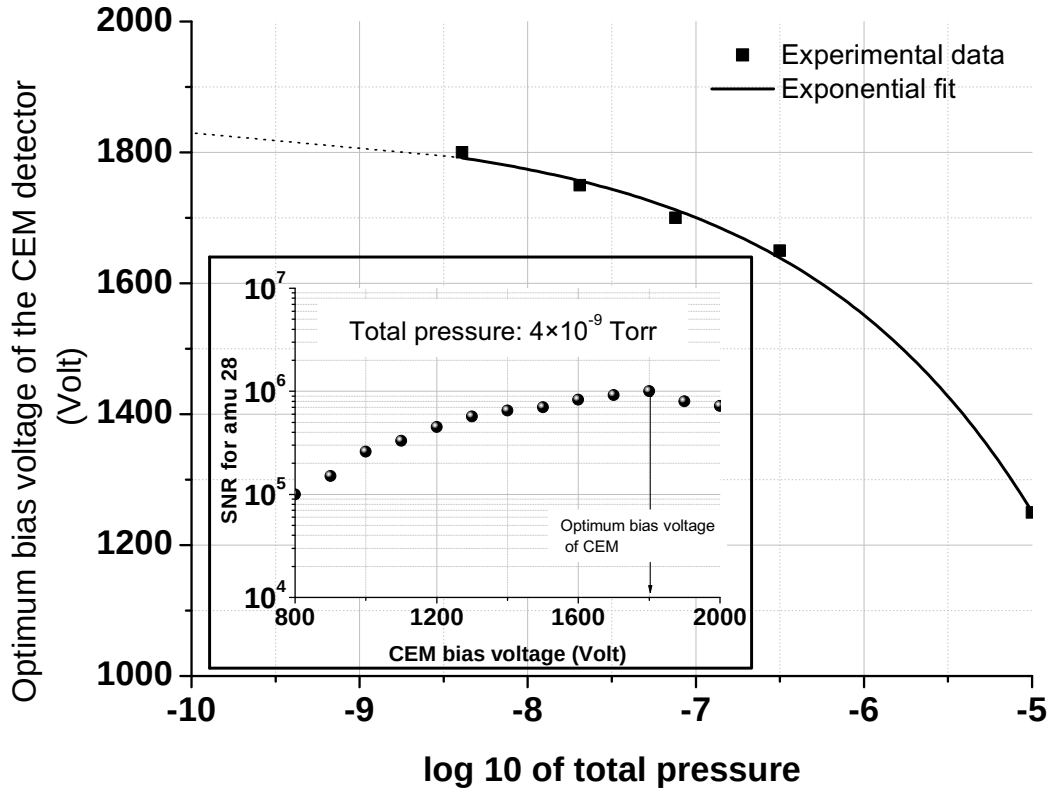

Figure 2.14: Variation of the optimum bias voltage of the CEM detector with total pressure. The filled squares are the experimentally obtained points and the continuous solid line is the exponential fit, which is extrapolated (dotted extension) to 10^{-10} Torr of total pressure, as expected in the sunlit side of the Moon. At a given total pressure, the optimum CEM bias voltage is obtained by studying the variation of the SNR of amu 28 peak with CEM bias voltage, as shown in the inset for a pressure of 4×10^{-9} Torr. Based on this experiment, the CEM bias voltage of CHACE was set at 1800 V.

2.3 Ground calibration and testing

The CHACE instrument was ground calibrated from high vacuum of 10^{-6} Torr to ultra high vacuum of 10^{-9} Torr. The calibration included determination of the relative transmission and detection efficiencies of ions with different mass-to-charge ratios. It also involved mass calibration with residual gases and insertion of pure and mixed gases in the chamber. The B/A gauge is calibrated for the total pressure.

2.3.1 Relative detection efficiencies

Detection efficiency of an ion by a transmission-type quadrupole mass spectrometer depends on the transmission properties through the quadrupole mass filter and the sensitivity of the detector. The relative detection efficiencies of the lighter species are greater than the heavier ones. This is mostly because of the Quadrupole Mass Discrimination (QMD) effect and the mass-dependent sensitivity of the CEM detector (*Dawson*, 1976).

The analytical theory of an ideal QMA does not take into account the effects of the fringing electric fields on the motion of the ions at the terminations of the quadrupole rods. In practice, the fringing fields affect the entry of the ions from the ionizer to the QMA (*Dawson*, 1976). They tend to trap the ions and delay the process of its transmission through the mass filter. Because of their lesser mobility, the heavier ions are more susceptible to get delayed in the fringing fields than the lighter ones. As a result, the heavier species have lesser transmission efficiencies than the lighter ones. This results into the overestimation of the relative abundance of the lighter species with respect to the heavier ones. This is known as the QMD effect (*Dawson*, 1976). The relative transmission efficiencies of different ions is calibrated for different masses in order to nullify this mass discrimination effect during analysis. The QMD factor is the reciprocal of the relative transmission efficiencies of the ions, which is a multiplicative correction factor to compensate for the QMD effect.

The variation of the relative transmission efficiency with ion mass, represented by the continuous curve in figure 2.15, is obtained by comparing the experimental and theoretical values of the fractionation ratios of water vapour (amu 1 , amu 16, amu 17, amu 18) and the compound Per Fluoro Tri Butyl Amine (PFTBA) (which yields mass peaks at amu 31, 69 and 100 in the range of 1-100 amu) (*Chapman*, 1995) for 70 eV electron impact energy. Also, the experimental and theoretical values of the single-to-double ionization ratios of Ar-40 and N (amu 14) are used for obtaining the relative transmission efficiency profile.

Figure 2.16 shows the gain of the CEM detector in CHACE as a function of the ion mass. The bias voltage was 1800 V. The Electron Multiplier Gain (EMG) profile is characterized to study the variation of the gain of the CEM detector with the ion mass. The EMG profile is obtained by comparing the mass spectra acquired with Faraday cup and the

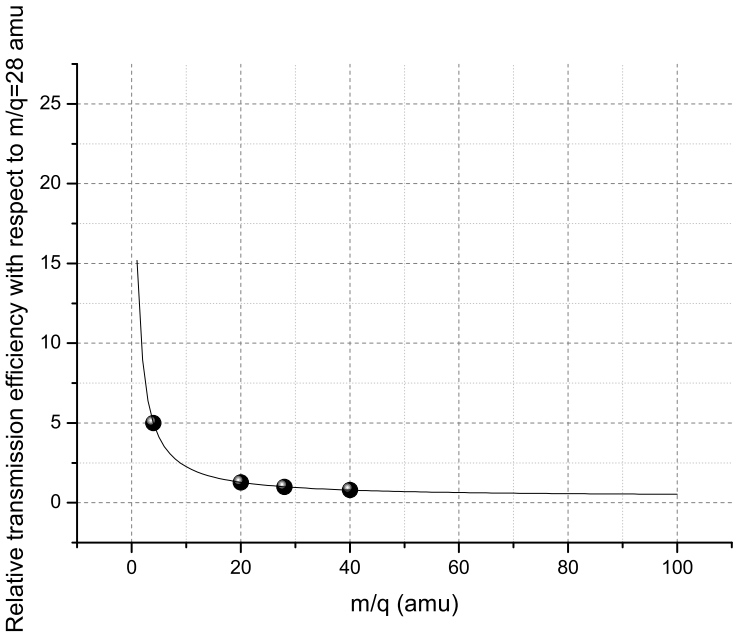

Figure 2.15: The continuous line represents the variation of the relative transmission efficiency (with respect to N_2 (amu 28)) with ion mass. The relative transmission efficiency curve is obtained by comparing the experimental and theoretical values of the fractionation ratios of water vapour (amu 1 , amu 16, amu 17, amu 18) and the compound Per Fluoro Tri Butyl Amine (PFTBA) (which yields mass peaks at amu 31, 69 and 100 in the range of 1-100 amu) for 70 eV electron impact energy. In addition to the fractionation ratios of the compounds, the experimental and theoretical values of the single-to-double ionization ratios of atomic species like ^{40}Ar (i.e. ratio of the parent peak at amu 40 to the harmonic peak at amu 20) and N (i.e. ratio of the parent peak at amu 14 to the harmonic peak at amu 7) at 70 eV electron energy are also used for obtaining the relative transmission efficiency profile. The solid circles, drawn on the relative transmission efficiency curve, represent the relative transmission efficiencies of ^{4}He, ^{20}Ne, ^{40}Ar with respect to N_2 due to the Quadrupole Mass Discrimination (QMD) effect.

CEM detector. The EMG profile is a divisive correction factor to account for the lesser sensitivity of the CEM detector to the heavier ions.

Both the relative transmission efficiency and the EMG are functions of ion mass and hence, the raw spectra needs to be corrected by incorporating the QMD and EMG effects, for the accurate interpretation of the relative abundances of gases. Figure 2.17 shows the relative sensitivity profile of the instrument (normalized with respect to amu 28) for the combined effects of mass dependent performances of the QMA and CEM.

2.3.2 Mass calibration

It is important to ensure that the gas atoms and molecules, ionized by the ionizer section of CHACE, register peaks at the correct value of the mass-to-charge ratio bin. This is ensured by mass calibration of CHACE, which is conducted with reference to the following:

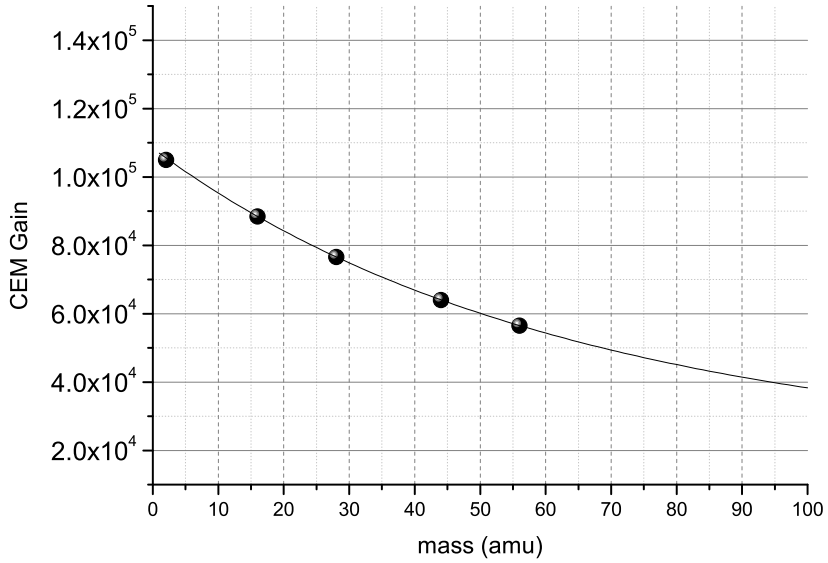

Figure 2.16: Variation of the Electron Multiplier Gain (EMG) of CHACE with the ion mass, at 1800 V bias. The EMG is calculated by comparing the signal strengths of the residual atmospheric gases viz. amu 1 (H atom), amu 16 (O atom), amu 28 (N_2 molecule), amu 44 (CO_2 molecule) and amu 56 (which is due to the oil used in the turbomolecular pump) in electron multiplier and Faraday cup modes. The criteria to choose these points are: 1) the signal strength should be high enough to detect it even in the Farady cup mode (less sensitive mode), 2) the signal strength should be stable with time (so that it doesn't vary during the span of the experiment) and 3) signals should cover a wide mass range.

- The residual gases in the vacuum chamber.
- Laboratory grade gases: ^{4}He, ^{40}Ar, N_2 and CO_2.

The mass calibration is conducted in the Ultra High Vacuum facility of SPL, VSSC. The sensor probe is inserted in the vacuum chamber, which is evacuated by a turbo molecular pump. The ultimate vacuum reachable in the system is $\sim 10^{-9}$ Torr.

The first step of mass calibration is to ensure the proper placement of the residual gas peaks. Figure 2.12 shows the mass spectrum acquired by CHACE, which depicts the signature of the residual gases in the vacuum chamber. Mass calibration is conducted with respect to the following peaks, as listed in Table 2.2.

CHACE, having 1 amu mass resolution, can not distinguish between N_2 and CO; both yield peaks at 28 amu.

The next step in the process of mass calibration of CHACE is to ensure the proper placement of the peaks of the known gases inserted into the chamber. Laboratory grade (99.999 $\%$ purity) gases are inserted into the chamber and the signatures are studied. The electron energy used in the study is 70 eV. ^{4}He, ^{40}Ar, N_2 and CO_2 gases are used for this

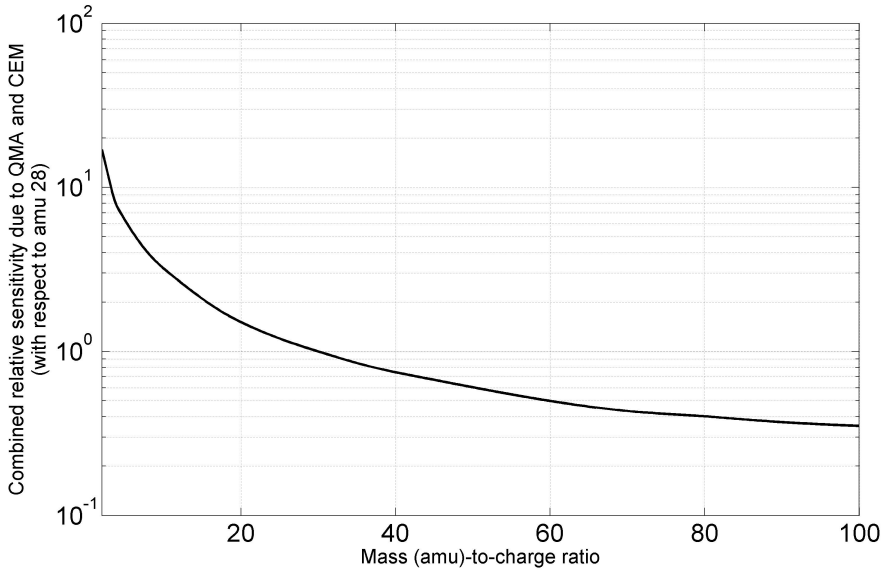

Figure 2.17: Combined relative sensitivity of the instrument due to the mass dependent performances of the QMA and the CEM. The lighter species have greater mobility and are less affected by the fringing fields at the terminations of the QMA, and hence have greater transmission efficiency. Also, the CEM gain is greater for the lighter species than the heavier ones. The overall effect is that the instrument is more sensitive to the lighter species than the heavier ones. This effect is corrected during the data analysis.

study. Figures 2.18, 2.19 , 2.20 and 2.21 show the signatures of ^{4}He, ^{40}Ar, N_2 and CO_2 respectively, as acquired by CHACE during mass calibration in the laboratory.

The mass calibration ensured not only the proper placement of the mass peaks on the mass axis, but also demonstrated the detectability of the lighter species like Hydrogen and Helium and stability of the measurement. As the quadrupole potentials (U and V) are proportional to the mass of the ion whose path is stable in the QMA, higher percentage stability of the quadrupole potentials is required for the stable measurement of the lighter species (*Dawson*, 1976).

2.3.3 Pressure calibration

Pressure calibration addresses to the calibration of the B/A gauge which measures the total pressure, which, in turn, is used to derive the partial pressures of the individual species. The total pressure measured by the B/A gauge is calibrated in an N_2 dominated environment using an external master gauge. For any other gas than N_2, the relative sensitivity factor with respect to Nitrogen is used, as shown in the second column of Table 2.3. Figure 2.22 shows the calibration of the B/A gauge of CHACE in an N_2 dominated environment.

Table 2.2: *Mass calibration with residual gases in the vacuum chamber*

Species	*Nominal mass-to-charge ratio (amu)*
Hydrogen atom	1
Hydrogen molecule	2
Hydroxyl radical	17
Water	18
Nitrogen molecule and Carbon monoxide	28
Oxygen molecule	32
Carbon dioxide	44

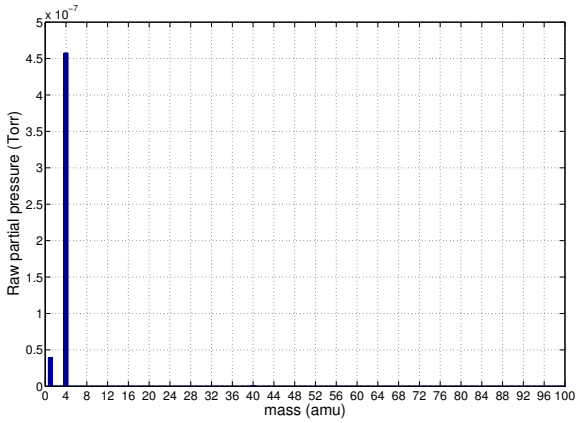

Figure 2.18: Signature of ^{4}He acquired by CHACE during laboratory calibration. While the parent peak is at amu 4, there is a harmonic peak due to double ionization of ^{4}He at amu 2, with a relative abundance of 0.08 with respect to the parent peak.

2.3.4 Sensitivity test

CHACE was subjected to a sensitivity test in order to study its response to He-4 and ^{40}Ar. Laboratory grade gases were used for the test. Before the sensitivity tests were conducted, the vacuum system and the CHACE sensor were thoroughly baked in vacuum for a period of two weeks. This was done in order to minimize the impurity level of gases due to the residual gases. The gas insertion and pump-out rates were adjusted in a way such that the rate of change of the abundance of the gas in the chamber was reasonably slow. Throughout the experiment, the inserted gas was dominant in the chamber, which was ensured from the spectra. The total pressure was measured with an external pressure gauge. The detector current was studied for different values of the total pressure and the sensitivities were derived from the slopes of the curves.

Table 2.3 presents the relative ionization sensitivities (with respect to N_2) of the gases addressed in the thesis, and their overall sensitivities.

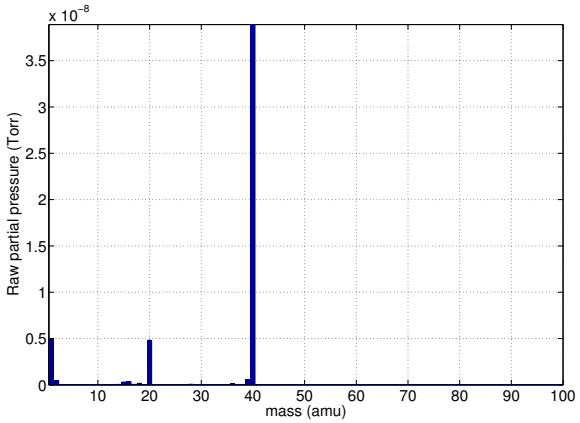

Figure 2.19: Signature of ^{40}Ar acquired by CHACE during laboratory calibration. The double ionized Argon (Ar^{++}) produces a peak at m/q = 20 amu.

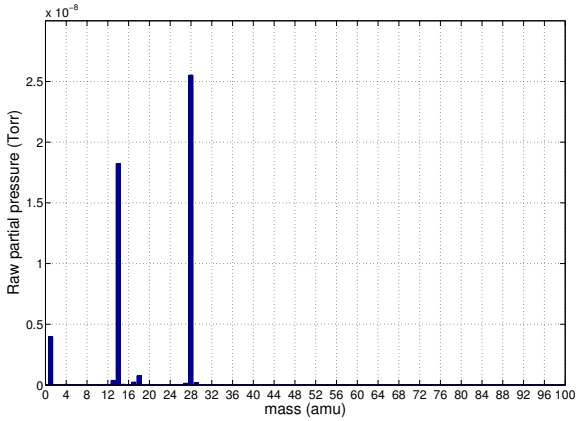

Figure 2.20: Signature of N_2 (amu 28) acquired by CHACE during laboratory calibration. The dissociated atomic N produces a peak at m/q = 14 amu.

It may be noted that the sensitivity tests were conducted in order to test the performance of the instrument for different gases. The sensitivity values were not used in deriving the absolute number densities of the gases reported in this thesis. Since CHACE was equipped with a calibrated Bayard-Alpert gauge, the absolute abundances were obtained by normalizing the sum over the peaks in a given mass spectrum with the total pressure and applying necessary calibration factors, as described in section 2.4. However, the number densities obtained from the absolute calibration (sensitivity test) match with the number densities obtained from the normalized partial pressures using Bayard-Alpert gauge measurements.

2.3.5 Test and Evaluation

CHACE has undergone all the tests as per the Chandrayaan-1 Environmental Test Level Specifications (ETLS) (*ISRO internal report: ISRO-VSSC-MIP-TR-001/2007*, 2007; *Test report on CHACE-FM: ISRO internal report*, 2008; *CHACE Package Assurance Re-*

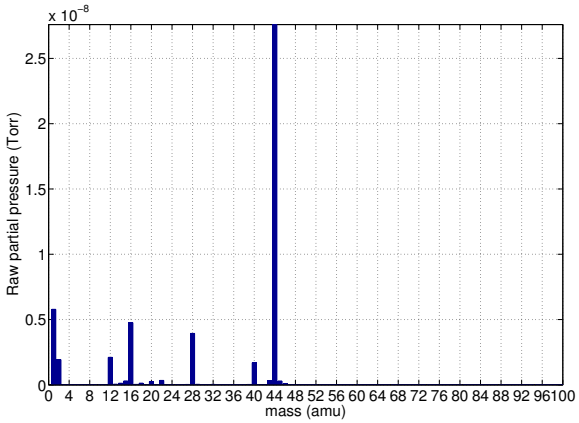

Figure 2.21: Signature of CO_2 (amu 44) acquired by CHACE during laboratory calibration. The dissociation products are CO and O and C producing peaks at m/q = 28, 16 and 12 amu, respectively.

Table 2.3: *Relative ionization sensitivity factor (with respect to N_2) (Summers, 1969; Holanda, 1972) and overall sensitivities for the noble gases covered in this thesis*

Species	*Relative ionization sensitivity with respect to N_2*	*Overall sensitivity (A/Torr)*
He	0.13	4.5
Ar	1.11	32.5
Ne	0.28	8.2
H_2	0.33	9.6

The overall sensitivities of Ne and H_2 are estimated from the experimentally obtained overall sensitivity of Ar, using the relative ionization sensitivity data.

port: ISRO internal report, 2008). The Flight Acceptance Tests (FAT) included pre-environmental tests at Standard Room Conditions (SRC); followed by the environmental tests which included thermovacuum test, sine and random vibration tests, (Electro Magnetic Interference/ Electro Magnetic Compatibility) EMI/EMC tests. The environmental tests were followed by the post-environmental SRC tests to confirm the functional normalcy of CHACE.

It was found that the performance of CHACE in the post-environmental SRC tests was within the specification limits and conformed to the pre-enviromental SRC test results. Figure 2.23 shows a comparison between two mass spectra obtained with CHACE flight model, acquired before and after the environmental tests.

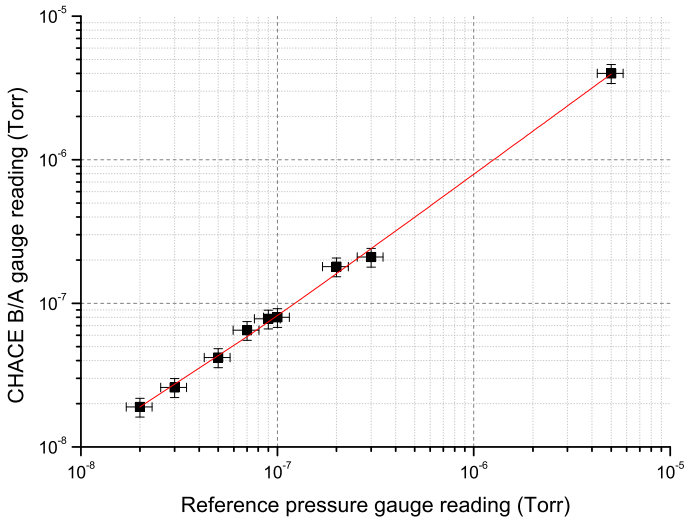

Figure 2.22: Total pressure calibration curve of the Bayard-Alpert gauge of CHACE. The linearity of the response of the gauge is established. The deviation between the readings of the Bayard-Alpert gauge of CHACE and the reference pressure gauge is due to the different locations of their mounting in the vacuum chamber with respect to the turbomolecular pump.

2.4 Mission operation of CHACE and data analysis

Five orbits before the release of MIP, on 14 November 2008, the MIP was switched ON for a rehearsal for a duration of ten minutes in order to check the normalcy of the payloads and the avionic subsystems. The performance of the payloads and the electronic systems were found to be normal. The MIP was released from the Chandrayaan-1 spacecraft on 14 November 2008 at 14:36:54.24 UTC at $\sim$ 13 °S latitude, $\sim$ 14°E longitude and $\sim$ 98 km altitude. The MIP deboost motor was fired to de-orbit it by imparting a delta-V of $\sim$ -62.67 m s^{-1}. MIP impacted the Moon at $\sim$ 89 °S latitude after a descend of $\sim$ 24 minutes through the lunar exosphere. The avionic systems and the payloads of the MIP were switched ON 20 minutes before the separation. Thus, MIP acquired $\sim$ 44 minutes of data (20 mins before separation and $\sim$ 24 minutes after separation, till impact) of the Moon.

MIP flew over the Malapert mountain (latitude $86°$S, longitude $0°$) at 8 km altitude and impacted near the Shackleton crater at the lunar south pole, covering a total ground range of $\sim$2340 km. The impact velocity of MIP was $\sim$ 1.7 km s^{-1}. Figure 2.24 (a) shows the geometry of orbit of Moon (black circle) around Earth in Geocentric Solar Ecliptic (GSE) coordinates for November 2008. GSE has its origin on Earth centre with x-axis towards Sun, z-axis along ecliptic North Pole and y-axis completes the right- handed coordinate system. Position of the Earth is indicated in black filled dot. The average position of Moon on 14 November 2008 is indicated using blue open circle, with respect

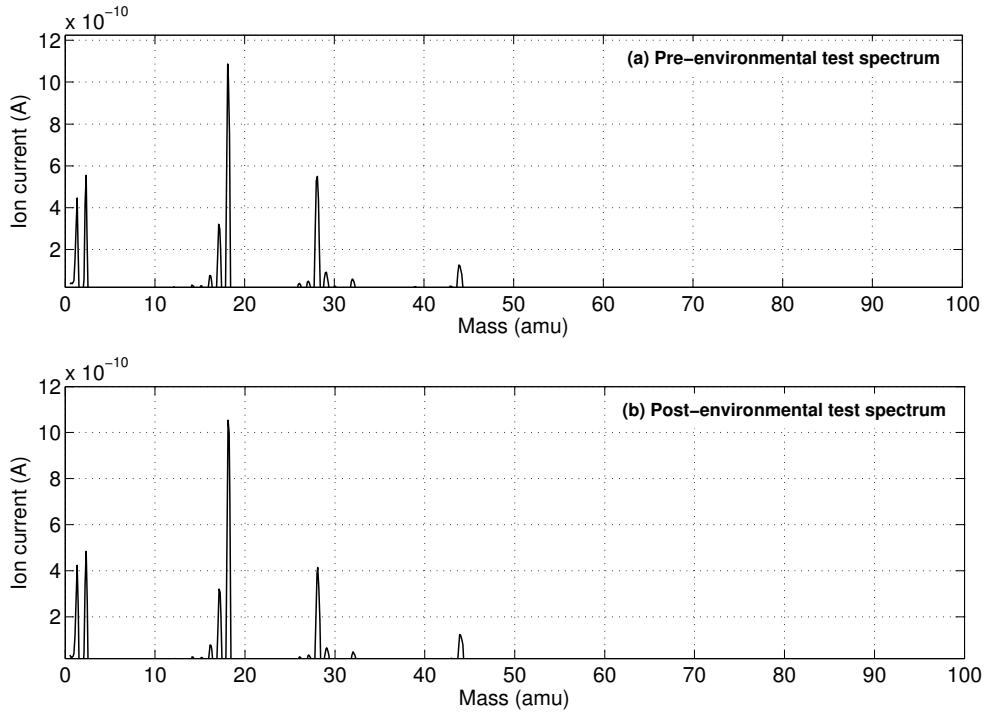

Figure 2.23: (a) A mass spectrum acquired with CHACE before the environmental test, at a total pressure of $\sim 5 \times 10^{-7}$ Torr. (b) A mass spectrum acquired after the completion of the environmental tests were completed, under similar total pressure. It is observed that the quality of the mass spectrum (assessed with respect to the mass resolution, peak shape, throughput and mass shift) is retained even after the environmental tests.

to the estimated positions of bow shock and geomagnetic tail. Figure 2.24 (b) shows the ground track of Moon Impact Probe (MIP) on Moon (red curve) in the y-z plane of Mean Earth (ME) coordinate system. The ME coordinate system has its origin on Moon centre with x-axis towards Earth, z-axis along the rotational pole of Moon and y-axis completes the right-handed coordinate system. This projection represents the geometry as viewed from Earth, such that the co-ordinate (0,0) represents the center of the near-side of Moon.

During the MIP mission, CHACE was switched ON at 14:16 UTC along with the other payloads, twenty minutes prior to the MIP release. The instrument took $\sim$ 20 minutes for the stability of its emission current from the hot cathode filament. During the MIP mission, CHACE was operated for a duration of $\sim$ 44 minutes, out of which for 20 minutes the MIP was attached with the Chandrayaan-1 orbiter. Each mass spectrum was acquired in $\sim$ 4.1 s, which translates to an average ground range of $\sim$6.5 km. During the MIP mission, CHACE acquired 650 mass spectra.

The post flight analysis of the HK parameters confirmed that CHACE was healthy during its operation. All the major parameters, viz. filament voltage, filament resistance, emission current, temperature, etc. were within the specification limits (*ISRO internal report: ISRO-VSSC-MIP-PFA-001/2008*, 2008).

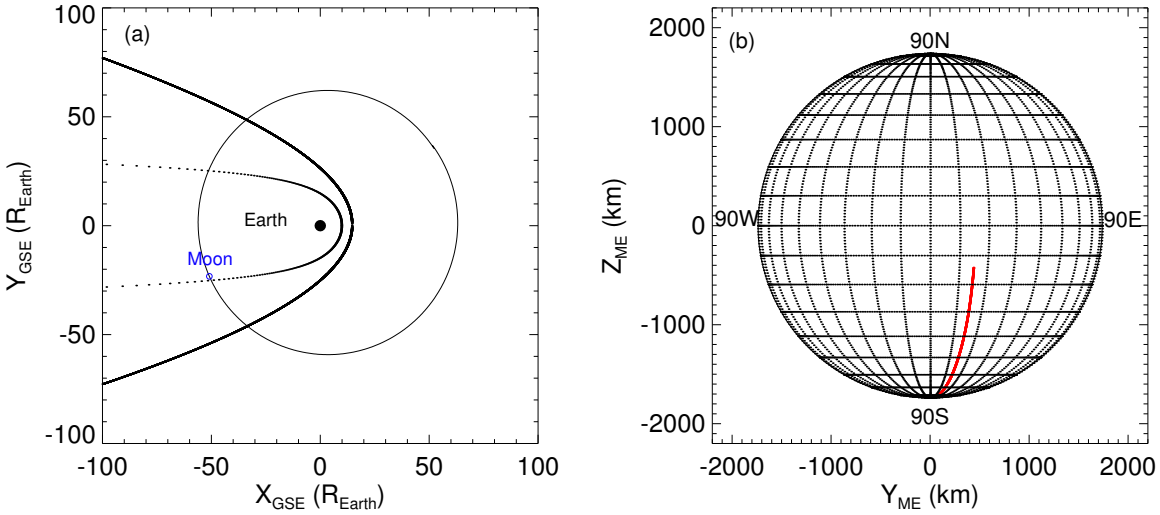

Figure 2.24: (a) Location of the Moon with respect to the Earth during the MIP release. The bow shock and the geomagnetic tail are shown for nominal solar conditions. (b) Ground trace of the MIP (red curve) after release from the Chandrayaan-1 orbiter.

The science data of CHACE comprise 650 mass spectra containing raw partial pressure (relative abundances of different species) data in the mass range of 1 to 100 amu; and the total pressure data for each spectrum from the B/A gauge. Out of these 650 mass spectra, the first 310 spectra were acquired when the emission circuit of CHACE was undergoing stabilization, while the rest 340 spectra were acquired with the emission circuit stabilized. For calculating the absolute abundances of species, the last 340 spectra were used, while all the 650 spectra were useful for ratiometric measurements (relative abundances).

First, the total pressure is corrected for the dominant gas with reference to the mass spectrum (the N_2-equivalent total pressure is divided by the gas-dependent sensitivity factor). The mass-dependent quadrupole mass discrimination (QMD) and electron multiplier gain (EMG) factors are incorporated to retrieve the correct relative abundances of the species. The resultant peaks are summed over and normalized to match the dominant gas-corrected total pressure. Finally, the corrected partial pressure of the species of interest is obtained by dividing the peak height by the corresponding relative sensitivity factor in order to account for its relative ionization efficiency with respect to N_2. The overall uncertainty in the derived absolute abundances of the species is $\sim \pm$ 40 %.

Figure 2.25 shows the flow chart of the data reduction process. Figure 2.26 shows the step-by-step reduction of the raw science data to the calibrated data. Here, the gas correction factor for the total pressure is 1.0 since the spectrum is dominated by water vapour and Nitrogen molecule. The QMD and EMG corrections compensate for the mass dependent transmission efficiency and the detector sensitivity (panels 2 and 3 from top). The total pressure normalization helps estimating the absolute partial pressures of the species (bottom panel).

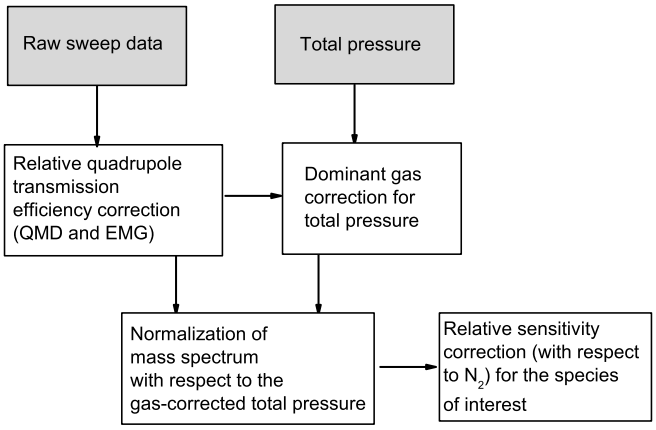

Figure 2.25: The flow chart describing the process of data reduction.

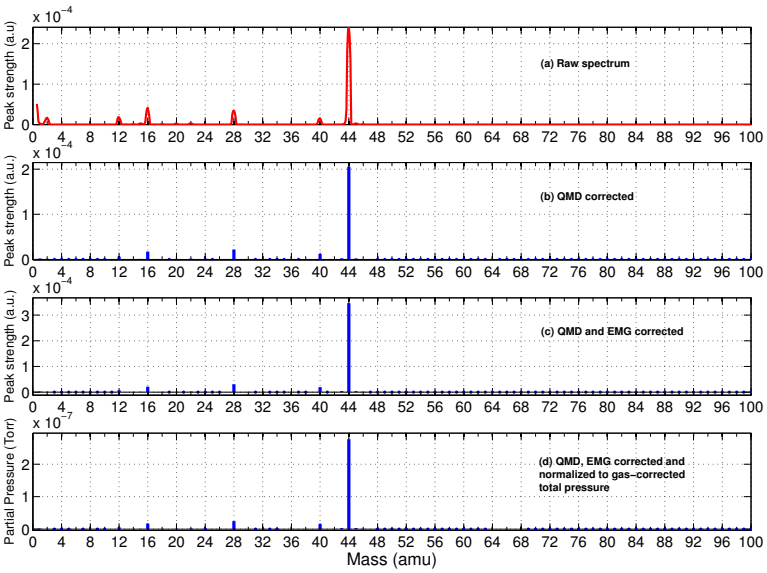

Figure 2.26: The step-by-step processing of the raw mass spectrum during the process of data reduction. The ordinates in the first three panels are plotted in arbitrary units (a.u.). The applications of relative transmission and detection efficiency corrections and normalization with the gas-corrected total pressure are demonstrated here.

The ram pressure enhancement of pressure due to the motion of the MIP through the lunar medium is accounted (*Sridharan et al.*, 2015). The measurements made by CHACE are a convolution of both altitude and latitude variations. The latitude variation brings in the variation of the local surface temperature, which, in turn, controls the altitude distribution of the exospheric species and is used to derive the number density. It is assumed here that the neutrals detected by CHACE were in thermal equilibrium with the lunar surface and the contribution of the sputtered neutrals in the lunar exosphere, if any, is less (*Wurz et al.*, 2007). *Benna et al.* (2015) has shown that the derived scale height temperature based on NMS/LADEE observations is in agreement with the surface temperature, which

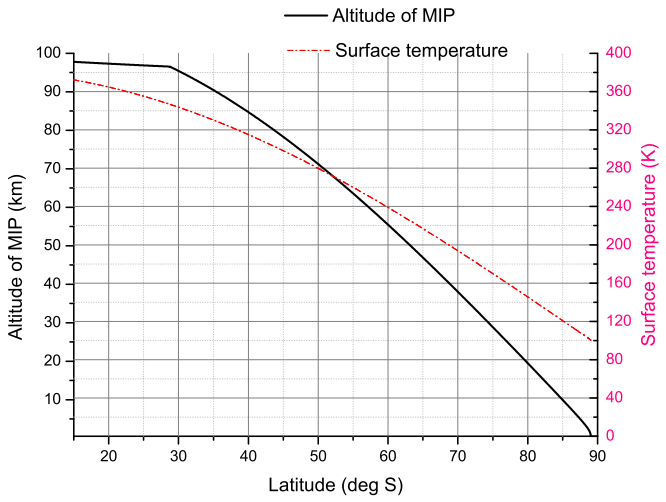

Figure 2.27: The black line shows the latitude-altitude profile of the trajectory of the MIP. The red coloured dotted line shows the variation of the lunar surface temperature as a function of latitude along the ground trace of the MIP. The surface temperature graph is as per the Diviner radiometer observations (*Paige et al.*, 2010*a*).

substantiates this assumption.

The 2D (latitude versus altitude) maps and the surface densities of the species are calculated by using the barometric law (*Chamberlain*, 1963) given by

$$P \;=\; P_0\, exp\left(\frac{r - r_0}{kT/mg}\right) \tag{2.20}$$

Here P is the pressure at a selenocentric distance r, r_0 is the radius of the Moon, T is the surface temperature, m is the mass of the species, P_0 is the pressure at the surface, k is the Boltzmann constant and g is the acceleration due to gravity in Moon. The equation

$$P = nKT$$

is used to convert the pressure (P) to the number density (n).

The barometric law holds good even in the collisionless regime as long as the mean kinetic energy per atom is constant. Barometric law has been used extensively by researchers to describe the vertical profile of the density even in planetary exospheres (*Benna et al.*, 2015; *Hurley et al.*, 2016). A discussion on this is presented in the Appendix. The lunar surface temperature along the MIP ground trace is taken from the global temperature map provided by the Diviner Lunar Radiometer Experiment aboard the Lunar Reconnaissance Orbiter (LRO) *Paige et al.* (2010*a*). Accordingly, an empirical model of the lunar surface temperature variation is adopted in the present analysis with the equatorial temperature of 382 K and polar temperature of 95 K, based on the Diviner temperature map at the subsolar meridian range relevant to the CHACE observations. Figure 2.27 shows the latitudinal and

altitudinal variation of the MIP trajectory and the variation of the lunar surface temperature with latitude along the ground trace of the MIP.

In the subsequent chapters, the observations of CHACE on the lunar exospheric noble gases (Ar, Ne and He) and H_2 will be presented.

Chapter 3

Observations on Argon

The most beautiful experience we can have is the mysterious. It is the fundamental emotion which stands at the cradle of true art and true science.

—Albert Einstein

3.1 The lunar Argon

The Cold Cathode Gauge Experiment (CCGE) of the Apollo-12, 14 and 15 Surface Experiment Packages determined the surface density of $\sim 10^7$ cm^{-3} and $\sim 10^5$ cm^{-3} during the lunar day and night, respectively (*Johnson et al.*, 1972). This results in the day-to-night ratio of the surface number density as $\sim 10^2$.

Hodges and Johnson (1968) predicted that in hydrostatic equilibrium, one would expect lateral flow in the lunar exosphere to establish a relation between surface number density (n) distribution and surface temperature (T), given by $nT^{5/2} = constant$ for non-condensable gases, in the absence of sinks. This is known as the law of exospheric equilibrium for non-condensable gases. The distribution of any condensable gas will deviate from this law.

For typical values of 100 K and 400 K for the lunar nightside and dayside temperatures, the law of exospheric equilibrium for non-condensable gases (*Hodges and Johnson*, 1968) suggests a ratio of $\sim$30. The higher value of the day-to-night surface density ratio measured with CCGE in the lunar exosphere indicated the dominance of non-condensable species, which was later detected by the LACE experiment of Apollo-17 Surface Experiment Package as Argon. Argon is condensable under the prevailing temperature and pressure

conditions on the lunar night side and the polar regions and is one of the important constituents of the lunar neutral exosphere. Out of the two prominent isotopes of Argon, ^{40}Ar and ^{36}Ar, most of the lunar Argon is ^{40}Ar while the isotope ^{36}Ar, which is of the solar origin (*Wieler*, 2002), accounts for only $\sim$10$\%$ of the lunar Ar inventory (*Wieler and Heber*, 2003).

3.1.1 Origin of ^{40}Ar

Lunar ^{40}Ar is a product of the radioactive decay of ^{40}K in the lunar interior (*Hodges*, 1977). The radioactive isotope ^{40}K has an abundance of 0.012 $\%$ in natural Potassium and has a half life of 1.27 $\times$ 10^9 years, which decays to ^{40}Ar by the process of electron capture resulting into the emission of 1.46 MeV gamma ray photon and electron neutrino (*Wetherill*, 1957; *Beckinsale and Gale*, 1969; *Ward*, 1981). The decay equation is given by:

$$^{40}_{19}K + ^{0}_{-1}e^{-1} \longrightarrow ^{40}_{18}Ar + \nu_e + \gamma \text{ (1.46 MeV)}$$

Hodges (1977) proposed that ^{40}Ar must be released from a depth of $\sim$1000 km, in the molten asthenosphere of the Moon. This depth was revised by *Weber et al.* (2011) to be $\sim$1250 km. These depths were arrived at by considering the ^{40}Ar effusion rate of 1.4 $\times$ 10^{21} atoms s^{-1} (*Hodges*, 1977), without attributing much importance to diffusion on the grounds that diffusion is a slow process to explain this effusion rate and the returned lunar rock samples would show a dearth of ^{40}Ar instead of the excess, as reported by *Heymann and Yaniv* (1970).

Killen (2002), using a multipath diffusion code, showed that a source of ^{40}Ar at a depth of $\sim$1000 to 1250 km is not a necessity. Natural diffusion from a crustal depth of $\sim$25 km through micropores and cracks, aided by shallow Moonquakes could account for the effusion rate of ^{40}Ar in the lunar exosphere.

The Ar atoms generated in the lunar interior diffuse to the surface and eventually undergo thermal desorption, which is indicated by the strong diurnal variation of the Argon density (*Hodges and Hoffman*, 1975; *Benna et al.*, 2015). The residence time of Ar on the lunar surface is given by (*Hodges*, 1982):

$$t_{res} = \frac{C}{T^2} exp\left(\frac{4.19Q}{RT}\right) \tag{3.1}$$

where Q is the heat of adsorption in Calories mole^{-1}, 4.19 is Joule's constant, R is the gas constant and T is the surface temperature and C is a constant expressed in s K^{-2}. The physical meaning of the pre-exponential factor is the vibration period (in s) for the van der Waals potential of the adsorbed atom, which is a property of the adsorbing material and

not of the species (*Grava et al.*, 2015*b*). The best model fit to the nightside variation of Ar from the LACE observations yield C= 4×10^{-6} s K^{-2} and Q=6500 Cal $mole^{-1}$. This suggests the residence time of Ar on the lunar nightside ranges between 10^{10} and 10^{2} s for surface temperatures of 80 to 120 K (*Grava et al.*, 2015*b*).

Sputtering, on the other hand, is considered as a source of non-thermal Argon, capable of producing an extended Argon corona (*Chaufray et al.*, 2009), although, with less contribution (*Wurz et al.*, 2007).

3.1.2 Loss processes for ^{40}Ar

Among the loss processes of lunar Argon, photoionization is important. The photoionization life-time of lunar exospheric Argon is ∼34 days for quiet Sun and ∼ 15 days for active Sun (*Huebner and Mukherjee*, 2015). Equally important loss process of the lunar exospheric ^{40}Ar is the charge exchange with solar wind protons (*Grava et al.*, 2015*b*). Electron impact ionization lifetime is ∼ 550 days (*Stern*, 1999). In addition to these permanent loss processes, if Argon is transported to a Permanently Shadowed Region (PSR), it may be condensed. The process of cold trapping may be permanent unless any external source supplies energy to it either by space weathering, shallow Moonquakes, meteor impacts or seasonal warming of the polar regions (*Grava et al.*, 2015*b*). Table 3.1 summarises the different loss processes of the lunar exospheric ^{40}Ar and their relative importances.

Table 3.1: *Loss processes of ^{40}Ar in the lunar exosphere (from Stern (1999); Nakai et al. (1987); Huebner et al. (1992); Grava et al. (2015*b*), and the references therein)*

Process	*Loss rate (atoms s^{-1})*	*Lifetime (Earth-days)*
PSR-cold trapping	3.0×10^{-7}	38
Photo-ionization	3.0×10^{-7} (QS), 6.86×10^{-7} (AS)	38 (QS), 16 (AS)
Charge exchange with solar protons	4.9×10^{-7}	34
Solar radiation pressure	9×10^{-8}	12731
Electron impact ionization	2.1×10^{-8}	5.5×10^{2}
Jeans escape	3.2×10^{-16}	3.6×10^{10}

QS = Quiet Sun, AS = Active Sun

The dominant loss mechanism for lunar Ar is photoionization, although the loss rates

are similar for PSR cold trapping, photoionization and charge exchange with solar wind. This is because of the fact that the flux of ionizing photons (photoionization threshold for Ar is 78.6 nm) is at least two orders of magnitude greater than the solar wind flux (*Huebner et al.*, 1992), and the PSR cold trapping is significant only in 0.03 % and 0.04 % of the total lunar surface area in the North and South poles, respectively (*Grava et al.*, 2015*b*).

Figure 3.1 shows a schematic of the main source, sink and transport processes acting on the lunar Ar exosphere.

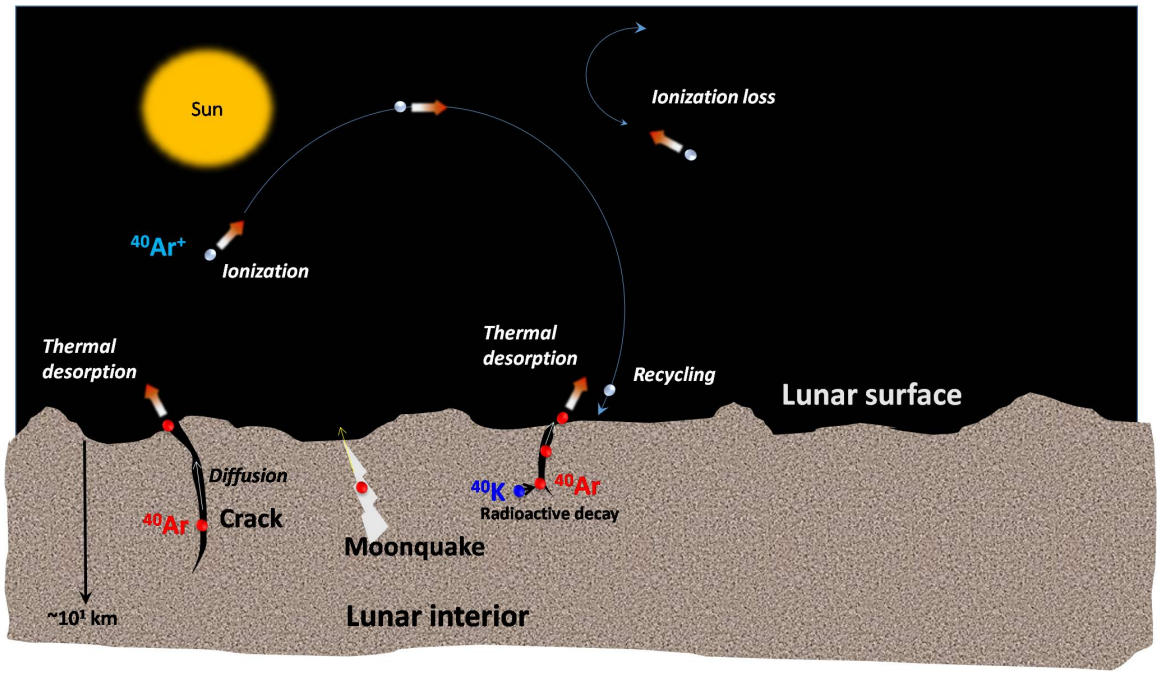

Figure 3.1: Schematic of the main processes in the lunar Argon exosphere.

3.2 Previous observations

Lunar Argon was first detected by the LACE mass spectrometer, emplaced on the lunar surface as a part of the Apollo-17 Lunar Surface Experiment Package (ALSEP) in 1972 (*Hoffman et al.*, 1973; *Hodges and Hoffman*, 1975).

In-situ observations by LACE (*Hodges and Hoffman*, 1975) and NMS (*Benna et al.*, 2015; *Hodges and Mahaffy*, 2016) have clearly shown that the synodic variation of ^{40}Ar is characteristic of a condensible gas. The slow post-sunset decrease and a sharp increase during sunrise in ^{40}Ar density have been shown to systematically repeat from one lunation to another. It is suggested that the sudden increase recorded before sunrise could, in all probability, be associated with a part of the desorbed gas from the sunlit surface drifting across the terminator into the night sector (*Stern*, 1999; *Grava et al.*, 2015*b*). Typically, the extrapolated/modeled daytime values were at least two orders of magnitude larger with

reference to the night side measurements. Even with the spot measurement data from LACE, *Hodges* (1973) could get evidence for a potentially varying source of ^{40}Ar, i.e., for a varying release rate of ^{40}Ar from the lunar interior, possibly associated with Moonquakes (*Hodges and Hoffman*, 1975). There were attempts during Apollo 15 and 16 missions wherein mass spectrometers were flown in the service modules but with limited success. One of the objectives of the studies carried out by *Hodges et al.* (1972) was to look for lunar volcanism. The ^{40}Ar:^{36}Ar ratio has been shown to be $\sim$3.5. No further details are available from the orbiter data even for the anti-sunward side, leave alone the sunlit side. Lunar Argon was also studied by the LAMP ultraviolet spectrometer aboard LRO at 104.8 and 106.7 nm fluorescent emission wavelengths, and an upper limit of 2.3×10^4 cm^{-3} is reported (*Cook et al.*, 2013), which is $\sim$1.5 times lower than the upper limit given by LACE (*Hodges and Hoffman*, 1975).

Recently, the NMS instrument aboard LADEE orbiter has studied the diurnal variation of the lunar exospheric Argon in the low latitudes ($\pm$ 23°) for a period of five months. NMS observations have brought out significant evidences of the lunar surface-exosphere interaction through the spatial inhomogeneity of the lunar exospheric Argon (*Benna et al.*, 2015). NMS has observed localized enhancement of ^{40}Ar at the Western maria, coincident with the potassium-rich KREEP regions, suggesting the close interaction between the surface and the exosphere, characteristic to the surface boundary exospheres (*Benna et al.*, 2015).

The NMS observations have also revealed synodic and semiannual oscillations of ^{40}Ar (*Hodges and Mahaffy*, 2016). The semiannual oscillation of ^{40}Ar is found to be consistent with condensation loss in the seasonal cold traps at the poles due to the obliquity of the Moon. The results show that the exospheric morphology depends on the energetics of desorption of atoms from soil grains. It also brought out the importance of the surface-exosphere interaction process.

In addition to the observations, several modelling studies on lunar Argon have been conducted (*Hodges et al.*, 1974; *Hodges and Hoffman*, 1975; *Hodges*, 1975; *Chaufray et al.*, 2009; *Grava et al.*, 2015*b*). These models accounted for cold trap condensation/adsorption of Argon on the lunar surface along with the ionization loss process. Attempts were even made to take into account of the Argon ions produced by the solar UV and then accelerated in the convective electric field of the solar wind towards the lunar surface and eventually getting implanted in the Lunar regolith and neutralized (*Manka and Michel*, 1971). The importance of the charge exchange process with the solar wind protons is also considered in the recent model of the lunar exospheric Argon (*Grava et al.*, 2015*b*).

In the present chapter, observation on the latitudinal variation of ^{40}Ar in the sunlit lunar exosphere and the relative variation of ^{40}Ar with respect to ^{36}Ar, based on the CHACE observation are reported. Since ^{40}Ar is produced from the lunar interior, it is directly

controlled by the processes in the lunar interior and hence it is expected to show some relation with the lunar topography. Since the main orbiter Chandrayaan-1 had a Lunar Laser Ranging Insturment (LLRI), the ratio of ^{40}Ar with respect to ^{36}Ar has been correlated with the LLRI-measured topography along the ground track of the MIP. The combined findings give us clues on the possible spatial heterogeneity of the radiogenic activity of the lunar interior.

3.3 Observations and Results

Sample spectra obtained by CHACE covering the mass range of 35-41 amu are depicted in Figure 3.2 to highlight the quality of data that has been obtained. The significance and variability of these isotopes could be ascertained from Figure 3.2 at different stages of the mission. The first two panels (a, b) of the spectra in Figure 3.2 were obtained when the MIP was still attached to the main orbiter, while panels c and d correspond to times when the MIP was racing towards the south pole.

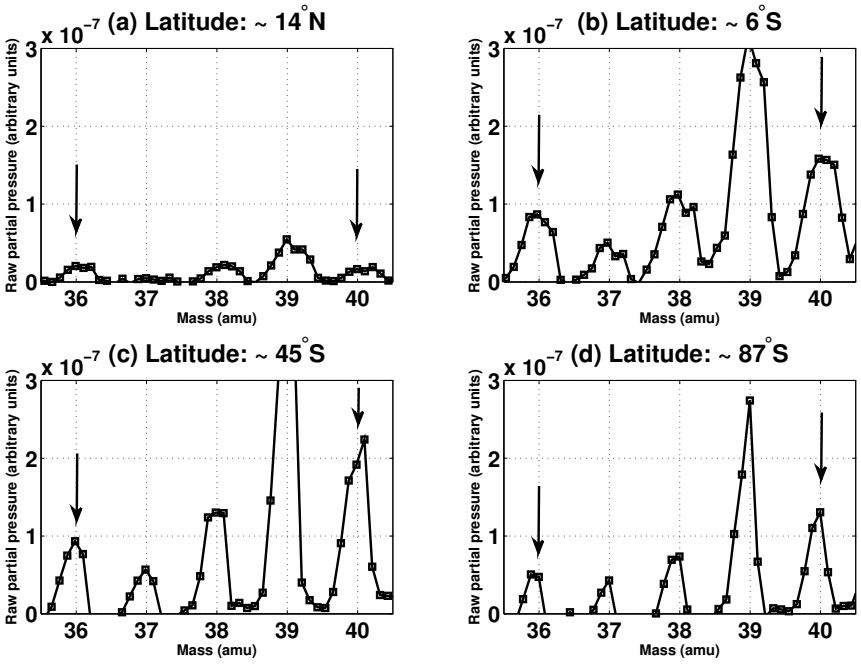

Figure 3.2: Sample raw spectra covering the mass range of 36 to 40 amu showing the presence of ^{40}Ar and ^{36}Ar. For panels (a) and (b), the altitude of observation was $\sim$98 km, i.e. before the separation of the MIP from the spacecraft. For panel (c), the altitude of observation was $\sim$80 km and for panel (d), the observation was close to the surface of the Moon.

3.3.1 Distribution of ^{40}Ar

When the partial pressures or absolute number densities of different species are to be dealt with, it is essential to ensure that the instrument has stabilized, which, in the case of CHACE, is ∼20 minutes after switch ON, during which time the MIP had crossed 20° S. Thus, data beyond 20° S are considered to calculate the absolute density of ^{40}Ar. Figure 3.3 shows the number density of ^{40}Ar (colour coded), along the MIP trajectory in latitude and altitude.

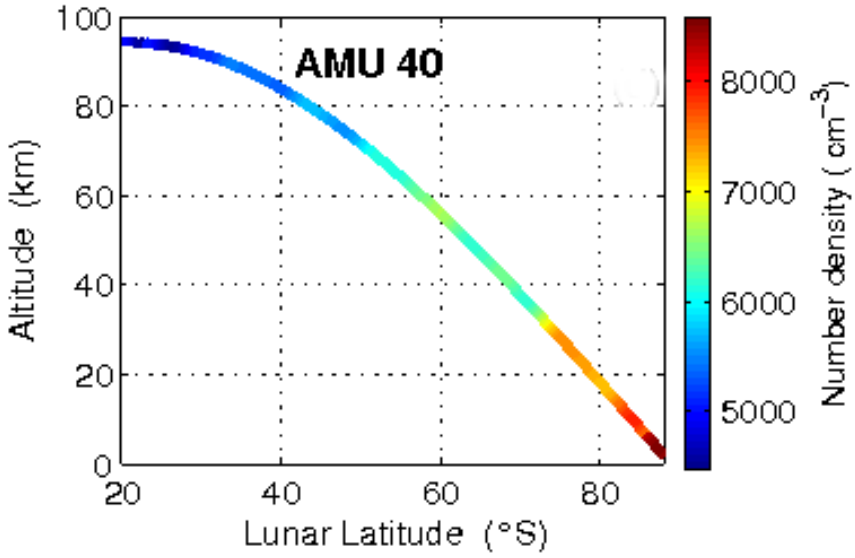

Figure 3.3: The number density of ^{40}Ar from the in-situ measurements of CHACE along the MIP trajectory. The measurements are convolution of altitudinal and latitudinal effects.

The top panel of Figure 3.4 shows the surface density of ^{40}Ar derived from the in-situ observations of CHACE by using barometric law using the local scale heights. In the absence of any surface heterogeneity, one would have expected to see a smooth variation in the latitudinal distribution of ^{40}Ar. In contrast, it is seen that, there are several undulations. To facilitate viewing the small scale undulations from the mean trend (presumably due to the surface temperature variation with latitude), a fourth order polynomial fit representing the mean trend has also been superposed on the plots along with the number densities. A maximum fluctuation of ∼5% is observed about the mean trend. These short scale variations of the ^{40}Ar surface number density are proposed to be associated with the lunar surface topography (*Sridharan et al.*, 2013*a*). The bottom panel shows the surface topography obtained from the LLRI on Chandrayaan-1 (*Kamalakar et al.*, 2009). The LLRI data corresponding to the longitude zone of the MIP ground track had been stripped out of the main data base and the topological features were extracted (*Sridharan et al.*, 2013*a*).

Since ^{40}Ar is a by-product of radiogenic activity from the lunar interior, it is expected that its concentration would increase in the regions of deep craters and decrease along with

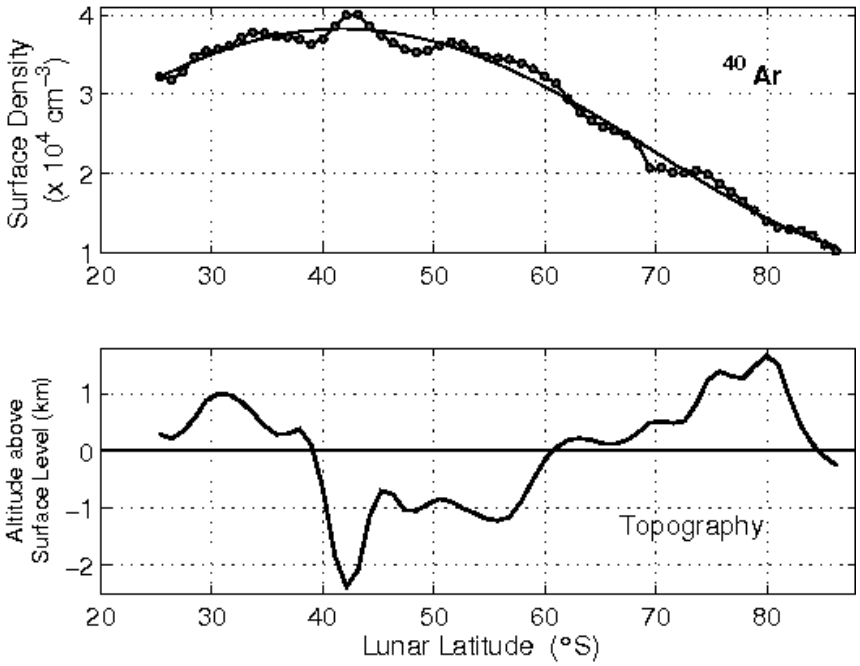

Figure 3.4: The top panel shows the surface density of ^{40}Ar derived using barometric law from the CHACE observations. The lower panel shows the lunar surface topography obtained using LLRI data along the ground track of the MIP. The anti-correlation of the trends of the surface density and the elevation from $\sim$ 42°S till the South pole is quite evident.

high elevation regions. While making the comparison, the mean reference - zero elevation line - for the LLRI data had been considered. The striking observations from Figure 3.4 are: from $\sim$42°S to $\sim$80°S the elevation registered an increasing trend from $\sim$-2.3 km to $\sim$+1.6 km and there had been a corresponding decreasing trend from $\sim 4 \times 10^4$ cm^{-3} to $\sim 1 \times 10^4$ cm^{-3} in the ^{40}Ar surface number density. Further, it could also be noted that the undulations in the ^{40}Ar density are nearly of the same scale lengths as revealed by the ranging instrument in the whole region under consideration. The elevation range of the lunar surface between 25° to 30° S along the ground trace of the MIP is 0-1 km. Similar range of elevation is observed between 60° to 75° S. However, the ^{40}Ar surface number density in these two regions differ by almost a factor of 2. This indicates spatial heterogeneity of the lunar ^{40}Ar.

The in-situ observations by CHACE are used to generate the 2-dimensional (latitude versus altitude) distribution map with a resolution of 1° in latitude and 5 km in altitude, using the barometric law, as shown in Figure 3.5.

The deviations from the mean concentration of ^{40}Ar show that, the deeper one goes into the lunar interior, more would be the ^{40}Ar density (*Sridharan et al.*, 2013*a*). These variations point to the important role of lunar surface processes in modulating the ^{40}Ar densities. Any long lived species, over time, would tend to get uniformly distributed. However, it may not be the case for a gas that has a source spatially distributed and source

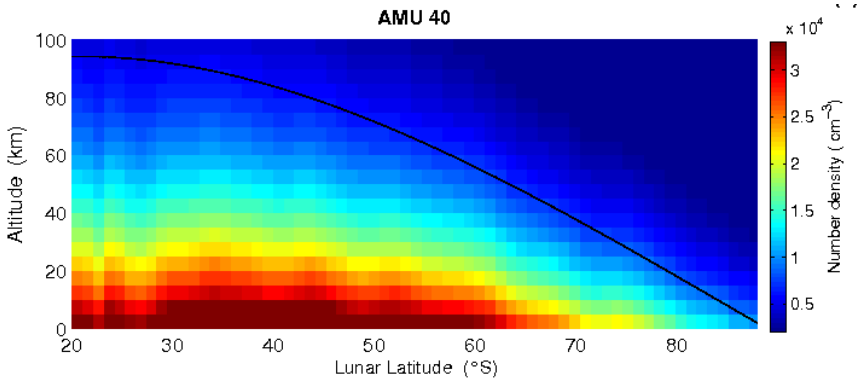

Figure 3.5: Two dimensional (latitude versus altitude) map of lunar ^{40}Ar along the trajectory of the MIP.

strength larger in comparison with the redistribution. In the absence of such a factor, as mentioned above, the variations would have been smooth (dictated only by the surface temperature variation with latitude). In the case of a SBE, the very fact that undulations are present in the density indicates the possible decisive role of lunar surface.

3.3.2 The ^{40}Ar:^{36}Ar ratio

The summary of the important findings of LACE on lunar Argon have been succinctly provided by *Stern* (1999) and *Wieler and Heber* (2003). The conclusion that ^{40}Ar is of lunar origin is essentially based on the relative concentration of ^{40}Ar with respect to ^{36}Ar. This ratio has to be $\sim 10^{-4}$ if these two isotopes are of solar wind origin (*Wieler*, 2002). On the other hand, the measurements from LACE in the Apollo-17 Surface Experiment Package revealed that, the ratio remained >1 all the times, and in fact, typically varied from 7.5 to 10 over the Apollo-17 landing site. This ratio was characteristic to the LACE deployment site as it is believed that LACE has observed significant amount of Moonquake-released Argon over and above the steady state Argon inventory (*Grava et al.*, 2015*b*).

On the other hand, CHACE has studied the variation of this ratio over a broad range of latitudes, as it was switched on at 40°N and the measurements continued till the MIP impacted close to the South Pole. When the ratios of the relative amplitudes are considered, stabilization of the instrument is not mandatory since within the short time span of $\sim$250 ms taken to cover the mass range of 36 to 40 amu the instrument characteristics are not likely to change. Therefore even when the instrument is just getting stabilized, ^{40}Ar: ^{36}Ar ratio could be studied. Results are depicted in Figure 3.6, wherein 15 point running average (equivalent to $\sim$100 km ground range) has been shown (continuous line) in addition to actual ratios in every sweep (red open circles). The average ratio initially registered a value of $\sim$1, over the lunar latitude of 40°N, then increased to $\sim$2.25 over 12°S and remained centred around this value till the point of impact. There are large and small undulations all through, which could on occasions, reach as large as 30% of the mean value. One

important aspect of the above result is that the ratio was consistently larger than that corresponding to the solar wind, indicating the potential radiogenic activity in the lunar interior and its possible variation along the ground track.

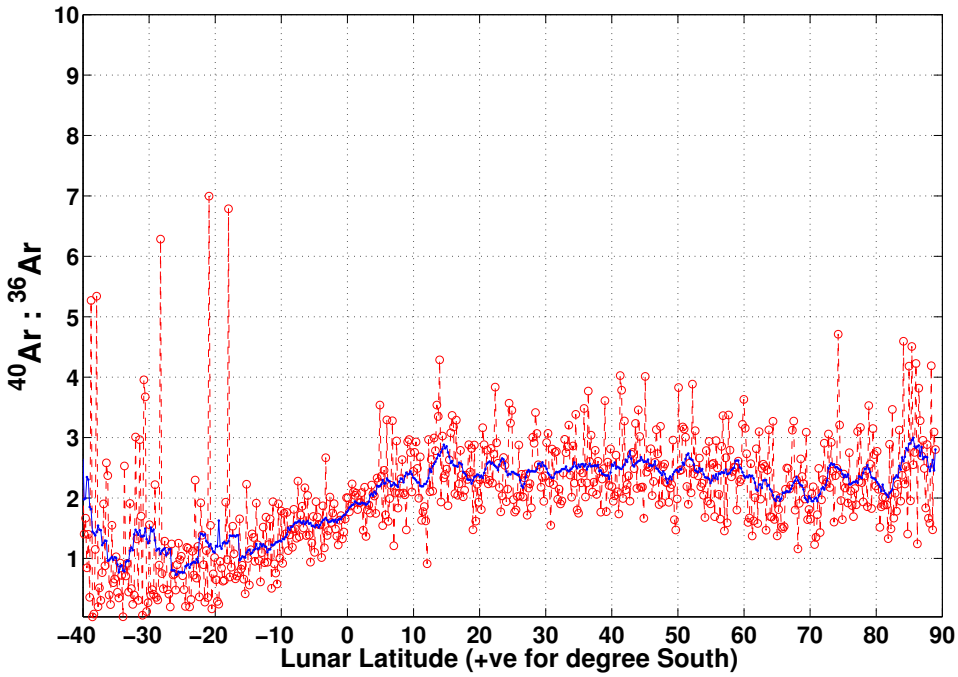

Figure 3.6: Variation of the ^{40}Ar:^{36}Ar ratio as obtained by CHACE. The red markers are the observed ratios while the blue continuous line is a 15 point moving average, which is equivalent to $\sim$ 100 km of ground trace.

In this context, some of the earlier results on the ^{40}Ar:^{36}Ar ratio and their possible relation to the de-gassing history of the lunar surface under consideration become important. *Wieler and Heber* (2003) have exhaustively discussed about the noble gas isotopes on the Moon and have highlighted how these 'parentless'gases could be used to constrain the degassing history of the Moon itself. The parentless ^{40}Ar is used as a semi-quantitative measure of the 'antiquity'of a soil, i.e., the time in the past when a sample was exposed to the solar wind at the top of the regolith. ^{40}Ar concentration needs to be normalised to the length of time a sample had spent on the surface for which ^{36}Ar from the solar wind could be used as proxy. It is believed that the ^{40}Ar:^{36}Ar ratio in any sample that had been irradiated by the solar wind for several billion years would be higher than in the sample that received the radiation later. This implies that higher the ratio of ^{40}Ar:^{36}Ar in any sample, the older the sample would be. A cross calibration has been provided by *Eugster et al.* (2001), which clearly indicates that a ratio of $\sim$13 would correspond to an antiquity of $\sim$3.7 Gy while a ratio of $\sim$0.5 would correspond to $\sim$10 My. Figure 3.7 depicts the re-plotted cross calibration of the basic inputs given by *Eugster et al.* (2001) and *Wieler and Heber* (2003). The ^{40}Ar:^{36}Ar ratio after the instrument stabilization is seen to be centred $\sim$2.25 in the southern hemisphere of the near side of the Moon. This would imply an antiquity of $\sim$1.5 Gy for the longitudinal segment corresponding to the ground track of

the MIP as shown in the figure. This result opens up an interesting possibility of getting the 'antiquity'of the entire lunar surface by means of composition measurements from an orbiter around the Moon. An empirical relation highlighted in the figure has been worked out relating the ratio to the antiquity. Further, going by Figure 3.6, one notices that the ratio had remained around 1 in the northern hemisphere which indicates for the antiquity of this region to be around 600 My. This requires further confirmation and more systematic measurements need to be carried out in future.

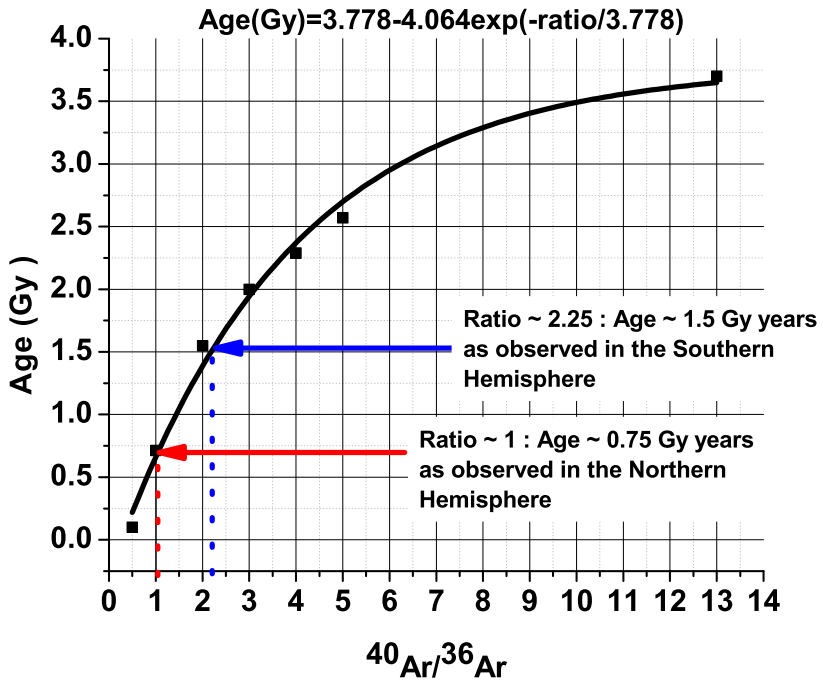

Figure 3.7: Redrawn antiquity estimates of the lunar samples along with their corresponding ^{40}Ar:^{36}Ar ratios using the basic data from *Eugster et al.* (2001) along with the present estimates for both the Northern and Southern hemisphere values.

In the context of the above results on the antiquity of the southern hemisphere, it is interesting to compare them with the elemental maps generated by the earlier missions. *Lawrence et al.* (1998, 1999), *Yamashita et al.* (2010) and *Hasebe et al.* (2009) have produced lunar maps for Thorium, Potassium, Uranium and Iron using gamma ray spectrometry from the Lunar Prospector and Kaguya missions. These maps were generated while delineating the compositional variability and evolution of the lunar highlands which contain KREEP- rich materials (potassium, (K), Rare Earth Elements (REE) and phosphorous (P)). Since KREEP rich rocks are believed to have formed in the lunar crust-mantle boundary as the final product of the initial differentiation of the Moon, their distribution would yield information on the temporal evolution of the lunar crust. *Zhu et al.* (2010) have reported similar results from the Chang'E-1 mission that carried a gamma ray spectrometer. They had confirmed the earlier results reported by *Lawrence et al.* (1998, 2000) including

the correlation between the radioactivity and lunar topography. Thus, the gamma ray spectrometry could yield absolute information on large scale features. The lunar maps shown by the earlier workers clearly demarcate the far and the near side of the Moon, the far side showing substantially less counts than the near side. Even in the near side, large differences exist both along the latitude and longitude. For example maximum potassium concentration has been shown to be localized and centred around $\pm$ 15° S latitude and 0 to 40° W longitude with an irregular structure in the periphery (*Lawrence et al.*, 1998; *Zhu et al.*, 2010). The ground projection of the MIP trajectory was centred around 14°E. As the ground track covered large number of small and medium craters, and in all probability, the sort of undulations revealed in the ^{40}Ar:^{36}Ar ratio might correspond to the surface heterogeneity. Since there is no mixing of the atmospheric constituents in the lunar atmosphere, the concentration at any point in the atmosphere would be directly linked to the source region at the surface.

3.4 Concluding remarks

The CHACE experiment on the Moon Impact Probe of Chandrayaan-1, enabled us to obtain the daytime lunar atmospheric composition with unprecedented altitude and latitude coverage. In this chapter, the 2-D (latitude versus altitude) distribution of the lunar exospheric ^{40}Ar is presented. The number densities presented here agree well with the previous estimates. The remarkable feature observed in the 2D maps is the significant spatial heterogeneity. Such heterogeneity had been earlier reported by NMS aboard LADEE (*Benna et al.*, 2015) in the distribution of ^{40}Ar, in the low latitude region.

The in-situ measurements of the ratio ^{40}Ar:^{36}Ar and the laser based topography data bring out the heterogeneity in the radiogenic activity of the lunar interior, with a very high spatial resolution in addition to providing semi quantitative antiquity of the region falling under the ground track. This opens up the interesting possibility of using the ratio of the noble gas isotopes to establish the antiquity of the whole Moon by suitably planning the lunar atmospheric composition measurements in future missions.

The results reported here highlight the complexities of the lunar exosphere and the significant role of the lunar surface processes in modulating the distribution of the different species and also highlighting the importance of more in-situ measurements.

Chapter 4

Observations on Neon

My Poet, is it thy delight to see thy creation through my eyes and to stand at the portals of my ears silently to listen to thine own eternal harmony ?

—Rabindranath Tagore

4.1 The lunar Neon

Neon is known to be the most volatile element after Helium (*Lodders*, 2003). Neon in the solar system owes its origin to the solar wind, and its isotopic composition is a proxy to the composition of the outer convective zone of the Sun (*Heber*, 2002). While the solar wind is composed mostly of Hydrogen and Helium ions, Neon is a trace constituent with abundance $\sim 10^{-4}$ times that of the Hydrogen ions (*Lodders*, 2003). The isotopic composition of the primordial Neon is beleived to have been preserved in the solar interior, since the large Coulumb barrier of the Neon isotopes protect these nuclides from alteration (*Kallenbach et al.*, 1997).

Due to its volatile nature, the abundance of Neon in the planetary materials is several orders of magnitude less than the solar abundance (*Kallenbach et al.*, 1997; *Lodders*, 2003). Another reason for the depletion of Neon in the planetary bodies is beleived to be degassing from the interior resulting into hydrodynamical escape (*Hunten et al.*, 1991). Neon is a trace constituent in the Earth's atmosphere with an abundance of $(10.0 \pm 0.1) \times 10^{-12}$ g/g (*Pepin*, 1997), which is about two orders of magnitude less than the solar abundance (*Marty*, 2012) .

Neon is yet another noble gas constituent of the lunar neutral exosphere. Lunar Neon is mostly ^{20}Ne, which is non-condensable even in the lunar night side and the PSRs.

4.1.1 Origin of ^{20}Ne

Since Moon does not have a global magnetic field, the solar wind ions are directly implanted onto the surface. A substantial fraction of them may be neutralized and become a part of the lunar exosphere. It is understood that the lunar Neon exosphere owes its origin to the Neon ions present in the solar wind (*Wieler*, 2002). The solar wind origin of the lunar Ne is substantiated by the fact that both solar wind and lunar samples have shown similar values of the Neon isotope ratio, i.e. ^{20}Ne: ^{22}Ne $\sim$ 13.8 (*Wieler*, 2002; *Wieler and Heber*, 2003). The Neon implanted on the lunar surface thermally desorbs and becomes a part of the lunar exosphere (*Benna et al.*, 2015).

4.1.2 Loss processes for ^{20}Ne

Among the loss processes of lunar Neon, photoionization is important. Electron impact ionization life-time is very high compared to the photoionization life-time. Table 4.1 summarises the different loss processes of the lunar exospheric ^{20}Ne and their relative importances.

Table 4.1: *Loss processes of ^{20}Ne in the lunar exosphere (from Huebner and Mukherjee (2015); Kim and Rudd (1994))*

Process	*Loss rate (atoms s^{-1})*	*Lifetime (Earth days)*
Photoionization	1.84×10^{-7} (QS) and 5.87×10^{-7} (AS)	58 (QS) and 20 (AS)
Electron ionization	8.2×10^{-9}	1.4×10^{3} ($\sim$ 3.8 Earth years)

Figure 4.1 shows a schematic of the main source, sink and transport processes acting on the lunar Neon exosphere.

4.2 Previous observations

The ^{20}Ne signature observed by LACE in the Apollo-17 surface experiment package was believed to be contaminated by the signal of $H_2^{18}O$ from Apollo equipment (*Hodges et al.*, 1973). There was an attempt to estimate the possible concentration of the neutral ^{20}Ne from the measurements of the fluxes of ionized Neon from the Suprathermal Ion Detector

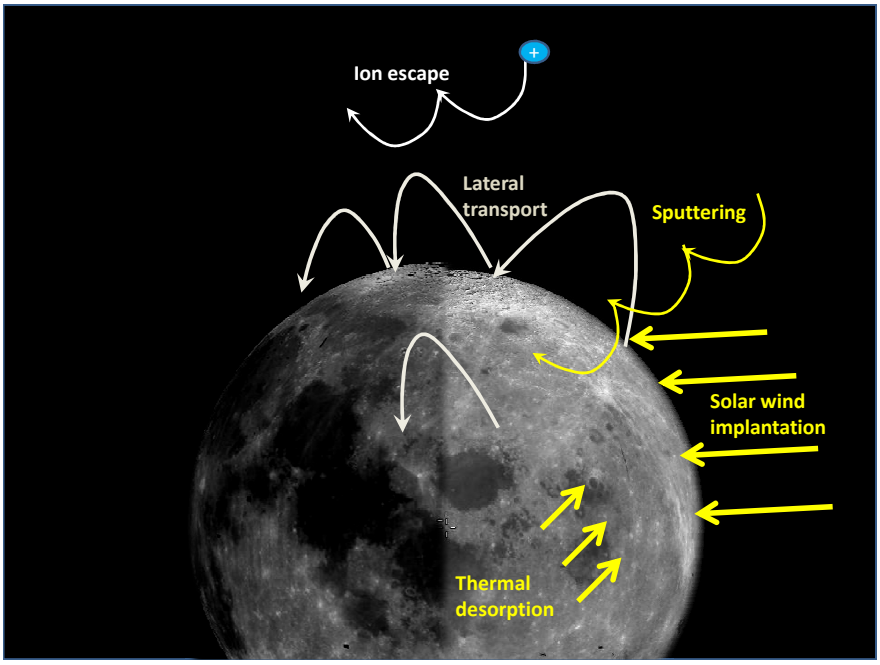

Figure 4.1: Schematic of the main processes acting on the lunar Neon exosphere.

Experiment (SIDE) emplaced by Apollo 12, 14 and 15 missions (*Benson et al.*, 1975; *Freeman and Benson*, 1977). The estimated surface concentration of Neon at the terminator crossing was 10^5 cm^{-3}. Owing to the different uncertainties involved in the estimation of the concentration of neutral Neon from its ion fluxes and also due to the lack of the observations on neutral Neon, the inference on ^{20}Ne from SIDE data was largely ignored in later analyses (*Stern*, 1999).

Since there was no reliable observations from LACE on Neon, work resorted to model calculations (*Hodges*, 1973; *Hodges et al.*, 1973) and the concentration of Neon during the lunar day was estimated as (4-7)$\times 10^3$ cm^{-3}. In the decade of 1970s, concentrations of different constituents of the lunar exosphere including ^{20}Ne were calculated by several researchers (*Johnson et al.*, 1972; *Hodges*, 1973; *Hodges et al.*, 1974; *Hoffman and Hodges*, 1975; *Mukherjee*, 1975) and the ^{20}Ne concentrations of 4×10^3 to 10^4 cm^{-3} for lunar day-time and 10^5 cm^{-3} for lunar night-time were reported in the lunar sourcebook (*Heiken et al.*, 1991). *Wurz et al.* (2007) calculated the lunar Neon based on solar wind implantation as 4900 cm^{-3}.

Later, *Cook et al.* (2013) reported an upper limit of 4400 cm^{-3} for the surface number density of Neon based on the observation of 63 nm ($2s^2 2p^5 4s \rightarrow 2s^2 2p^6$) and 73.5 nm ($2s^2 2p^5 3s \rightarrow 2s^2 2p^6$) spectral lines from the LAMP instrument aboard Lunar Reconnassaince Orbiter. Recently, the NMS instrument aboard the LADEE spacecraft has reported the diurnal variation of Neon at lower latitudes (*Benna et al.*, 2015) during the observations

in February 2014. It is observed that the Ne density peaks to $\sim 3.5\times 10^4$ cm^{-3} about 10° prior to the lunar sunrise because of the progressive cooling of the surface, and drops sharply by more than two orders of magnitude because of the increase in the surface temperature.

In this context, the observations by the CHACE experiment aboard the MIP in the Chandrayaan-1 mission are significant as they provide the latitudinal and altitudinal variations of ^{20}Ne (hereafter to be referred to as Neon) in the sunlit lunar exosphere. The CHACE experiment studied for the first time the constituents of the sunlit lunar exosphere with broad latitudinal (45° North to the South pole) and altitudinal (∼98 km to the surface) coverage (*Sridharan et al.*, 2010*a*,*b*; *Sridharan et al.*, 2013*b*; *Sridharan et al.*, 2013*a*, 2015; *Thampi et al.*, 2015). The observation of Neon by CHACE is reported in this chapter. The derived surface number densities from CHACE are compared with those obtained from the NMS/LADEE observations.

4.3 Observations and Results

The CHACE instrument used 70 eV electrons to impact-ionize the ambient neutrals. The doubly ionized ^{40}Ar, i.e. Ar^{++}, would contribute to the m/q = 20 bin of the mass spectra. NIST has listed a value of the Ar^{++}:Ar^{+} ratio as 13%. The laboratory calibration data of the CHACE instrument acquired by inserting laboratory grade Ar-40 in the vacuum chamber yielded a value of 14.5% at 70 eV electron energy. *Montanari and Miraglia* (2014) compiled the experimental work of several workers to determine the electron impact ionization cross sections of Argon and compared the results with theoretical calculations, suggesting a value of the Ar^{++}:Ar^{+} ratio as 8.7% (0.087), which is on the lower side. Since the present work aims at investigating the upper limits of the Neon density, the value of 0.087 of the Ar^{++}:Ar^{+} ratio is used to remove the Ar^{++} contribution from the amu 20 signal to obtain the Neon number density. Also, results of the sensitivity analysis presented in section 4.3.1 show that the number density of Neon is not very sensitive to the Ar^{++}:Ar^{+} ratio at the high latitudes.

Two important instrument calibration factors are the relative gain of the CEM detector and the relative transmission efficiency of the quadrupole mass analyser (due to quadrupole mass discrimination) at amu 20 with respect to amu 40. For the CHACE instrument, the relative gain of the CEM detector and the relative transmission efficiency of the quadrupole mass analyser at amu 20 with respect to amu 40 are 1.25 and 1.6, respectively. In addition to these calibration factors, the relative (with respect to N_2) ionization sensitivity factors of ^{40}Ar and Neon (1.11 and 0.28, respectively) are also taken into account. The total number density was derived by accounting for the local surface temperature on the Moon and also by applying the correction for the ram pressure enhancement due to the velocity of the

MIP (*Sridharan et al.*, 2015).

Significant information on the lunar global surface temperature distribution was provided by the Diviner Lunar Radiometer Experiment aboard the LRO, which brought out the diurnal and latitudinal variabilities of the lunar surface temperatures by mapping the albedo of the Moon at infrared wavelengths (*Paige et al.*, 2010*b*). Accordingly, a cosine model of the lunar surface temperature variation is adopted in the present analysis with the equatorial temperature of 382 K and polar temperature of 95 K, based on the Diviner temperature map at the Local Solar Time (LST) relevant to the CHACE observations. The Diviner observations have revealed distinct variations of the lunar surface temperature at higher lunar latitudes including patches of very low temperature regions (from 80° towards poles), ranging down to 25 K (*Paige et al.*, 2010*a*) at the permanently shadowed regions (PSR) on the lunar surface. In addition, the local surface temperatures at higher lunar latitudes have significant spatial and temporal variations due to the variations of the solar incidence angle owing to the local topography. Due to the inhomogeneity of different surface parameters that govern the local surface temperature, any analytical model would deviate from the actual values. Analytical modeling of the lunar surface temperatures for exospheric modeling using Diviner observations deviate from the measured lunar surface temperature near the terminators and higher lunar latitudes (*Hurley et al.*, 2015) due to local variations in the solar incidence angle. The local fluctuations of the surface temperature at higher lunar latitudes translate to fluctuations in the spatial distribution of the number density observed by CHACE.

Fig. 4.2 presents the number densities of Neon as a function of the lunar altitude and latitude derived from the partial pressure measurements and accounting for the corrections as mentioned above.

The Fig. 4.3 shows the surface number density of Neon as a function of the lunar latitude, derived using the scale heights at different latitudes assuming a cosine model of temperature consistent with the Diviner observations (*Hurley et al.*, 2015). The surface number density from the CHACE observations are seen to vary (1σ variation) from 7×10^3 to 22×10^3 cm^{-3} near the pole, 3×10^3 to 5×10^3 cm^{-3} in mid (50°S) latitudes, and 0.5×10^3 to 1.1×10^3 cm^{-3} in lower (20°S) latitudes. This is due to the non-condensible behaviour of Neon at Moon. The filled circles in the figure represent the mean of the number densities derived from 10 consecutive spectra acquired by CHACE, leading to a latitudinal binning of $\sim 2°$. The error bars are standard deviations on the observations within a bin. The higher values of the standard deviations in the CHACE observations at the higher latitudes are attributed to the high inhomogeneity in the local surface temperature due to the local topography.

The results are compared with the number density derived from the NMS instrument aboard the LADEE spacecraft. The NMS observed the lunar exosphere in the mass range

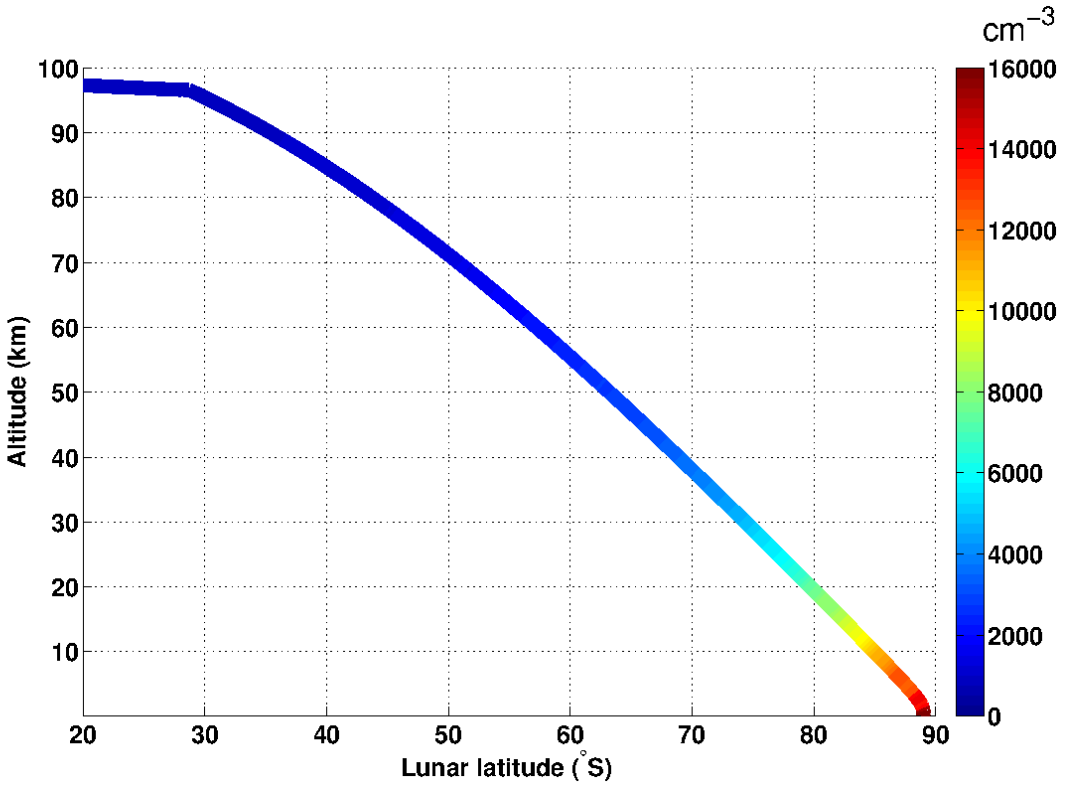

Figure 4.2: Number density of Neon as a function of lunar latitude and altitude in the sunlit lunar exosphere derived from CHACE measurement.

of 2 to 150 amu and observations on the variability of Neon in the lunar exosphere have been reported (*Benna et al.*, 2015). The calibrated science data from the PDS webpage along with the ephemeris information provided as the SPICE Kernels by Navigation and Ancillary Information Facility (NAIF) are used to calculate the surface number densities of Neon on 25 December 2013, 18 March 2014, and 21 January 2014, when the Moon was in the geomagnetic tail. The counts corresponding to amu-20 are extracted from each mass spectrum, and converted to number densities. These values are corrected to remove the contribution from Ar^{++}, using the number density values obtained for amu-40. The corrected values for Neon are converted to the surface values using the local scale height. The time information in the data is converted to Local Solar Time (LST), expressing the local time on a 24 hour clock. In this scale, 12:00 LST represents the sub-solar meridian, 06:00 LST represents the sunrise terminator and 18:00 LST represents the sunset terminator. From the three orbits, the data corresponding to the LST between 10.00 and 11.00 hours are used to compare with the observations of the sunlit lunar exosphere by CHACE. The results from NMS/LADEE observations indicate that the surface number density of Neon is $\sim 10^3$ cm^{-3} in the lower lunar latitudes. This is consistent with the derived surface number density from CHACE observations at lower latitudes.

A two dimensional (latitude and altitude) map of the number density of Neon is generated based on its scale height at different latitudes. The result is shown in Fig. 4.4.

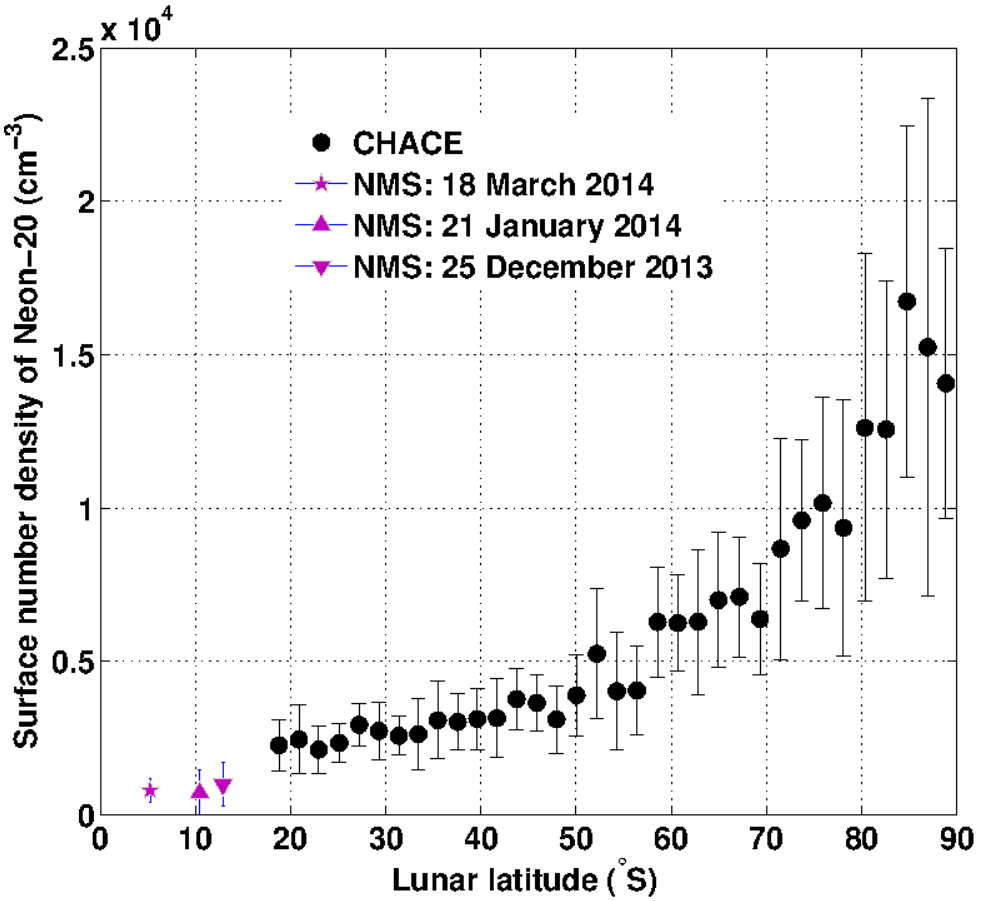

Figure 4.3: Variation of surface number density of Neon with latitude in Southern hemisphere of the Moon observed by CHACE (filled circles). NMS/LADEE observations shown here were made on 25 December 2013, 18 March 2014 and 21 January 2014, when the Moon was in the magnetotail of the Earth, similar to the CHACE observation.

It shows a higher concentration of the Neon at the higher lunar latitudes. The black continuous line represents the MIP track during the observation made by CHACE.

4.3.1 Sensitivity analysis

The derived values of the number densities are sensitive to two parameters, *viz.*, the local lunar surface temperature and the ratio of double to single electron impact ionization cross section of ^{40}Ar at 70 eV. A sensitivity analysis is conducted in order to study the variation in the number density of Neon with respect to the lunar surface temperature profile and the Ar^{++}:Ar^{+} electron impact ionization cross section ratio. The lunar surface temperature profile depends on the local surface mineralogy, emissivity, as well as the local topography. Heterogeneity of the lunar surface mineralogy and emissivity, as well as the sensitivity of the solar incidence angle to the local topographical variations (especially in the higher latitudes), the analytical surface temperature profiles are always associated with uncertainties. These uncertainties are more at the higher lunar latitudes (*Hurley et al.*,

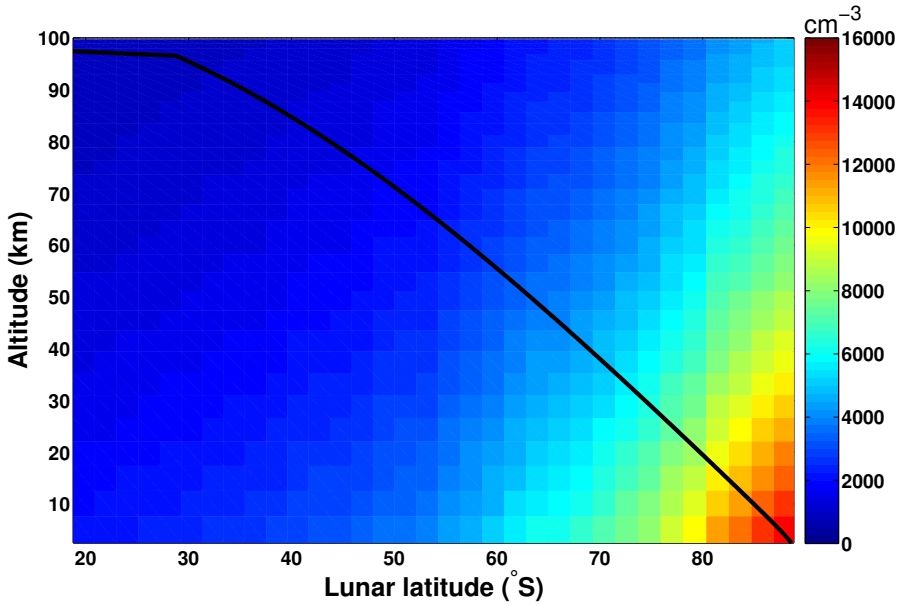

Figure 4.4: A two dimensional (latitude vs altitude) distribution of Neon generated using the scale heights at different latitudes for the 14°E lunar meridian. The black continuous line depicts the locus of the MIP during the CHACE observations.

2015).

To understand the sensitivity of the derived number density to such a difference, we have used two temperature models. One of them assumes 382 K at equator and 95 K at the pole, which is based on the Diviner observations, and used in this analysis. However, the previous reports from CHACE (*Sridharan et al.*, 2010*b*; *Thampi et al.*, 2015) used a slightly different temperature profile, with 400 K at equator and 150 K near the pole.

The Ar^{++}:Ar^{+} electron impact ionization cross section ratio of $\sim$0.087 at 70 eV is calculated from the single and double electron ionization cross section results reported by *Montanari and Miraglia* (2014). Several researchers have reported the experimental values of single and double electron impact ionization cross sections of Ar-40 over a range of electron energies which show good agreement with one another in the case of single ionization but show a factor of $\sim$2 dispersion in the range of 70-100 eV electron energy in case of double ionization cross section measurements (see Figs.2 and 3 in *Montanari and Miraglia* (2014) and the references therein). Considering the dispersion factor of $\sim$2 in the experimentally obtained double ionization cross section results, the ratio could be as high as $\sim$20%. Considering these dispersions, sensitivity analysis is carried out using the values of Ar^{++}:Ar^{+} ratio as 8.7% and 20%.

The two temperature models, with two different values of the electron impact ionization cross section ratios have been used to derive the surface number densities.

The top panel of the Fig.4.5 shows the two temperature models used for the sensitivity analysis. The temperature variation-1 (dashed line) and the temperature variation-2 (solid

line) assume 400 K at equator and 150 K at the pole. The bottom panel presents the results of the sensitivity analysis, as mentioned below.

1. Case-1: Temperature model-1 (382 K at equator and 95 K at pole) and Ar^{++}:Ar^{+} electron impact ionization cross section ratio 8.7:100
2. Case-2: Temperature model-1 (382 K at equator and 95 K at pole) and Ar^{++}:Ar^{+} electron impact ionization cross section ratio 20:100
3. Case-3: Temperature model-2 (400 K at equator and 150 K at pole) and Ar^{++}:Ar^{+} electron impact ionization cross section ratio 8.7:100
4. Case-4: Temperature model-2 (400 K at equator and 150 K at pole) and Ar^{++}:Ar^{+} electron impact ionization cross section ratio 20:100

The Neon number density is found to be more sensitive to the variation in the lunar surface temperature as it directly affects its velocity distribution. It may also be noted that the Ar^{++} contribution would be inherently high at the lower and middle lunar latitudes and hence the Neon number density is more affected by the Ar^{++} signature over those regions. However, near the poles, the temperature is so low that the ^{40}Ar undergoes condensation loss while Neon remains uncondensed. Hence, the effect of Ar^{++} contamination to the Neon in the measurements made by CHACE is not significant at higher lunar latitudes and near the poles.

CHACE observations have shown that the surface number density of Neon is higher at the colder regions near the pole as compared with the lower latitudes ($\sim 20°$S), consistent with the law of exospheric equilibrium for noncondensable gases (*Hodges and Johnson*, 1968).

Figure 4.6 shows the plot of the surface density (n) with respect to $T^{-5/2}$ and the best fit straight line has the R^2 value of 0.94. The surface number density (n) is seen to be related to the local surface temperature (T) as

$$n(T) = 2.5 \times 10^{9} T^{-5/2} + 2.1 \times 10^{3} \tag{4.1}$$

where n is in cm^{-3} and T is in Kelvin. This equation suggests that the surface number density of Neon is $\sim 2.7 \times 10^4$ cm^{-3} at midnight in low lunar latitudes where the temperature is $\sim$ 100 K, which is consistent with the NMS/LADEE-reported Neon concentration of $\sim 2\times 10^4$ cm^{-3} at local midnight in the low latitude region (*Benna et al.*, 2015).

Hence equation (4.1) can be used to obtain an expected Neon surface number density if measured temperature is available, like that provided by the Diviner (*Paige et al.*, 2010*b*).

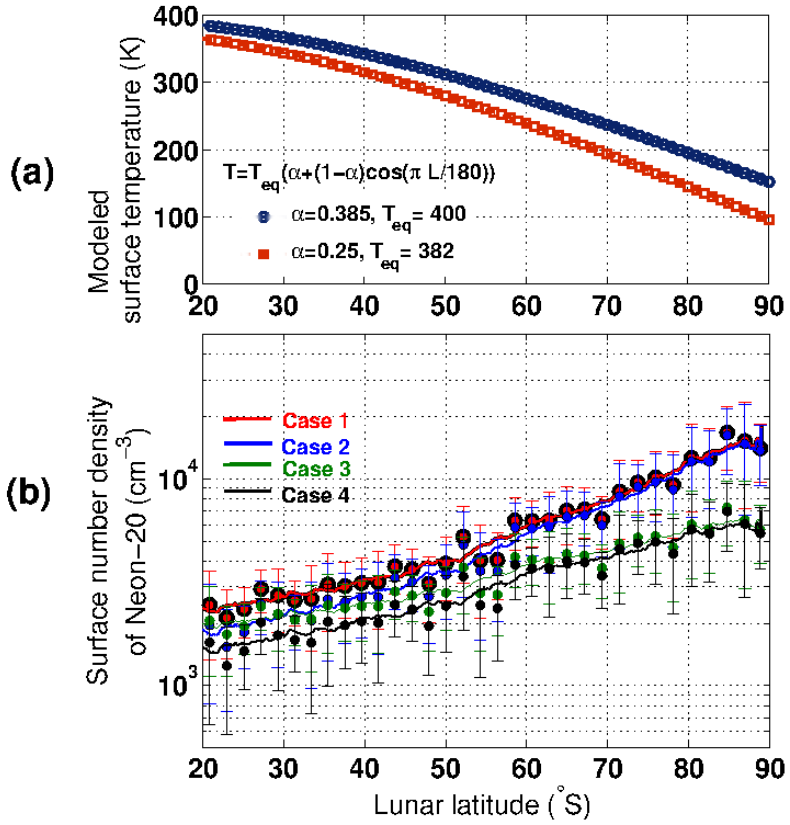

Figure 4.5: (a): Temperature profiles used for the sensitivity analysis of the derived number densities of Neon. The graph with blue circles represents the temperature profile from *Sridharan et al.* (2010*b*), while the one with red squares represent the tempretaure profile inferred from the Diviner observations. L represents the lunar latitude. (b): The result of the sensitivity analysis for four cases that include the combination of two temperature profiles and two different ratios of the double-to-single ionization cross section of ^{40}Ar. The latitude binning is same as that used in Fig. 4.3

It may be noted that this estimate would be valid in the absence of sinks, and that the constants of the equation (4.1) derived correspond to low solar activity conditions, without any CME events and based on the observations along a given longitude of 14°E, along the MIP trajectory.

4.4 Concluding remarks

The distribution of neutral Neon at the mid and high latitudes in the sunlit lunar exosphere observed by CHACE aboard the MIP of the Chandrayaan-1 is reported. The upper limites of the surface number density is found to vary from (7–22)$\times$ 10^3 cm^{-3} at the pole, to (3–5)$\times$ 10^3 cm^{-3} in mid (50°S) latitudes and to (0.5–1.1)$\times$ 10^3 cm^{-3} in lower (20°S) latitudes. The two dimensional map presented in Fig. 4.4 is characteristic to the LST

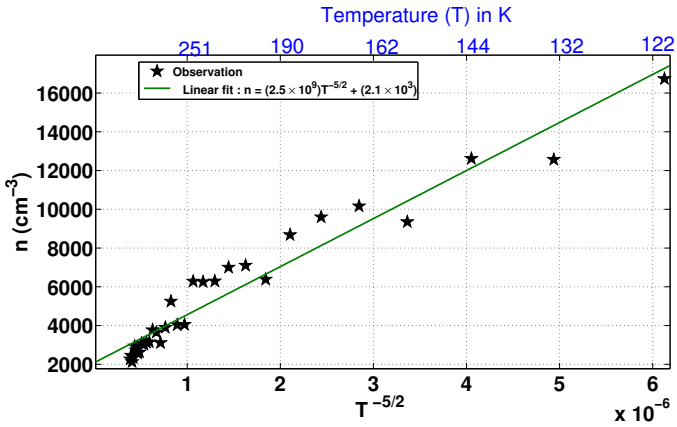

Figure 4.6: The variation of the Neon surface density n with respect to $T^{-5/2}$ for the lunar Neon at the middle and higher lunar latitudes.

of observation by CHACE ($\sim$14° E) and the meridional variation of the number density of Neon may be estimated to the first order by the law of exospheric equilibrium for noncondensable gases. The surface number densities estimated at lower latitudes from CHACE observations are consistent with the LADEE/NMS observations.

Chapter 5

Observation on Helium

Expect the best. Prepare for the worst. Capitalize on what comes.

—Zig Ziglar

5.1 The lunar Helium

Helium (He) is the lightest among the noble gases in the lunar neutral exosphere. The current understanding from the coordinated observations between NMS/LADEE, LRO/LAMP and ARTEMIS is that the source of lunar He is primarily (accounting for 64 ± 5 % of the total inventory) the solar wind alpha particles (He^{++}), while the rest is from endogenic sources owing to the radioactive decay of ^{232}Th and ^{238}U (*Hurley et al.*, 2016). Alpha particles from the solar wind get neutralized upon incidence on the lunar surface and constitute a majority of the lunar neutral Helium inventory (*Heiken et al.*, 1991; *Benna et al.*, 2015). In-situ (*Benna et al.*, 2015) and remote sensing (*Hurley et al.*, 2016) observations of the lunar Helium have shown a strong dependence of its abundance on the solar wind flux. The radiogenic Helium, on the other hand, constitutes a constant background of the lunar Helium. The latter is not expected to be affected by the fluctuations of the solar wind alpha particle flux (*Hodges*, 1975; *Benna et al.*, 2015). While the lunar disc is uniformly exposed to the He^{++} ions from the solar wind (except for the latitude-dependent surface obliquity and shielding by the minimagnetospheres, whereever present), the endogenic source of the lunar He is expected to show spatial heterogenity, as shown by the Thorium and Uranium maps reported from the Gamma Ray Spectrometer observations from Lunar Prospector (*Lawrence et al.*, 1999) and Kaguya (*Hasebe et al.*, 2009; *Kobayashi et al.*, 2010; *Yamashita et al.*, 2010) missions. The flux level of the endogenic component of the

lunar He is estimated to be $(4.5 \pm 1.2) \times 10^6$ He atoms cm^{-2} s^{-1} (*Grava et al.*, 2015*a*). Since He is non-condensable in the prevailing temperature and pressure conditions on the Moon, the Jean's escape is its primary loss process (*Hodges*, 1973), with a time constant of $\sim$ 5 days, as inferred from simultaneous multi-platform observations (*Benna et al.*, 2015; *Hurley et al.*, 2016).

Table 5.1 summarises the different loss processes of the lunar exospheric He and their relative importances. Figure 5.1 shows the schematic of different sources, sinks and processes in the lunar He exosphere.

Table 5.1: Loss processes of He in the lunar exosphere (from *Huebner et al.* (1992); *Stern* (1999); *Benna et al.* (2015))

Process	*Lifetime (Earth-days)*
Jeans escape	~ 5
Photo-ionization	200 (QS), 68 (AS)
Electron impact ionization	2.9×10^3

QS = Quiet Sun, AS = Active Sun

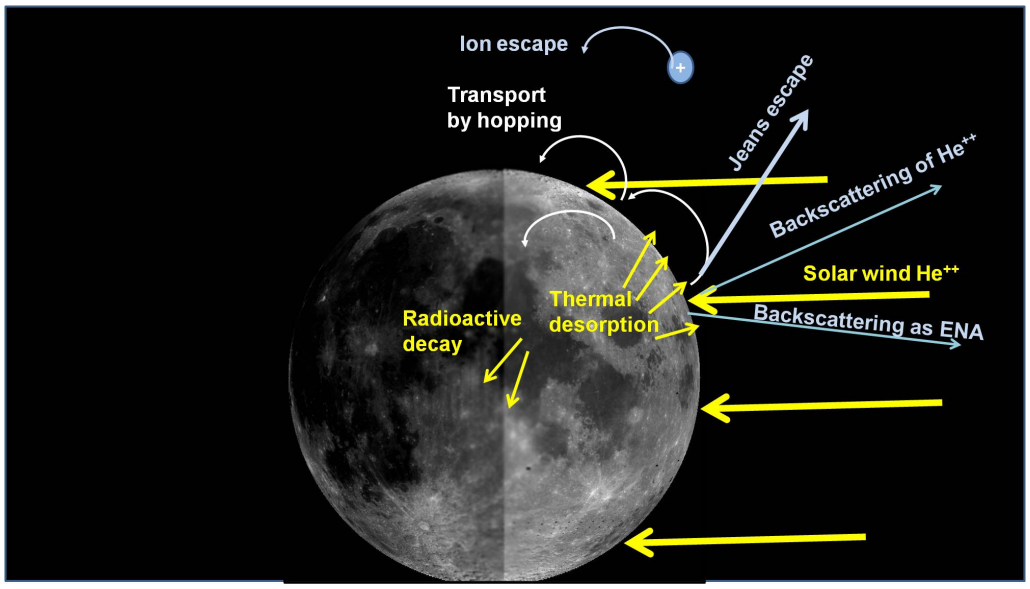

Figure 5.1: Schematic of the main processes acting on the lunar Neon exosphere.

Initially, in the absence of sufficient measurements, Monte Carlo simulations (*Hodges*, 1973), coupled with LACE results, indicated an upper limit of the daytime He abundance of 1.6×10^3 cm^{-3} for a solar wind alpha particle flux of 1.3×10^7 cm^{-2} s^{-1}. Model simulations based on exospheric model of *Hartle* (1971) further refined the upper limit to 1.2×10^3 cm^{-3} (*Hartle and Thomas*, 1974), for a solar wind alpha particle flux of 1.1×10^7

cm^{-2} s^{-1}. In his model, *Hodges* (1973) considered the fact that a non-escaping Helium atom may experience multiple hops before migrating to relatively colder regions. The horizontal extent of the trajectory of a hopping thermal Helium atom is a function of the zenith angle (χ) of its point of release (source point) from the surface and the ratio v/v_{esc}; where v and v_{esc} are respectively the initial velocity of the Helium atom released from the surface (which is, in turn, a function of the local surface temperature), and the escape velocity of the Moon (2.38 km s^{-1}). In his model, *Hodges* (1973) used the following formula to compute the horizontal angular extent (represented by δ; the angle subtended at the centre of the Moon by the source and impact points of the Helium atom on the lunar surface) of the trajectory of a hopping Helium atom.

$$cos\delta = 1 - \frac{8(v/v_{esc})^4 sin^2\chi cos^2\chi}{1 - 4(v/v_{esc})^2[1 - (v/v_{esc})^2]sin^2\chi} \tag{5.1}$$

The hop radius R_{hop} may be estimated from the relation

$$R_{hop} \; = \; R_{Moon}\delta \tag{5.2}$$

Here R_{Moon} is the radius of the Moon ($\sim$ 1735 km) and δ is in radians.

Simple analysis for a range of zenith angles and latitudes (and hence surface temperature T) shows that at lower latitudes the hop radius can be $(1 - 2) \times 10^3$ km, while in mid latitudes it can be $\sim 10^2$ km. Such a large hop length would average out the effect of the surface temperature gradient on the surface density of He.

Leblanc and Chaufray (2011) has further refined the Monte Carlo model of *Hodges* (1973) by incorporating the effect of the interaction between the hopping He atoms and the lunar surface. The He atom-lunar surface interaction is related to the time of residence of the He atoms in the surface (*Smith et al.*, 1978), calculated using the following equation (*Hunten et al.*, 1988).

$$\tau \; = \; \tau_0 \, exp\left(\frac{D_0}{kT}\right) \tag{5.3}$$

Here τ_0 is the vibration time for the van der Waals potential (4.7 $\times$ 10^{-13} s, after *Hunten et al.* (1988)), D_0 is the heat of adsorption, and T is the surface temperature. This results into typical residence time of 3 $\times$ 10^{-12} s in the nightside (*Leblanc and Chaufray*, 2011). The dayside residence time is calculated using equation 5.3 assuming the dayside surface temperature four times greater than that of the nightside surface temperature as 7.4 $\times$ 10^{-13} s.

The residence time of He on the surface influences the degree of their thermalization (*Leblanc and Chaufray*, 2011). The number of hops of a ballistic He atom on the sur-

face and its residence time determines its energetics. This is quantified with the enrgy accommodation factor, which is defined as the ratio of energy transfer between gas and surface to the energy which would have been transferred if the gas atoms had come into thermal equilibrium with the surface before re-emission (*Trilling*, 1970). It is given by α = $(E_2 - E_0)/(E_1 - E_0)$, where E_0, E_1 and E_2, respectively, represent the mean energies per atom of the 1) impacting species, 2) species in thermal equilibrium with the surface, and 3) species leaving the surface (*Shemansky and Broadfoot*, 1977). A low value of α, such as 0.05, corresponds to a single collision of the surface, while higher values (0.25 or more) suggest more than three collisions (*Shemansky and Broadfoot*, 1977; *Hunten et al.*, 1988). The limiting condition of $\alpha \rightarrow 1$ suggests complete thermalization of the atom with the surface. *Leblanc and Chaufray* (2011) found the best fit of the He data of LACE with α=0.75, which suggests that neither the full energy accommodation, as assumed by *Hodges* (1975) in his modelling, nor the low energy accommodation as assumed by *Shemansky and Broadfoot* (1977) were appropriate.

Hurley et al. (2016) has further improved the Monte Carlo model of the lunar Helium exosphere. Photoionization rate from *Huebner et al.* (1992) is used in the model for quiet Sun conditions. The model assumes that He is re-released immediately since the lunar surface temperature exceeds the sticking temperature and hops depending on its energetics. The model approximates the interaction of a He atom with the regolith grains leading to its thermalization by envisaging a thermalization coefficient (f_t), randomly chosen betwen 0 % and 100 %. The velocity (v) at which the He atom is released from the lunar surface to the exosphere is computed as a combination of the velocity with which the He atom had entered the regolith grains (ingoing velocity v_b) and a velocity picked up from the Maxwell-Boltzmann distribution at the local surface temperature. Assuming conservation of energy, the velocity of release of the He atom is computed as

$$v^2 = f_t v_t^2 + (1 - f_t) v_b^2 \tag{5.4}$$

The analytical model of the lunar surface temperature (*Hurley et al.*, 2015) obtained using the temperature map from the Diviner radiometer measurements (*Paige et al.*, 2010*b*) has gone into the Monte Carlo model to compute the Maxwell-Boltzmann velocity distribution function at a given point on the lunar surface.

The distribution of He on the lunar surface in the steady state is computed for a constant day-side He source of 4.7×10^{23} s^{-1} with the model. The model predicts that He surface density would peak at around 60-70° subsolar longitude. This apparently deviates from the temperature-dependent surface density predicted by the law of exospheric equilibrium for non-condensable gases (*Hodges and Johnson*, 1968). However, He being very light with large hop lengths, a large-area-averaged surface temperature is more relevant (*Benna et al.*, 2015).

The model predicts that the noon-time surface density of He to be $\sim 10^3$ cm^{-3} and has minimum latitudinal variation.

In last few decades, several missions have observed the lunar He exosphere, though in-situ as well as remote sensing techniques. These measurements have helped to constrain the model calculations. In the next section, the observations on the He exosphere will be presented.

5.2 Previous observations

Lunar He was first detected by the Lunar Atmospheric Composition Experiment (LACE) mass spectrometer (*Hoffman et al.*, 1973), emplaced on the lunar surface at 20°N latitude as a part of the Apollo-17 Lunar Surface Experiment Package. The diurnal variation of He revealed a maximum in density about 2 to 3 hours after the local midnight, with a value of (2–4) $\times$ 10^4 cm^{-3} (*Hodges*, 1975). Although LACE operated for nine lunations, the information on the daytime He was very limited, owing to low ($\sim 2 \times 10^3$ cm^{-3}) He density with large statistical fluctuations (*Hoffman et al.*, 1973).

The ultraviolet imaging spectrograph LAMP (Lyman Alpha Mapping Project) aboard the polar orbiting Lunar Reconnaissance Orbiter (LRO) detected He in the lunar exosphere using the 58.4 nm emission ($1s2p \rightarrow 1s^2$) line (*Stern et al.*, 2012), which is resonantly scattered by the Sun-illuminated He in the exosphere against the dark lunar surface at the dawn terminator. The results revealed hardly any latitudinal variation of the surface density of Helium (*Grava et al.*, 2016). LAMP inferred the Helium surface abundance to be maximum at local dawn with a number density of $\sim 2 \times 10^4\ cm^{-3}$ (*Feldman et al.*, 2012). It also revealed significant day-to-day variability, which was attributed to the variations in the solar wind flux. The absolute density also decreased by a factor of ~ 2 during each passage of the Moon through the Earth's magnetotail (*Feldman et al.*, 2012).

In addition, sporadic flares of He were observed by LAMP, which were attributed to strong bursts of alpha particles in the solar wind and this conjecture is supported by ARTEMIS observations (*Cook and Stern*, 2014). Another possible reason behind the observed sporadic increases of the lunar Helium is the sudden internal release from endogenic sources triggered by Moonquakes, which could be verified by simultaneous seismic measurements and remote sensing observations (*Cook and Stern*, 2014). By maneuvering the lateral roll and pitch of LRO towards and opposite to the direction of motion of the spacecraft, the line-of-sight illumination of LAMP was increased considerably, thus making reliable measurements possible (*Grava et al.*, 2016). The results suggested that instead of all the incident alpha particles getting thermalized, a significant fraction ($\sim$50%) of the incoming flux escapes as suprathermal Helium or by backscatter from the lunar surface. These conjectures were supported by the simultaneous observations by LAMP, NMS, and

ARTEMIS (*Hurley et al.*, 2016). It was inferred that about 60% of the solar wind alpha particles are converted to thermalized exospheric Helium through interaction with the lunar surface, while the rest may be reflected/scattered as He^{+} or He^{++}, or escape as energetic neutral atoms (ENA). In fact, Helium ENA has been observed by Chandrayaan-1 Energetic Neutral Analyzer (CENA), a sensor of the SARA experiment aboard Chandrayaan-1 (*Vorburger et al.*, 2014; *Bhardwaj et al.*, 2015), and has been understood as to be due to backscattering of the alpha particles after neutralization with a backscatter ratio of $(0.5 - 5) \times 10^{-3}$. This is considered to be a lower limit since the detection efficiency of CENA for He was less because of the higher ionization potential of He and it is estimated that the actual backscatter ratio could be 10 times higher (*Vorburger et al.*, 2014).

The NMS characterized the lunar neutral Helium over the equatorial latitudes ($\pm 23^{\circ}$) and reported the variability in terms of the diurnal cycle and also during the magnetospheric passages (*Benna et al.*, 2015). The He density has been observed to reach its maximum around 2 to 3 AM local time and to decrease by a factor of $\sim$2 during the magnetotail passage of the Moon. As mentioned earlier, increases in the He abundance are well correlated with solar particle events. NMS, however, did not report the day-side abundances of Helium due to the lower signal level and also the higher statistical noise in the data. In particular, no densities were reported between 1120 and 1400 LT. (*Benna et al.*, 2015).

The following section presents the in-situ observation of He in the sunlit lunar exosphere by CHACE.

5.3 Observations by CHACE

In most of the mass spectra acquired by CHACE, the amu-4 mass bin is found to be noisy, implying poor Signal-to-Noise Ratio (SNR). In majority of the spectra, He is not detected.

The apparent non-detection of He by CHACE could raise two concerns. Either, 1) the performance of the instrument in the lower mass range is below the expectations, because of the stringent requirement of high stability of the ion optics and mass filtering potentials; or, 2) the lunar exosphere had a density of He lower than the detection threshold of the instrument. The first possibility is ruled out by a careful check of the instrument House Keeping (HK) parameters, which were normal throughout the observation session. Also, the performance of CHACE was tested by inserting laboratory grade He during ground testing. This indicates that the He density in the sunlit lunar exosphere is indeed tenuous.

In order to recognize the feeble signatures of He amidst the system noise, the amu 4 mass bin in each mass spectrum has been scrutinized with a suitable pattern recognition based Peak Detection Algorithm (PDA).

The PDA takes 9 points in a given mass bin as input and checks for the pattern of

the rising and trailing edges characteristic to a peak. For a symmetrical peak with 9 samples with a reasonably good SNR, the fifth point should be the maximum, with all the four transitions at its left (right) are positive (negative). For a calibrated and tuned mass spectrometer like CHACE, any deviation from this is primarily due to the influence of random noise of comparable amplitude. The PDA used for the He peak detection looks for a minimum of 60% correct transitions (positive transition in the rising edge and negative transition in the trailing edge) and allows a shift of the maximum-valued sample by ± 1 point. The robustness of the PDA is tested with respect to false alarm probability with random noise, and is found to be 0.02 %. The PDA is applied to the data points in channels corresponding to amu 5 and 7 of all the 340 spectra, where neither any lunar species nor any spacecraft material is expected to contribute and hence would represent the system noise under actual operations that would limit the detection threshold. For both the channels the PDA test yielded no peak detection vindicating the robustness of the method. A detailed description of the PDA is presented in the next section.

5.4 The Peak Detection Algorithm

The DC and RF potentials applied at the Quadrupole Mass Analyzer (QMA) CHACE instrument are ramped so as to cover the mass range of 1 to 100 amu. The ramp-step of the Digital-to-Analog Converter (DAC) is equivalent to 0.11 amu. Hence, a bin of mass 1 amu is covered by 9 numbers of equispaced samples. As shown in Figure 5.2, the nine samples, denoted by x_1, x_2, ... x_9 constitute the mass bin.

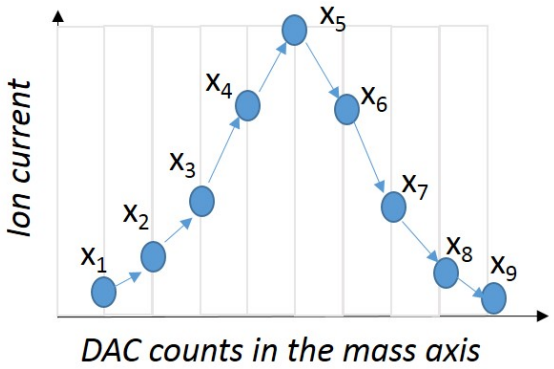

Figure 5.2: A typical mass peak in CHACE, comprising nine equispaced sample points, shown by x_i, where i=1,2,...9.

The detection threshold of a given species is dictated by the system noise of CHACE and the ionization cross section of the species. The system noise is contributed by the instabilities in the ion-optics and QMA potentials, thermal noise of the preamplifier and the associated circuit and the shot noise at the detector (*Dawson*, 1976).

If the number density of a given species is above the detection threshold of the mass spectrometer, a peak is registered in the corresponding mass bin. For a tuned mass spectrometer, the peak is ideal. That is, the peak is symmetrical, which, in turn, means that x_5 will have the maximum value and the elements in the rising edge, viz. x_1, x_2, x_3 and x_4 are in the increasing order of their respective values (i.e. positive transitions), while the elements in the falling edge, viz. x_6, x_7, x_8 and x_9 are in the decreasing order (i.e. negative transitions).

If the Signal-to-Noise-Ratio (SNR) is small, i.e. $\sim$1, the signal (peak) is contaminated with the noise, and hence, one or more of the following effects on the peak may be observed.

1. The maximum value of the peak may be shifted to left or right from the middle, i.e. x_5 no longer remains the maximum.
2. The increasing sequence of x_1, x_2, x_3 and x_4 is lost. There may be one or more wrong (decreasing) transitions due to the noise.
3. The decreasing sequence of x_6, x_7, x_8 and x_9 is lost. There may be one or more wrong (increasing) transitions due to the noise.

The PDA searches for the pattern of the ideal peak in the vector x_i = [x_1 x_2 x_3 x_4 x_5 x_6 x_7 x_8 x_9], with all the possible modes of distortion of the pattern as described above. The flow chart of the PDA is shown in Figure 5.3.

The PDA first checks the value of the index i, (say, k) for x_k = max(x_i). It allows for maximum one step of shift on either side, i.e. $4 \leq k \leq 6$. If this condition is not satisfied, the vector x_i is declared as 'not-a-peak'. If passed, then the vector is subjected to two more tests, which check in how many cases the required condition of positive transitions in the rising edge and negative transitions in the trailing edge are obeyed. In the PDA flow-chart shown in Figure 5.3, it is represented by the percentage of correct transitions in the left (rising) and right (trailing) edges, denoted by N_L and N_R, respectively. If any of these two conditions are not satisfied, the vector x_i is declared as 'not-a-peak'. In other words, in order to qualify as a possible peak, the maximum of the peak should not have a shift by more than one point on either sides and the number of correct transitions in the rising and trailing edges should be at least equal to a given percentage (N_L = N_R = $N_{L,R}$, say), which controls the stringency of the test.

Two possible errors in the PDA are:

1. Type-I error: Rejecting a true peak
2. Type-II error: Accepting a noise pattern as a peak (false detection)

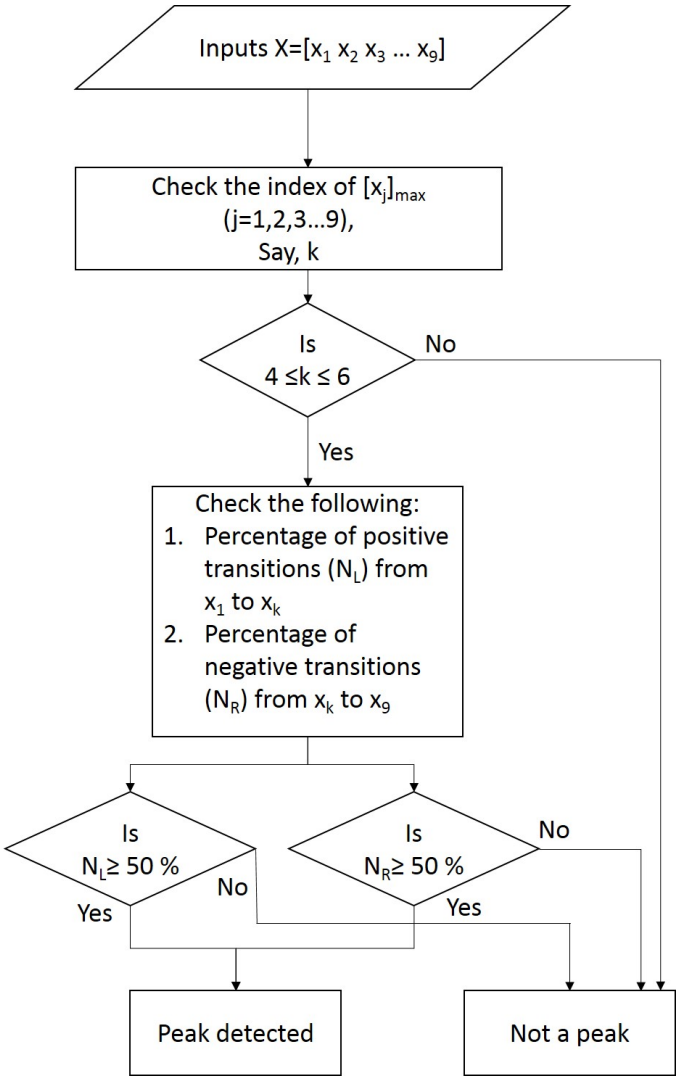

Figure 5.3: The flow chart of the PDA.

The type-I and II errors have the same significance as in the testing of a null hypothesis in statistics (*Goon et al.*, 1968). The PDA is tested for both kinds of errors. The probability of type-I error is tested by generating vectors with 9 elements by envisaging an ideal peak with 9 points and coherently adding a Gaussian noise with 9 points with its 3-σ value equal to the peak amplitude. The test is run for 10^7 times where the ideal peak is kept invariant while the noise pattern is changed from interation to iteration. On the other hand, for the type-II error test, Gaussian noise is generated and the PDA is run to check for any false detection. This test is also run for 10^7 times.

In the present application of the PDA to search for the pattern of the He peak with small SNR, the type-II error is more serious, which signifies false detection. For $N_{L,R}$=50%, the false detection probability is $\sim$ 2.7 %, while for $N_{L,R}$=60%, it is only $\sim$ 0.02 %. For the present analysis, $N_{L,R}$=60% is used.

5.5 Interpretation

As a next step, the points in the amu 4 mass bin from all the 340 mass spectra were subjected to the PDA. Out of all the trials, only 16 positive detections were encountered. Second order polynomials are fitted on the 9 points of the amu-4 mass bins that passed the PDA test and the peak amplitudes are determined. Barometric law is used to estimate the surface number density of He from the peak amplitudes, and are presented in Figure 5.4. It is observed that the inferred densities from the PDA-positive points are very close to the detection thresold of the instrument. Due to very less number of positive detections and poor SNR, in this paper we restrict ourselves to estimating the upper limit of He based on the detection thresold of the instrument.

Taking into account the instrument calibration factor from the detector current to the number density conversion using the total pressure measurement by the in-built Bayard-Alpert gauge of CHACE, and also accounting for the ram enhancement effect (*Sridharan et al.*, 2015), the detection threshold for N_2 gas in CHACE is $\sim 1.0 \times 10^2$ cm^{-3}. Accounting for the relative sensitivity of He to electron ionization at 70 eV with respect to N_2, which is 0.13 (*Summers*, 1969; *Holanda*, 1972), the detection threshold for He is $\sim 8 \times 10^2$ cm^{-3}. The uncertainty in the estimation of this value, accounting for the major contributors to the overall uncertainty, viz. the total pressure and relative partial pressure measurements, is $\pm 50\%$.

5.6 Discussion

Lunar He is known to have a uniform latitudinal distribution, as reported by LAMP in the terminator region (*Feldman et al.*, 2012; *Grava et al.*, 2016). This is attributed to the multiple hops undergone by the ballistic (Moon-bound) He atoms on the lunar surface (*Shemansky and Broadfoot*, 1977), resulting into uniform latitudinal distribution. The number of hops experienced by a ballistic He atom on the lunar surface determines the extent of its interaction with the lunar surface and the degree of thermalization.

As discussed earlier, the dynamics of this hopping process is described by the energy accommodation factor. Monte Carlo simulation by *Leblanc and Chaufray* (2011) brought out the sensitivity of the night-to-dayside density ratio of He to the energy accommodation factor. In the present work, the energy accommodation factor is estimated with the upper limit of $\sim 8 \times 10^2$ cm^{-3} of the dayside He density reported here, and the nightside maximum density of $\sim 7 \times 10^4$ cm^{-3} observed by NMS when the Moon was outside the Earth's magnetotail, during a coronal mass ejection (CME) (*Benna et al.*, 2015). The maximum night-time density reported by *Benna et al.* (2015) is scaled down by a factor of $\sim$3.6 (to normalize the state of the solar wind alpha particle flux during the reported

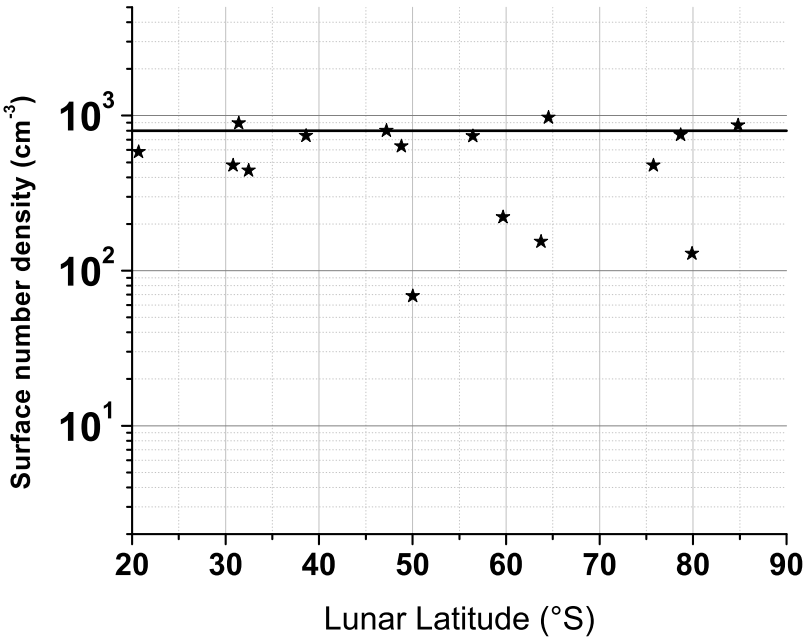

Figure 5.4: The inferred surface density of He corresponding to the PDA-positive points, detected based on pattern recognition. The dark horizontal line indicates the detection thresold of the instrument, limited by the system noise.

NMS observation to that during the CHACE observations, using SWEEPAM/ACE data) and a factor of $\sim$2 (to normalize the state of the lunar exosphere to that during magnetotail passage). This yields a minimum night-to-dayside density ratio of $\sim$ 12, which, according to *Leblanc and Chaufray* (2011), corresponds to the energy accommodation factor of at least 0.35 for He atoms with Maxwell Boltzmann (MB) energy distribution. This indicates four or more hops by a ballistic He on the lunar surface.

The significantly less number of the PDA detections of He by CHACE is attributed to the very special conditions at which CHACE measurements were carried out in the lunar exosphere. The major factors that control the abundance of He in the lunar exosphere are:

1. Local Solar Time: Helium density maximizes after local midnight and is minimum during lunar day (*Hodges*, 1975; *Benna et al.*, 2015; *Hurley et al.*, 2016).

2. Location of the Moon with respect to the Earth: He density minimizes when the Moon is about to exit the Earth's magnetotail, during its orbit around the Earth (*Benna et al.*, 2015).

3. The flux level of the solar wind alpha particles: Since the majority of the lunar He is of the solar wind origin, the lunar He is known to scale with the solar wind alpha particle flux (*Hurley et al.*, 2016).

When it comes to the loss processes, the Lunar He is sensitive to Jeans escape because of its small escape parameter, which is the ratio of its gravitational binding energy to thermal energy (computed as ∼3.47 at 390 K surface temperature). Because of its low mass, it has a large scale height (∼400 km at 390 K surface temperature, which is typical during lunar day). Thus, during a lunar day, the insolation at lower latitudes is enough to cause thermal expansion of the He exosphere so as to reduce the surface density. Apart from the He atoms that undergo Jeans escape, the ballistic component of He has a large hop length, often in the order of half to one third of the lunar radius at lower latitudes in the sunlit side (*Hodges*, 1973; *Leblanc and Chaufray*, 2011).

In addition to the diurnal variability, lunar He is also sensitive to the location of the Moon with respect to the Earth. When the Moon enters the Earth's magnetotail where it spends ∼ 4–5 days, it is shielded from the solar wind influx. Thus, the loss of the lunar He, which is mostly by Jeans escape with a time constant of ∼4.5 days (*Benna et al.*, 2015), is not replenished during the passage of the Moon through the Earth's magnetotail, resulting in the monotonic decrease of the lunar He abundance.

Since the lunar Helium owes its origin to the solar wind, the absolute values of its surface density at any given local time depends on the prevailing solar wind alpha particle flux. The above inference is substantiated by the measurements of NMS/LADEE during several lunations and it is observed that lunar He inventory hits its minimum when the Moon is about to come out of the Earth's magnetotail (*Benna et al.*, 2015).

Figure 5.5 shows the monthly averaged solar wind alpha particle flux from year 2008 to 2015, as derived from the SWEEPAM/ACE observations. The time range covers the observation time of CHACE/Chandrayaan-1 and NMS/LADEE. During NMS observations, there have been several occasions of solar flares, which caused increase in the level of the solar wind alpha particle flux. On the other hand, it is observed that during the CHACE observations, the solar wind alpha particle flux was less by a factor of ∼ 3.6 than during February 2014, when the NMS observed the maximum He density.

Further, the CHACE observations were carried out in the lunar dayside, when the Moon was on the verge of coming out of the Earth's magnetotail, as shown in Figure 2.24. A combination of these conditions, along with the low solar wind alpha particle flux at the time of CHACE observations present a case when the He abundance in the Moon had been at its lowest. CHACE has thus studied the lunar exosphere in an extreme condition of the factors that control the lunar He abundance.

5.7 Conclusion

An upper limit of $\sim 8.0 \times 10^2$ cm^{-3} for the surface density of the neutral He in the sunlit lunar exosphere is proposed based on the observations made by CHACE/MIP/Chandrayaan-

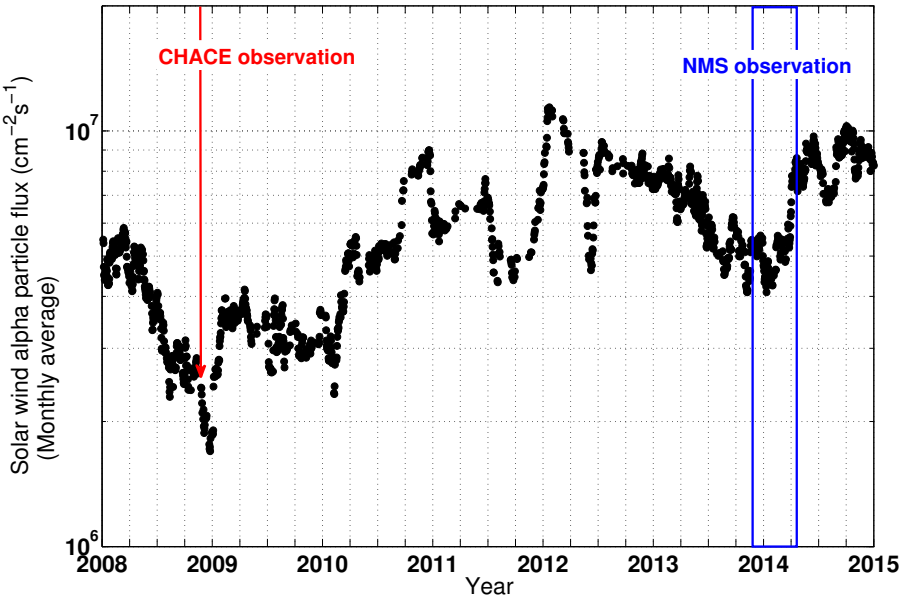

Figure 5.5: Monthly averaged solar wind alpha particle flux, as derived from the SWEEPAM/ACE observations over few years, covering the observation time of CHACE/Chandrayaan-1 and NMS/LADEE. Alpha particle number density data along with the velocity data of protons are used to compute the alpha particle flux. It is observed that during the CHACE observations, the solar wind alpha particle flux was significantly less than that during the NMS/LADEE observations.

1. However, more sensitive measurements are called for to throw more light on this aspect. The CHACE observations were carried out in the lunar dayside, when the non-escaping component of the lunar He exosphere thermally expands, thereby reducing its surface number density. Furthermore, during CHACE observations, the Moon was about to exit the Earth's magnetotail and thus had been deprived of the fresh influx of the solar wind alpha particles. In addition, the then prevailing low level of the solar wind alpha particle flux present a case where the He abundance in the Moon had hit one of its lowest values.

Thus, CHACE has observed the lunar exosphere in an extreme condition, where all the major factors controlling the lunar He inventory were unfavourable, and, therefore, provides a constraint to the lunar He exosphere models under such extreme conditions.

Chapter 6

Observations on H_2

A scientist in his laboratory is not only a technician, he is also a child placed before the natural phenomena which impress him like a fairy tale.

—Marie Curie

6.1 The lunar H_2

Study of the distribution of H_2 is considered to be an important tool to study the exosphere-surface interaction in the Moon. The major source of the Lunar exospheric H_2 is the solar wind proton flux (*Hodges et al.*, 1972). In steady state, a balance exists between the influx of the solar wind protons and the outflux of hydrogen. At energies of $\sim$ 1 keV amu^{-1}, solar wind protons penetrate few 10s of nm into the rim of the regolith grain and most of them are neutralised (*Hurley et al.*, 2017). The Kaguya mission has measured that a small fraction ($\sim$ 0.1 to 1 %) of the solar wind protons are backscattered from the surface as ions (*Saito et al.*, 2008). This has been confirmed by the ARTEMIS spacecraft (*Halekas et al.*, 2013). The SARA instrument of Chandrayaan-1 (*Wieser et al.*, 2009) and the Interstellar Boundary Explorer (IBEX) (*McComas et al.*, 2009; *Funsten et al.*, 2013; *Allegrini et al.*, 2013) have shown that about 10 to 20 % of the incident solar wind protons are converted to Energetic Neutral Atoms (ENA). Thus, about 10 to 20 % of the incident solar wind proton flux is directly accounted as H^+ ions and ENAs, leaving the rest 80 to 90 % unobserved (*Hurley et al.*, 2017).

It is proposed (*Crider and Vondrak*, 2002) that H_2 is produced from the interaction of the solar wind with the regolith through chemical sputtering. Further, *Hurley et al.* (2017) has quantified this process as 10 % of the solar wind H^+ requires to be converted to H_2,

for a density of $\sim$ 1200 cm^{-3} of the latter. The chemically sputtered H_2 molecules are released from the surface with a lower energy and hence remain in the lunar exosphere over several hops. On the other hand, the process of physical sputtering is not very significant as a potential source of the lunar H_2 since it releases H_2 with higher energy resulting into higher scale height and escape fraction (*Hurley et al.*, 2017).

Apart from the chemical sputtering of the solar wind protons on the lunar regolith which produces a symmetrical H_2 density about the subsolar point, *Hurley et al.* (2017) has also considered the role of micrometeorides as a source of the lunar H_2. Micrometerorides are likely to produce a dawn-dusk asymmetry in the H_2 density, as the dawn hemisphere of the Moon experiences greater influx of the micrometeoroids than the dusk hemisphere owing to the motion of the Earth-Moon system around the Sun (*Fechtig et al.*, 1974). This is confirmed by the Lunar Dust Experiment (LDEX) aboard the LADEE spacecraft (*Horányi et al.*, 2015). However, direct delivery of H_2 via micrometeoroids is not a very efficient source, even if the micrometeoroid is composed entirely of water (*Hurley et al.*, 2017) as they are not likely to carry large amounts of hydrogen. Thus, the solar wind proton flux remains as the potential source of the lunar exospheric H_2.

Table 6.1 summarises the different loss processes of the lunar exospheric H_2 and their relative importances. Figure 6.1 shows the major source and sink processes of the lunar H_2.

Table 6.1: Loss processes of H_2 in the lunar exosphere (*Benna et al.*, 2015; *Huebner et al.*, 1992)

Process	*Lifetime*
Jeans escape	2.2 days [a]
Photo-ionization	214 days (QS)[b] and 100 days (AS)[b]

[a] Scaled down the Jeans escape time constant of He-4 (*Benna et al.*, 2015) by a factor of 2.

[b] Photoionization lifetimes are computed based on the photoionization rates provided by *Huebner and Mukherjee* (2015). QS and AS refer to quiet Sun and active Sun respectively.

6.2 Previous observations

The results from the in-situ obervations made by the LACE instrument in the Apollo-17 Surface Experiment Package suggested the presence of molecular Hydrogen in the lunar atmosphere, which owe its origin to the lunar surface (*Hoffman et al.*, 1973). The LACE had measured a H_2 surface density of 6.5 $\times$ 10^4 cm^{-3} at night, which agreed with the prediction (*Hodges*, 1973).

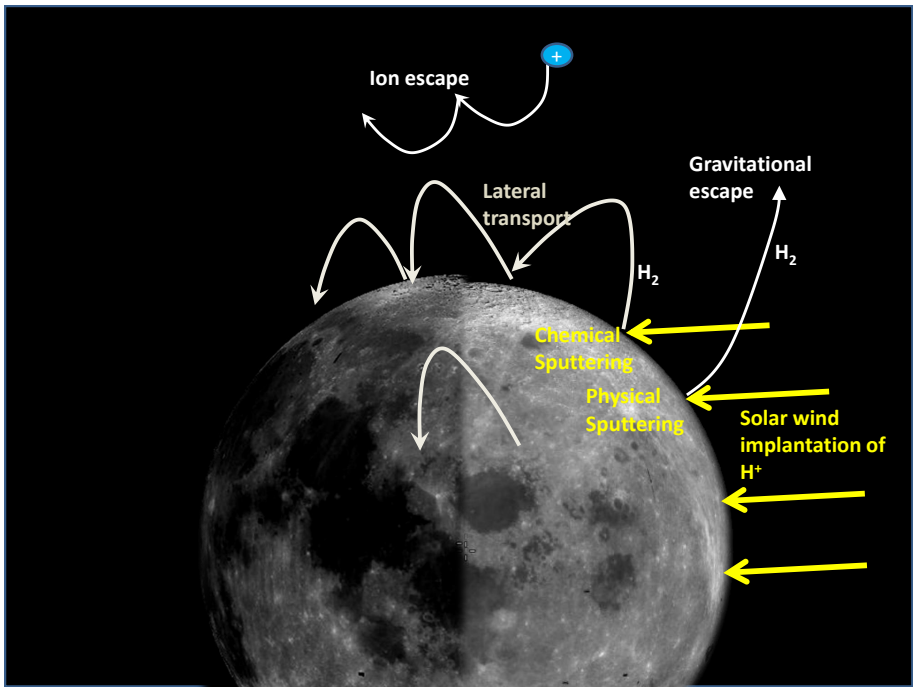

Figure 6.1: Cartoon showing the major source and sink processes of the lunar H_2, based on the discussions given in (*Hurley et al.*, 2017). The major source of the lunar H_2 is the chemical sputtering from the lunar regilith, which owes its hydrogen inventory to the solar wind proton influx. The physically sputtered component of the H_2 from the lunar regolith usually has enough energy to escape the lunar gravity. In the cartoon, both the thermal escape and physical sputtering-induced escape components of the lunar H_2 are shown as gravitational escape. Another escape mechanism is the ion escape, collectively due to photoionization, charge exchange and electron impact ionization.

Apart from LACE, the UV spectrometer aboard the Apollo 17 orbiter also detected similar levels of H_2 ($\sim 10^4$ cm^{-3}). On the other hand, the estimated atomic Hydrogen abundance was too low, i.e., $\sim$10 cm^{-3} (*Fastie et al.*, 1973). This was interpreted as an indication for the conversion of the majority of the solar wind protons as H_2 at the lunar surface and its re–emission to the atmosphere in accordance with the lunar surface temperature. The upper limits of H_2 at the Apollo–17 site *Hodges et al.* (1974) also qualitatively agreed with this hypothesis. Later, using the Apollo–17 UV spectrometer data, *Feldman and Morrison* (1991), provided more stringent upper limits to the number densities of H (17 cm^{-3}), and H_2 (9000 cm^{-3}). On the other hand, *Wurz et al.* (2012), based on the previously reported upper limits, arrived at H_2 number density of 5×10^4 cm^{-3} near 10 km above the lunar surface on the dayside, at a temperature of 400 K.

Lunar H_2 was also detected by the LAMP UV spectrometer aboard the LRO spacecraft in the vapour plume emanated from the impact of the LCROSS into the permanently shadowed Cabeus crater (*Gladstone et al.*, 2010*b*). A release of about 110 kg of H_2 was estimated (*Hurley et al.*, 2012). LAMP also derived a H_2 surface density of $1.7 \pm 0.4 \times 10^3$ cm^{-3} at dusk increasing to $2.1 \pm 0.3 \times 10^3$ cm^{-3} at dawn (*Cook et al.*, 2013). Using the same dataset, averaging many different column lengths throughout the mission, *Stern*

et al. (2013) obtained an effective vertical column density of $\sim 6 \times 10^9$ cm^{-2}, which translated to a surface density of $\sim 1.2 \times 10^3$ cm^{-3}, at 120 K.

The Chinese lunar mission Chang'E-1 flew Electro Static Analysers (ESA), which revealed parallel curve structures in the energy-time spectrogram with a component due to a flux of ions with energy ~ 8 times greater than the solaw wind proton energy (*Wang et al.*, 2011). The ions exhibited ring-distribution in the V_E-V_C space, where V_E and V_C are respectively the velocity components parallel to the Interplanetary Magnetic Field (IMF) and perpendicular to the local IMF direction. The ring distribution, along with the $\sim 90^\circ$ pitch angle indicated their 'pick-up'origin. The low initial velocity of these pick-up ions (with m/q = 2, which could either be H_2^+ or He^{++}), derived from the velocity-space distribution confirmed their cold source origin, including the Local Inter Stellar Medium (LISM), Inter Planetary Dust (IPD) or the neutral exosphere of the Moon. Based on their observed flux level, the LISM and IPD sources of the pick-up ions were ruled out and lunar neutral exosphere was confirmed as the source. Further, based on the comparison between the observed flux of the ions and the possible H_2^+ or He^{++} flux levels estimated based on the production rates of H_2^+ and He^{++}, it was inferred that the observed pick-up ions were H_2^+, which originated from the ionizing processes like photoionization, charge exchange, electron impact ionization, etc. of the lunar neutral H_2. This was the first observation of the lunar pick-up H_2^+ ions, and indirect evidence for the lunar neutral H_2 exosphere.

Recently, *Halekas et al.* (2015) has inferred the neutral H_2 density from the measurement of H_2^+ ions by the NMS instrument in its ion mode. However, the NMS ion observations are convolution of the ionization production process and the column density along the electric field direction.

6.3 Results of CHACE observations

The CHACE instrument aboard the MIP conducted in-situ measurements of the lunar H_2 from 100 km altitude to the surface at different latitudes along the 14° E meridian. The in-situ obervations were convolution of altitude and latitude (refer Figure 6.2). Barometric law is used to translate the measured partial pressure of H_2 to the surface density using the local surface temperature and scale height. A 2D (latitude versus altitude) map of the lunar H_2 is generated along the 14° meridian, as shown in Figure 6.3.

The map clearly shows the increased abundance of H_2 near the polar region. As expected, the H_2 number density do not show any significant altitude variation due to its scale height being larger than 100 km, even at 88°S and even when the temperature is low. The derived values of the surface number density of H_2 agree with the values reported by *Stern et al.* (2013) wherein they had estimated a surface density of$\sim 10^3$ cm^{-3} for H_2 corresponding to a surface with a temperature of 120 K, and the present estimates for

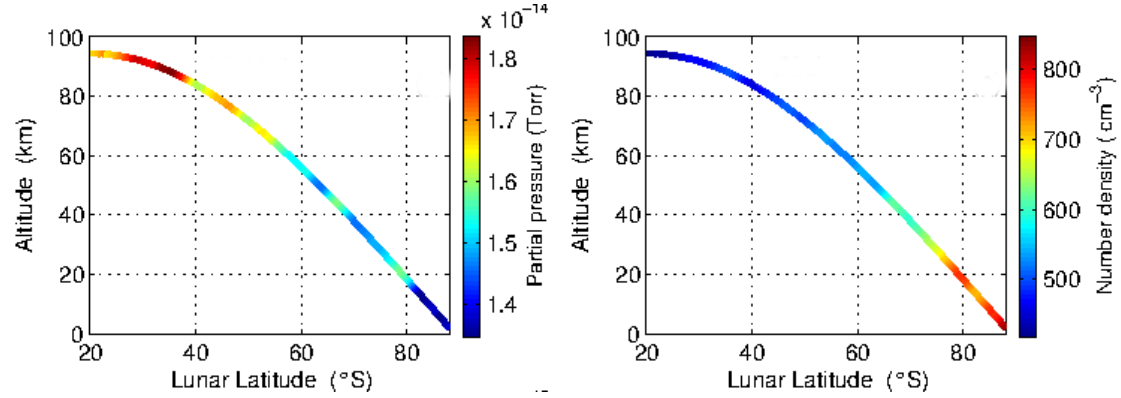

Figure 6.2: Left: The observed partial pressure of H_2 along the MIP trajectory. Right: The calculated number density of H_2 along the MIP trajectory.

the surface density at 88°N (∼140 K) is ∼825 cm^{-3}. However, it should also be noted that our estimates are significantly lower than the upper limit reported by *Cook et al.* (2013).

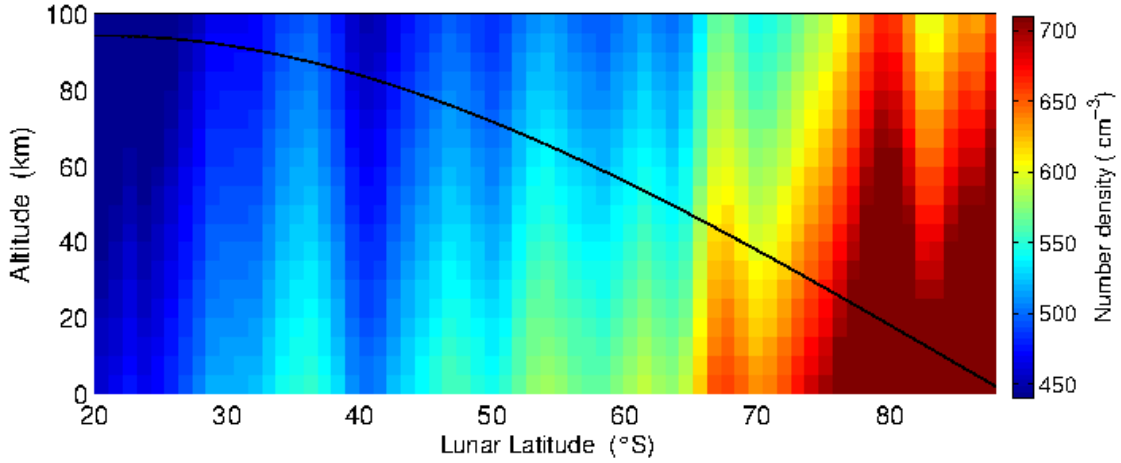

Figure 6.3: A two dimensional (latitude vs altitude) map of H_2 generated using the scale heights at different latitudes. The black continuous line depicts the locus of the MIP during the CHACE observations.

Further, the CHACE measurements reveal significant latitudinal variation which is an indication of the spatial heterogeneity of the lunar H_2. Until now no such information is available since all the previous estimates were based either, on single point measurements or, on highly averaged UV spectra/calculations based on night time measurements. If the latitudinal variation of H_2 had been only due to surface temperature variation, then it should have been rather smooth and the density should have monotonically increased with latitude. On the other hand, distinct undulations are observed in the spatial variation of H_2 number density despite its large scale height.

The surface number density of H_2 derived from the in-situ observations by CHACE is correlated with the surface topography along the 14° E meridian. The surface topog-

raphy data are obtained from the Lunar Laser Ranging Instrument (LLRI) aboard the Chandrayaan-1 orbiter. It is observed that over the craters where the surface is ∼2 km below the mean level, the H_2 concentration is slightly less compared to the nearby elevated regions. Similarly, the H_2 concentration is relatively higher near the elevated region ∼80°N as compared to the region northward of it. This is shown in Figure 6.4.

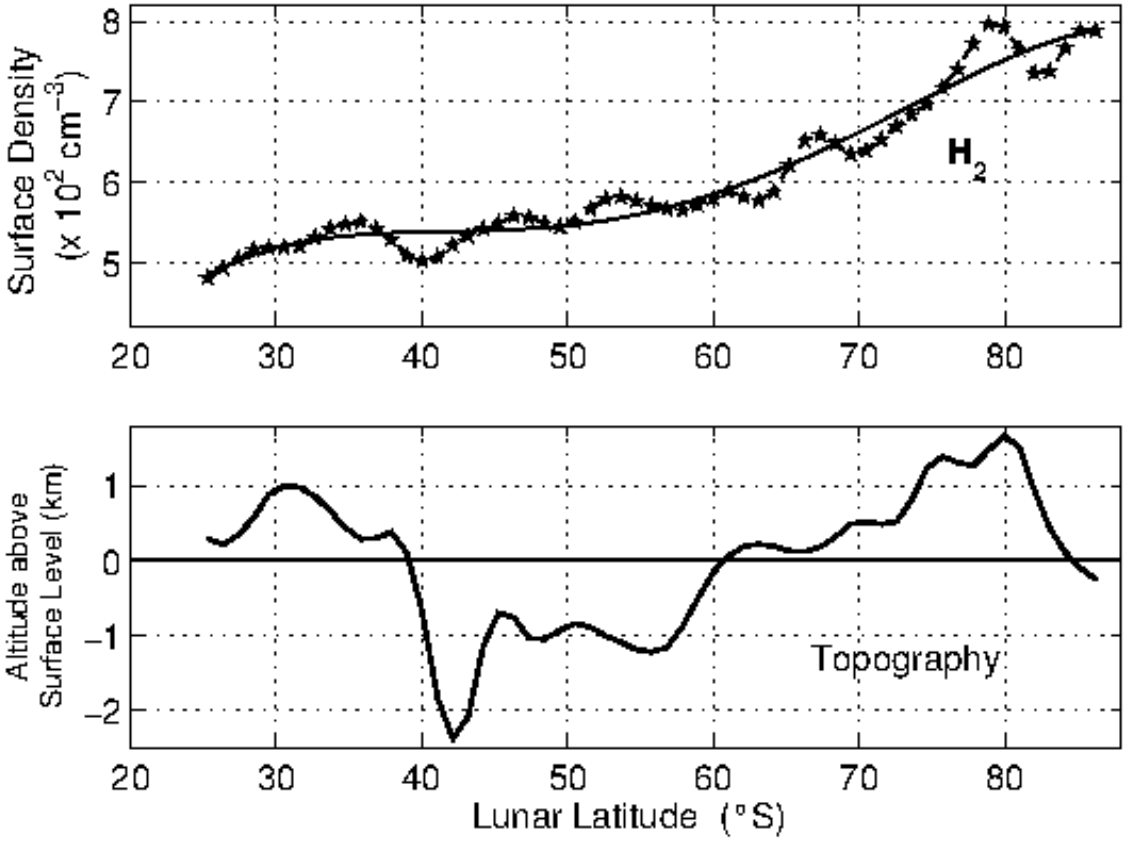

Figure 6.4: Variation of the surface number density of H_2 (top panel) and the surface topography (bottom panel) at different lunar latitudes along the MIP ground trace.

Theoretical calculations have shown that 60% of the H atoms form H_2 through chemical sputtering (*Crider and Vondrak*, 2002). The Apollo-16 and 17 soil sample studies suggested that the Hydrogen abundance in the soil increases as a function of depth (*Gibson and Bustin*, 1987). The lunar H_2 may get released due to a variety of surface processes including the solar wind interaction with the Hydrogen bearing compounds like water ice and also cometary impacts. This may provide a clue to the origin and spatial distribution of the exospheric H_2 and the plausible role of large scale processes that had led to the present day topographical features. It must also be remembered that H-bearing compounds like water ice are more concentrated in the polar regions, thus increasing the probability of finding more Hydrogen over there. The recent observations using the LRO neutron detector experiment showed increased Hydrogen abundance in the regolith over the South Pole region, but those regions are not spatially coincident with the permanently shadowed

craters (*Mitrofanov et al.*, 2010). More such measurements are needed to unravel the complexities of the lunar atmosphere.

6.4 Concluding remarks

The CHACE experiment on the MIP enabled us to obtain the distribution of the lunar H_2 during daytime along the 14° E meridian. A remarkable feature observed was the spatial heterogenity of the lunar H_2 number density. The H_2 density showed enhancement in the elevated regions, despite the fact that the scale height of H_2 is vergy large ($\sim$ 700 km at 400 K) compared to the scale of orographic variations on Moon. These results highlight the complexities of the lunar atmosphere and the significant role of the lunar surface processes in modulating the distribution of the different species.

Chapter 7

Summary and Future Work

The more you lose yourself in something bigger than yourself, the more energy you will have.

—Norman Vincent Peale

7.1 Summary of the Work and Major Results

The present thesis is the outcome of the scientific investigation of the lunar exospheric ^{40}Ar, ^{20}Ne, ^{4}He and H_2, based on the in-situ observations made by the CHACE payload aboard the MIP in Chandrayaan-1 mission. This is the first, and so far the only observation on the latitudinal and altitudinal distribution of the lunar exospheric noble gases covering mid and high latitudes and the southern polar region, under sunlit condition.

The distribution of ^{40}Ar at the mid and high latitudes in the sunlit lunar exosphere is investigated. ^{40}Ar density is seen to be maximum between 30° and 50°S with a value of $\sim 4\times 10^4$ cm^{-3}. The upper limits of the surface number density decreases at higher latitudes and near the polar region it is found to be $\sim 1\times 10^4$ cm^{-3}. The ^{40}Ar:^{36}Ar ratio along the 14°E meridian is found to be $\sim$ 1 in the Northern hemisphere and $\sim$ 2.5 in the Southern hemisphere. An altitude versus latitude map of the lunar ^{40}Ar along the above-mentioned meridian is also presented. The relation between the topography and the ^{40}Ar concentration is delineated and the indications on the spatial heterogeneity of the radiogenic processes are brought out. It is observed that the ^{40}Ar density enhances near the crater regions.

For ^{20}Ne, it is found that the upper limit of the surface number density varies from (7–22)$\times$ 10^3 cm^{-3} at the pole, to (3–5)$\times$ 10^3 cm^{-3} in mid (50°S) latitudes and to (0.5–1.1)$\times$ 10^3 cm^{-3} in lower (20°S) latitudes. An empirical relation between the lunar ^{20}Ne

surface density and surface temperature based on the law of exospheric equilibrium for non-condensable gases is proposed. Although derived under the conditions of the sunlit exosphere, it provides a first order estimate on the surface density of ^{20}Ne, given the surface temperature.

A combination of daytime He-4 depletion and decrease during magnetotail passage of the Moon, along with low flux of alpha particles in the solar wind at the time of CHACE observations presented a unique case when the He-4 abundance in the Moon had hit one of its lowest values. CHACE, thus had the opportunity to explore the lunar exosphere in an extreme combination of the factors that control the lunar He abundance. Based on the observations and instrument sensitivity, an upper limit of $\sim 8.0 \times 10^2$ cm^{-3} for the surface density of lunar He-4 in the sunlit hemisphere is proposed. This result is expected to provide realistic constraints to the lunar He exosphere models under similar extreme conditions.

The analysis of the H_2 distribution at the mid and high latitudes in the sunlit lunar exosphere is also reported. Lunar H_2 is seen to maximize at the higher latitudes. The estimated number density in the high southern latitude during the lunar day is found to be ~ 825 cm^{-3}. A remarkable feature observed was the spatial heterogenity of the lunar H_2 number density. The H_2 density is found to show enhancement in the elevated regions. These results highlight the complexities of the lunar atmosphere and the significant role of the lunar surface processes in modulating the distribution of the different species.

The incremental knowledge on the lunar science added by this research includes:

1. Two dimensional (latitude versus altitude) distribution of lunar exospheric Ar, Ne and H_2 based on direct (in-situ) observations covering a range of latitude and altitude.

2. Results on the spatial heterogenity and indications of interhemispherical asymmetry of radiogenic activity in the lunar interior through the measurement of the ^{40}Ar:^{36}Ar ratio.

3. Empirical formula connecting the surface number density (n) of lunar Ne and the surface temperature (T)

4. Upper limit of the He density under extreme conditions of the major controlling factors: i.e. when the lunar exosphere is sunlit, the Moon is on the verge of coming out of the Earth's magnetotail, and the solar wind proton flux level is low.

Figure 7.1 summarizes the latitudinal variation of the surface density of ^{40}Ar, ^{20}Ne and H_2, as derived from the CHACE observations. ^{40}Ar is seen to maximize in the mid latitudes and decrease in the high latitudes because of its condensable behaviour. On the other hand, surface density of ^{20}Ne and H_2 increase at higher latitudes due to their non-condensable

nature. The slope of the surface density of H_2 is found to be less, as it is a light species and has large hop lengths and hence not affected by local temperature variations.

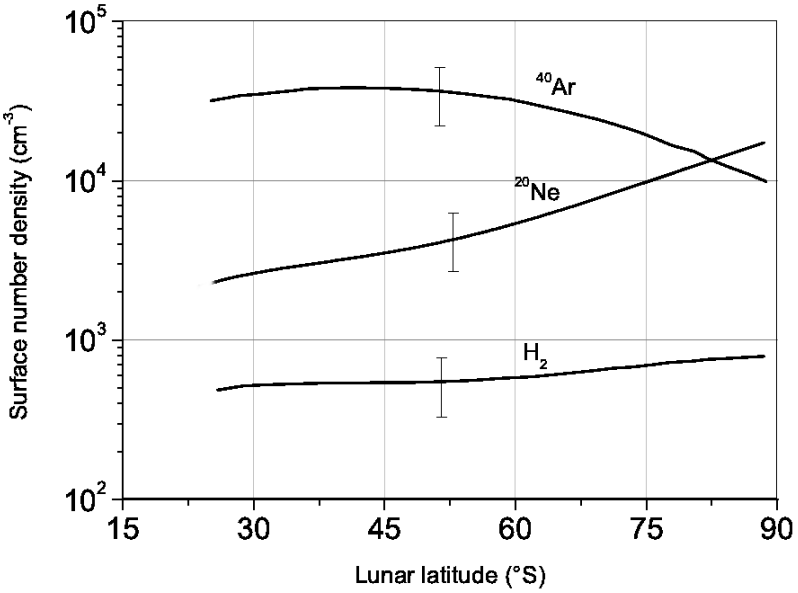

Figure 7.1: Latitudinal variation of the surface density of ^{40}Ar, ^{20}Ne and H_2, as derived from the CHACE observations. Fourth order polynomials are plotted in order to emphasize the latitudinal variation of the surface densities of these species thereby suppressing the local variations.

7.2 Open Questions

The scientific outcome of this research, based on the observations by CHACE, on the latitudinal and altitudinal variation of the noble gases on the lunar exosphere facilitated the understanding of the source and sink processes of the lunar exosphere, surface-exosphere interaction and the dynamics of the exospheric species.

The polar exosphere of the Moon remain inadequately explored. For instance, The Moon's South Pole-Aitken Basin, one of the largest impact structures known within the Solar System, exposes material from deep within the crust and possibly even the upper mantle that was excavated by the impact, and may preserve melt rocks from the impact itself. The permenantly shadowed regions of the Moon shows signatures of the presence of Hydrogen bearing compounds (*Pieters et al.*, 2009). All these reiterate the importance of having a polar orbiting satellite equipped with composition measurements of the lunar exosphere, which is directly coupled to the lunar surface. CHACE aboard MIP in Chandrayaan-1 was a one-time experiment. The spatial heterogenity observed in the variation of several species from the CHACE results calls for more observations, both in space and time. This can be accomplished by in situ measurements from a polar satellite

platform. The CHACE-2 (CHandra's Atmospheric Composition Explorer-2) experiment aboard Chandrayaan-2 mission is going to fullfil this important requirement.

7.3 Future work: Detailed observation of the lunar exosphere

The lunar exosphere will be studied in more details in the Chandrayaan-2 mission. The Chandrayaan-2 will consist of an orbiter, lander and a rover. The Chandra's Atmospheric Composition Explorer (CHACE-2) will be a payload aboard the Chandrayaan-2 orbiter, which will study the lunar exosphere from 100 km circular polar orbit. The CHACE-2 instrument will be fundamentally similar to CHACE aboard MIP/Chandrayaan-1, but with important functional differences (mass range, multi-mode operation, telecommand capability, etc.) that will facilitate detailed study of the lunar neutral exosphere.

The selection of the operating parameters and configurations of the CHACE-2 instrument are guided by the experiences gained in the CHACE observations. While the mandate of CHACE was to study the lunar neutral exosphere till the surface of the Moon , it was a one-time experiment and hence was operated in a given configuration of instrument parameters. On the other hand, the CHACE-2 instrument will be housed in the Chandrayaan-2 orbiter and hence, multiple operating configurations are being worked out based on scientific requirements. The different operating configurations and telecommand-amenability of CHACE-2 will allow the instrument to choose the mass range of operation, scan rate, electron energy for impact ionization, ion optics parameters, etc..

The CHACE-2 experiment will provide new insights about the lunar exosphere, especially over the least explored polar and high latitude regions and may provide answers to many questions that are open today.

Appendices

Appendix A

Vertical density profile in an exosphere

The following sections present a discussion on the applicability of the barometric law to derive the vertical density profile in the collisionless regime characteristic to an exosphere. In the first section, the barometric law will be derived from the law of hydrostatic equilibrium and the ideal gas law. In the second section, the transport of the atoms in the collisionless regime is presented in line with the derivation reported by *Chamberlain* (1963), where it is assumed that below the exobase the collisions among the gas atoms maintain a Maxwellian velocity distribution. It will be shown that the barometric law can be used in the exospheric regime as well up to the altitude where the mean kinetic energy per atom remains constant.

A.1 Hydrostatic equilibrium and the barometric law

The temperature, pressure and density in a planetary atmosphere are governed by the equilibrium between the gravitation (acting radially inwards to the planet) and buoyancy (acting radially outwards, due to the pressure gradient). If m and n, respectively, denote the mass of an atom and its number density in a slab of thickness dr, kept under a gravitational field with acceleration due to gravity g, then the pressure (P) at any altitude r is given by

$$\frac{dP}{dr} = -mng \tag{A.1}$$

According to the kinetic theory of gases, the mean kinetic energy of an atom is proportional to its absolute temperature (T). In a system with 3 degrees of freedom, the kinetic energy of a gas with velocity v is given by

$$\frac{1}{2}mv^2 = \frac{3}{2}kT \tag{A.2}$$

Here, k is the Boltzmann's constant.

The expression of pressure exerted by gas atoms in terms of their mean velocity v is given by

$$P = \frac{1}{3}mnv^2 \tag{A.3}$$

Substituting the expression for the mean velocity v from equation A.2 to equation A.3, the expression of pressure comes out as

$$P = nkT \tag{A.4}$$

Equation A.4, which is referred to as the perfect gas law, is, hence, a consequence of the proportionality of the mean kinetic energy of the atoms to the absolute temperature.

Substituting equation A.4 in equation A.1, the hydrostatic equilibrium equation assumes the following form:

$$\frac{dP}{dr} = -\frac{mg}{kT}P \tag{A.5}$$

The pressure P at any arbitrary altitude r is computed by evaluating the following integral

$$\int_{P_0}^{P} \frac{dP}{P} = -\frac{mg}{kT}\int_{r_0}^{r} dr \tag{A.6}$$

Here, r_0 represents the planetary radius or surface of the body and P_0 the pressure at the surface of the planet.

Equation A.6 yields

$$P = P_0\, exp\left(\frac{r - r_0}{kT/mg}\right) \tag{A.7}$$

Equation A.7 is known as the barometric law, which suggests that the pressure falls exponentially with altitude with characteristic height kT/mg, which is called the scale height. The barometric law is derived from the hydrostatic equilibrium and the perfect gas law and is valid irrespective of any information on the distribution function of the gas atoms.

A.2 Exosphere: the collisionless regime

The theory presented here is based on *Chamberlain* (1963). Let us assume a planet and its atmosphere around it in spherical symmetry. Let us further assume that the exobase is at a planetocentric distance of r_c. The evolution of the density function $f(q, p)$ of ensemble

of atoms in the 6 dimensional (3 spatial coordinates $q_{1,2,3}$ and 3 momentum coordinates $p_{1,2,3}$) phase space is described by the Boltzmann transport equation, given by

$$\frac{\partial f}{\partial t} + \nabla_q.(\dot{q}f) + \dot{p}.\nabla_p f \;=\; J_{collision} \tag{A.8}$$

Below the exobase, the velocity of the atoms follow Maxwellian distribution. On the other hand, above the exobase, collisions are absent and the spatial and momentum distribution of the atoms is governed by Liouville's equation, which is equivalent to the Boltzmann transport equation without the collision term. Hence, above the exobase, equation A.8 reduces to

$$\frac{\partial f}{\partial t} + \sum_{i=1}^{3}\left[\frac{\partial f\dot{q}_i}{\partial q_i} + \frac{\partial f\dot{p}_i}{\partial p_i}\right] \;=\; 0 \tag{A.9}$$

The system of atoms are under the influence of the gravitation of the planet. Their velocities and equation of motion are given in terms of the Hamiltonial function H as

$$\dot{q}_i \;=\; \frac{\partial H}{\partial p_i} \tag{A.10}$$

and

$$\dot{p}_i \;=\; -\frac{\partial H}{\partial q_i} \tag{A.11}$$

Expanding each term in the square bracket of equation A.9,

$$\frac{\partial(f\dot{q}_i)}{\partial q_i} \;=\; f\frac{\partial \dot{q}_i}{\partial q_i} + \dot{q}_i\frac{\partial f}{\partial q_i} \tag{A.12}$$

and

$$\frac{\partial(f\dot{p}_i)}{\partial p_i} \;=\; f\frac{\partial \dot{p}_i}{\partial p_i} + \dot{p}_i\frac{\partial f}{\partial p_i} \tag{A.13}$$

Adding equations A.12 and A.13,

$$\frac{\partial(f\dot{q}_i)}{\partial q_i} + \frac{\partial(f\dot{p}_i)}{\partial p_i} \;=\; f\left[\frac{\partial \dot{q}_i}{\partial q_i} + \frac{\partial \dot{p}_i}{\partial p_i}\right] + \dot{q}_i\frac{\partial f}{\partial q_i} + \dot{p}_i\frac{\partial f}{\partial p_i} \tag{A.14}$$

Using equations A.10 and A.11 on the square bracketted terms in equation A.14,

$$f\left[\frac{\partial\left(\frac{\partial H}{\partial p_i}\right)}{\partial q_i} + \frac{\partial\left(-\frac{\partial H}{\partial q_i}\right)}{\partial p_i}\right] \;=\; \frac{\partial^2 H}{\partial q_i \partial p_i} - \frac{\partial^2 H}{\partial p_i \partial q_i} \;=\; 0 \tag{A.15}$$

Thus, equation A.14 reduces to

$$\frac{\partial(f\dot{q}_i)}{\partial q_i} + \frac{\partial(f\dot{p}_i)}{\partial p_i} \;=\; \dot{q}_i\frac{\partial f}{\partial q_i} + \dot{p}_i\frac{\partial f}{\partial p_i} \tag{A.16}$$

Using equation A.16, equation A.9 reduces to

$$\frac{\partial f}{\partial t} + \sum_{i=1}^{3}\left[\dot{q}_i\frac{\partial f}{\partial q_i} + \dot{p}_i\frac{\partial f}{\partial p_i}\right] \;=\; 0 \tag{A.17}$$

Equation A.17 signifies that the density in phase space remains constant along a dynamical trajectory. Under steady state, the time-derivative of the distribution function vanishes and equation A.17 reduces to

$$\sum_{i=1}^{3}\frac{dq_i}{dt}\frac{\partial f}{\partial q_i} \;=\; -\sum_{i=1}^{3}\frac{dp_i}{dt}\frac{\partial f}{\partial p_i} \tag{A.18}$$

Replacing q with r (the planetocentric distance) and p with p_r (radial component of the momentum), equation A.18 assumes the form

$$\frac{dr}{dt}\frac{\partial f}{\partial r} \;=\; -\frac{dp_r}{dt}\frac{\partial f}{\partial p_r} \tag{A.19}$$

The Hamiltonian of the particle in spherical polar coordinate system is given by

$$H \;=\; \frac{p_r^2}{2m} + \frac{P_\chi^2}{2mr^2} - \frac{GM_pm}{r} \tag{A.20}$$

Here P_χ is the angular momentum, m is the mass of the atom, M_p is the mass of the planet and G is the Universal gravitational constant. The equation of motion is given by

$$\dot{p_r} \;=\; \frac{dp_r}{dt} \;=\; -\frac{\partial H}{\partial r} \;=\; \frac{P_\chi^2}{mr^3} - \frac{GM_pm}{r^2} \tag{A.21}$$

Below the exobase, the collisions between the atoms maintain their velocity distribution Maxwellian. Even in the case of Surface Boundary Exosphere, like that of the Moon, the velocities of the thermally desorbed atoms from the surface follow the Maxwellian distribution (*Armand*, 1977). The Maxwellian distribution is given by

$$f(r, p_r, P_\chi) \;=\; \frac{N\, exp\left(-\frac{p_r^2}{2mkT}\right)\; exp\left(-\frac{P_\chi^2}{2mkTr^2}\right)}{(2\pi mkT)^{3/2}} \tag{A.22}$$

where N is the density of atoms at a distance of r. At the exobase, r = r_c, n = N_{ex} and T = T_c. Thus, from equation A.22,

$$\left(\frac{\partial f}{\partial p_r}\right)_{r=r_c} = -\frac{p_r}{mkT_c}\, f \tag{A.23}$$

$$\frac{d(ln\ f)}{dr} = -\left(\frac{GM_p m}{kT_c r^2} - \frac{P_\chi^2}{mkT_c r^3}\right) \tag{A.24}$$

It may be noted that the equation A.24 is independent of p_r. Since the functional dependence of f on p_r does not depend on r, equations A.23 and A.24 are valid for $r > r_c$ (above the exobase) as well.

Expressing the gravitational potential energy $GM_p m/r$ in terms of thermal energy kT_c, a parameter $\lambda(r)$ is envisaged, given by

$$\lambda(r) = \frac{GM_p m}{kT_c r} = \frac{v_{esc}^2}{U^2} \tag{A.25}$$

where $v_{esc} = (2GM_p/r)^{1/2}$ is the escape velocity and $U = (2kT_c/m)^{1/2}$ is the most probable velocity from the Maxwell distribution.

From equation A.24, we get

$$\int_{f_c}^{f} d(ln\ f) = -\int_{r_c}^{r} \left(\frac{GM_p m}{kT_c r^2} - \frac{P_\chi^2}{mkT_c r^3}\right) dr \tag{A.26}$$

where f_c is the Maxwellian distribution at $r = r_c$, which is calculated using equation A.22. Thus the distribution function f at any arbitrary distance r is obtained as

$$f(r, p_r, P_\chi) = \frac{N_{ex}\ exp(-(\lambda_c - \lambda))\ exp\left(-\frac{p_r^2}{2mkT}\right)\ exp\left(-\frac{P_\chi^2}{2mkTr^2}\right)}{(2\pi mkT)^{3/2}} \tag{A.27}$$

The number density at a given altitude r is given by

$$N(r) = \int f(q_i, p_i) d^3 p_i \tag{A.28}$$

If the momenta are independent and can take all values $(-\infty < p_r < \infty\ ;\ 0 < P_\chi < \infty)$, as the case is at lower altitudes (and below the exobase), equation A.28 reduces to

$$N(r) = N_{ex}\ \ exp(-(\lambda_c - \lambda)) \tag{A.29}$$

Equations A.28 and A.29 are the generalized form of the vertical density profile, which resembles the barometric law given by equation A.7.

A.3 Discussion

In the collisionless regime (above the exobase), the vertical distribution of the density of the atoms depends on their energy distribution. The energy distribution of the atoms is Maxwellian below the exobase. The ballistic atoms that are found above the exobase have their velocities distributed as the tail of the Maxwellian, which is an exponential function. As long as the mean kinetic energy per atom is constant, the vertical density profile of atoms display the exponential variation with altitude.

For a given ensemble of thermal atoms in the exosphere, the mean potential energy per atom increases as the particle go up, and hence the mean KE per atom reduces. This is the ideal scenario when the ballistic particle does not undergo any other process which can change their energy state. As the mean kinetic energy per atom decreases at larger altitudes, deviation from the barometric law is observed. *Hurley et al.* (2016), with an example of lunar ^{4}He, has showed that the barometric approximation of the vertical profile matches well with that obtained by Monte Carlo model of the lunar exosphere at altitudes below 200 km. At higher altitudes, deviations are observed from the barometric law, as the mean kinetic energy per atom decreases.

The in-situ observations of the lunar exosphere by CHACE cover the altitude range of 98 km to ground, and hence the barometric law is applicable for the estimation of the density of species at any altitude in that range.

Bibliography

Allegrini, F, MA Dayeh, MI Desai, HO Funsten, SA Fuselier, PH Janzen, DJ McComas, E Möbius, DB Reisenfeld, N Schwadron, *et al.*, Lunar energetic neutral atom (ENA) spectra measured by the interstellar boundary explorer (IBEX), *Planetary and Space Science*, *85*, 232–242, 2013.

Andrews-Hanna, J.C., S.W. Asmar, J.W. Head, W.S. Kiefer, A.S. Konopliv, F.G. Lemoine, I Matsuyama, E Mazarico, P.J. McGovern, H.J. Melosh, and G.A Neumann, Ancient igneous intrusions and early expansion of the Moon revealed by GRAIL gravity gradiometry, *Science*, *339*(6120), 675–678, 2013.

Angerami, J. J., and J. O. Thomas, Studies of Planetary Atmospheres, 1, The Distribution of Electrons and Ions in the Earth's Exosphere, *Journal of Geophysical Research*, *69*, 4537–4560, 1964.

Armand, G, Classical theory of desorption rate velocity distribution of desorbed atoms: Possibility of a compensation effect, *Surface Science*, *66*(1), 321–345, 1977.

Arnold, J R., Ice in the polar regions, *Journal of Geophysical Research*, *86(810)*, 5659–5668, 1979.

Barabash, Stas, Anil Bhardwaj, Martin Wieser, R Sridharan, Thomas Kurian, Subha Varier, E Vijayakumar, Veena Abhirami, KV Raghavendra, SV Mohankumar, *et al.*, Investigation of the solar wind-moon interaction onboard chandrayaan-1 mission with the sara experiment, *Current Science*, *96*(4), 2009.

Beckinsale, R.D., and N.H. Gale, A reappraisal of the decay constants and branching ratio of 40k, *Earth and Planetary Science Letters*, *6*(4), 289 – 294, 1969.

Benna, M., P. R. Mahaffy, J. S. Halekas, R. C. Elphic, and G. T. Delory, Variability of helium, neon, and argon in the lunar exosphere as observed by the LADEE NMS instrument, *Geophysical Research Letters*, *42*, 3723–3729, 2015.

Benson, J., J. W. Freeman, and H. K. Hills, The lunar terminator ionosphere, *Proc. 6th Lunar. Sci. Conf*, pp. 3013–3021, 1975.

Berezhnoy, A A, Chemistry of impact events on the Moon, *Icarus*, *226*, 205–211, 2013.

Beth, A., P. Garnier, D Toublanc, I Dandouras, and C Mazelle, Theory for planetary exospheres: I. Radiation pressure effect on dynamical trajectories, *Icarus*, *266*, 410–422, 2016*a*.

Beth, A., P. Garnier, D Toublanc, I Dandouras, and C Mazelle, Theory for planetary exospheres: II. Radiation pressure effect on exospheric density profiles, *Icarus*, *266*, 423–432, 2016*b*.

Bhardwaj, A, S Barabash, Y Futaana, Y Kazama, K Asamura, D McCann, R Sridharan, M Holmstrom, P Wurz, and R Lundin, Low energy neutral atom imaging on the moon with the sara instrument aboard chandrayaan-1 mission, *Journal of Earth System Science*, *114*(6), 749–760, 2005.

Bhardwaj, A., M. B. Dhanya, A. Alok, S. Barabash, M. Wieser, Y. Futaana, P. Wurz, A. Vorburger, M. Holmström, C. Lue, Y. Harada, and K. Asamura, A new view on the solar wind interaction with the Moon, *Geoscience Letters*, *2*, 10, 2015.

Bishop, J., and J.W. Chamberlain, Radiation pressure dynamics in planetary exospheres: A natural framework, *Icarus*, *81*, 145–163, 1989.

Boss, Alan P, The origin of the moon, *Science*, *231*(4736), 341–345, 1986.

Boss, Alan P, George W Wetherill, and Nader Haghighipour, Rapid formation of ice giant planets, *Icarus*, *156*(1), 291–295, 2002.

Braden, S. E., J. D. Stopar, M. S. Robinson, S. J. Lawrence, C. H. van der Bogert, and H. Hiesinger, Evidence for basaltic volcanism on the Moon within the past 100 million years, *Nature Geoscience*, *7*, 787–791, 2014.

Canup, R. M., Origin of Terrestrial Planets and the Earth-Moon System, *Physics Today*, *57*(4), 56–62, 2004.

Canup, R. M., Forming a Moon with an Earth-like composition via a giant impact, *Science*, *338*(6110), 1052–1055, 2012.

Canup, R. M., Lunar-forming impacts: processes and alternatives, *Philosophical Transactions of the Royal Society of London Series A*, *372*, 20130175–20130175, 2014.

Canup, R. M., and Erik Asphaug, Origin of the Moon in a giant impact near the end of the Earth's formation, *Nature*, *412*(6848), 708–712, 2001.

Canup, R. M., C. Visscher, J. Salmon, and B. Fegley Jr., Lunar volatile depletion due to incomplete accretion within an impact-generated disk, *Nature Geoscience*, *8*, 918–921, 2015.

CHACE Package Assurance Report: ISRO internal report, CHACE Package Assurance Report; ISRO internal report number QDTE/PAR/852/2008, Vikram Sarabhai Space Centre, ISRO, 2008.

Chamberlain, J. W., Planetary coronae and atmospheric evaporation, *Planetary and Space Science*, *11*, 901–960, 1963.

Chapman, J.R., *Practical organic mass spectrometry, 2nd edition*, John Wiley & Sons, Chichester, UK, 1995.

Chaufray, J.-Y., K. D. Retherford, G. R. Gladstone, D. M. Hurley, and R. R. Hodges, Lunar Argon Cycle Modeling, *Lunar Reconnaissance Orbiter Science Targeting Meeting*, vol. 1483 of *LPI Contributions*, 22–23, 2009.

Colaprete, A, M Sarantos, D H Wooden, T J Stubbs, A M Cook, and M Shirley, How surface composition and meteoroid impacts mediate sodium and potassium in the lunar exosphere, *Science*, *351*, 249–252, 2016.

Colaprete, Anthony, Peter Schultz, Jennifer Heldmann, Diane Wooden, Mark Shirley, Kimberly Ennico, Brendan Hermalyn, William Marshall, Antonio Ricco, Richard C Elphic, *et al.*, Detection of water in the lcross ejecta plume, *science*, *330*(6003), 463–468, 2010.

Cook, J. C., and S.A. Stern, Sporadic increases in lunar atmospheric helium detected by LAMP, *Icarus*, *236*, 48–55, 2014.

Cook, Jason C, S. A. Stern, P. D. Feldman, G. R. Gladstone, K.D. Retherford, and Constantine C C Tsang, New upper limits on numerous atmospheric species in the native lunar atmosphere, *Icarus*, *225*, 681–687, 2013.

Crider, D. H., and R. R. Vondrak, Hydrogen migration to the lunar poles by solar wind bombardment of the moon, *Advances in Space Research*, *30*, 1869–1874, 2002.

Crotts, A. P. S., Lunar Outgassing, Transient Phenomena, and the Return to the Moon. I. Existing Data, *The Astrophysical Journal*, *687*, 692–705, 2008.

Ćuk, M., and S. T. Stewart, Making the Moon from a Fast-Spinning Earth: A Giant Impact Followed by Resonant Despinning, *Science*, *338*, 1047, 2012.

Darwin, G. H., On the Precession of a Viscous Spheroid, and on the Remote History of the Earth, *Philosophical Transactions of the Royal Society of London Series I*, *170*, 447–538, 1879.

Dawson, P. H. (Ed.), *Quadrupole mass spectrometry and its applications*, Elsevier scientific publishing company, Amsterdam, Oxford, New York, 1976.

de Pater, I., and J. J. Lissauer, *Planetary Sciences*, Cambridge University Press, Cambridge, UK, 2010.

Dhanya, M B, A Bhardwaj, Y Futaana, M Fatemi, M Holmstroem, S Barabash, M Wieser, P Wurz, A Alok, and R S Thampi, Proton entry into the near-lunar plasma wake for magnetic field aligned flow, *Geophysical Research Letters*, *40*, 2913–2917, 2013.

Dhanya, MB, Anil Bhardwaj, Yoshifumi Futaana, Stas Barabash, Abhinaw Alok, Martin Wieser, Mats Holmström, and Peter Wurz, Characteristics of proton velocity distribution functions in the near-lunar wake from chandrayaan-1/swim observations, *Icarus*, *271*, 120–130, 2016.

Dollfus, A., Polarization of light scattered by solid bodies and natural clouds , *Ann. Astrophysics*, *19*, 83–113, 1956.

Elkins-Tanton, Linda T, Seth Burgess, and Qing-Zhu Yin, The lunar magma ocean: Reconciling the solidification process with lunar petrology and geochronology, *Earth and Planetary Science Letters*, *304*(3), 326–336, 2011.

Elphic, R. C., G. T. Delory, B. P. Hine, P. R. Mahaffy, M. Horanyi, A. Colaprete, M. Benna, and S. K. Noble, The Lunar Atmosphere and Dust Environment Explorer Mission, *Space Science Review*, *185*, 3–25, 2014.

Eugster, O., D. Terribilini, E. Polnau, and J. Kramers, The antiquity indicator argon-40/argon-36 for lunar surface samples calibrated by uranium-235-xenon-136 dating, *Meteoritics and Planetary Science*, *36*, 1097–1115, 2001.

Fastie, W G, P D Feldman, R C Henry, H W Moos, C A Barth, G E Thomas, and T M Donahue, A search for far-ultraviolet emissions from the lunar atmosphere, *Science*, *182*, 710–711, 1973.

Fechtig, H, JB Hartung, K Nagel, G Neukum, and D Storzer, Lunar microcrater studies, derived meteoroid fluxes, and comparison with satellite-borne experiments, *Lunar and Planetary Science Conference Proceedings*, vol. 5, 2463–2474, 1974.

Feldman, P D, and D Morrison, The Apollo 17 ultraviolet spectrometer : Lunar atmosphere measurements revisited, *Geophysical Research Letters*, *18(11)*, 2105–2109, 1991.

Feldman, P. D., D. M. Hurley, K. D. Retherford, G. Randall Gladstone, S. Alan Stern, Wayne Pryor, Joel Wm. Parker, David E. Kaufmann, Michael W. Davis, Maarten H. Versteeg, and LAMP Team, Temporal variability of lunar exospheric helium during January 2012 from LRO/LAMP, *Icarus*, *221*, 854–858, 2012.

Freeman, J. W., and J. L. Benson, A search for gaseous emissions from the Moon, *Phys. Earth Planet. Inter.*, *14*, 276–281, 1977.

Funsten, HO, F Allegrini, PA Bochsler, SA Fuselier, M Gruntman, K Henderson, PH Janzen, RE Johnson, BA Larsen, DJ Lawrence, *et al.*, Reflection of solar wind hydrogen from the lunar surface, *Journal of Geophysical Research: Planets*, *118*(2), 292–305, 2013.

Futaana, Yoshifumi, Stas Barabash, Martin Wieser, M Holmström, Anil Bhardwaj, MB Dhanya, R Sridharan, Peter Wurz, Audrey Schaufelberger, and Kazushi Asamura, Protons in the near-lunar wake observed by the sub-kev atom reflection analyzer on board chandrayaan-1, *Journal of Geophysical Research: Space Physics*, *115*(A10), 2010.

Geiss, Johannes, and Angelo Pio Rossi, On the chronology of lunar origin and evolution: Implications for Earth, Mars and the Solar System as a whole, *Astronomy & Astrophysics Review*, *21*(1), 1 – 54, 2013.

Gibson Jr., E. K., and R. Bustin, Hydrogen Abundances vs. Depth in the Lunar Regolith: Results From an Apollo 15 Double Drive Tube and Deep Drill Core, *Lunar and Planetary Science Conference*, vol. 18 of *Lunar and Planetary Science Conference*, 1987.

Gladstone, G. R., S. A. Stern, K. D. Retherford, R. K. Black, D. C. Slater, M. W. Davis, M. H. Versteeg, K. B. Persson, J. W. Parker, D. E. Kaufmann, A. F. Egan, T. K. Greathouse, P. D. Feldman, D. Hurley, W. R. Pryor, and A. R. Hendrix, LAMP: The Lyman Alpha Mapping Project on NASA's Lunar Reconnaissance Orbiter Mission, *Space Science Review*, *150*, 161–181, 2010*a*.

Gladstone, G Randall, Dana M Hurley, Kurt D Retherford, Paul D Feldman, Wayne R Pryor, Jean-Yves Chaufray, Maarten Versteeg, Thomas K Greathouse, Andrew J Steffl, Henry Throop, *et al.*, LRO-LAMP observations of the LCROSS impact plume, *Science*, *330*(6003), 472–476, 2010*b*.

Goon, A.M., M.K. Gupta, and B Dasgupta, *Fundamentals of Statistics*, The World press Pvt. Ltd., 1968.

Goswami, J.N., and M. Annadurai, Chandrayaan-1: India's first planetary science mission to the Moon, *Current Science*, *96*(4), 486 – 491, 2009.

Grava, C., K. D. Retherford, D. M. Hurley, P. D. Feldman, R. Gladstone, T. K. Greathouse, J. C. Cook, A. Stern, W. R. Pryor, J. S. Halekas, and D. E. Kaufmann, LRO-LAMP Observations of Lunar Exospheric Helium, *AAS/Division for Planetary Sciences Meeting Abstracts*, vol. 47 of *AAS/Division for Planetary Sciences Meeting Abstracts*, 107.12, 2015*a*.

Grava, C., J.-Y. Chaufray, K. D. Retherford, G. R. Gladstone, T. K. Greathouse, D. M. Hurley, R. R. Hodges, A. J. Bayless, J. C. Cook, and S. A. Stern, Lunar exospheric argon modeling, *Icarus*, *255*, 135–147, 2015*b*.

Grava, C., K. D. Retherford, D. M. Hurley, P. D. Feldman, G. R. Gladstone, T. K. Greathouse, J. C. Cook, S. A. Stern, K. E. Mandt, D. E. Kaufmann, W. R. Pryor, and J. S. Halekas, Lunar exospheric helium observations of LRO/LAMP coordinated with ARTEMIS , *Icarus*, *273*, 36 – 44, 2016.

Greeley, R., *Introduction to Planetary Geomorphology*, Cambridge University Press, 2013.

Halekas, JS, AR Poppe, JP McFadden, and K-H Glassmeier, The effects of reflected protons on the plasma environment of the Moon for parallel interplanetary magnetic fields, *Geophysical Research Letters*, *40*(17), 4544–4548, 2013.

Halekas, JS, M Benna, PR Mahaffy, RC Elphic, AR Poppe, and GT Delory, Detections of lunar exospheric ions by the LADEE neutral mass spectrometer, *Geophysical Research Letters*, *42*(13), 5162–5169, 2015.

Harland, W Brian, *A geologic time scale 1989*, Cambridge University Press, 1990.

Hartle, R. E., Model for rotating and nonuniform planetary exospheres, *Physics of Fluids*, *14*(12), 2592–2598, 1971.

Hartle, R. E., and G. E. Thomas, Neutral and ion exosphere models for lunar hydrogen and helium, *Journal of Geophysical Research*, *79*, 1519–1526, 1974.

Hartle, R. E., M. Sarantos, R. M. Killen, E. C. Sittler, J. S. Halekas, S. Yokota, Y. Saito, and W. Farrell, Lunar neutral exosphere properties from pickup ion analysis, *AGU Fall Meeting Abstracts*, p. C1266, 2009.

Hasebe, N, E Shibamura, T Miyachi, T Takashima, M-N Kobayashi, O Okudaira, N Yamashita, S Kobayashi, Y Karouji, M Hareyama, *et al.*, First results of high performance ge gamma-ray spectrometer onboard lunar orbiter SELENE (KAGUYA), *Journal of the Physical Society of Japan*, *78*(Suppl. A), 18–25, 2009.

Heber, Veronika S, *Ancient solar wind noble gases in lunar and meteoritic archives and tests for modern solar wind collection with the GENESIS mission*, Ph.D. dissertation, ETH Zürich, 2002.

Heiken, G. H., D. T. Vaniman, and B. M. French, *Lunar Sourcebook - A user's guide to the Moon*, Cambridge University Press, 1991.

Herring, J R, and A L Licht, Effect of the solar wind on the lunar atmosphere , *Science*, *130*, 206, 1959.

Heymann, D., and A. Yaniv, Ar^{40} anomaly in lunar samples from Apollo 11, *Geochimica et Cosmochimica Acta Supplement*, *1*, 1261, 1970.

Hiesinger, H, JW Head, U Wolf, R Jaumann, and G Neukum, Ages and stratigraphy of mare basalts in oceanus procellarum, mare nubium, mare cognitum, and mare insularum, *Journal of Geophysical Research*, *108*(E7), 2003.

Hinton, F. L., and D. R. Taeusch, Variation of the Lunar Atmosphere with the Strength of the Solar Wind, *Journal of Geophysical Research*, *69*, 1341–1347, 1964.

Hodges, R. R., Helium and hydrogen in the lunar atmosphere, *Journal of Geophysical Research*, *78*(34), 8055 – 8064, 1973.

Hodges, R. R., Formation of the lunar atmosphere, *Moon*, *14*, 139–157, 1975.

Hodges, R. R., Release of radiogenic gases from the moon, *Physics of the Earth and Planetary Interiors*, *14*, 282–288, 1977.

Hodges, R R, Adsorption of exospheric argon-40 in lunar regolith, *Lunar and Planetary Institute Science Conference Abstracts*, vol. 13, 329–330, 1982.

Hodges, R. R., and F. S. Johnson, Lateral transport in planetary exosphere, *Journal of Geophysical Research*, *73*(23), 7307–7317, 1968.

Hodges, R R, Hoffman J H, Yeh T T J, and Chang G K, Helium and hydrogen in the lunar atmosphere , *Journal of Geophysical Research*, *77(22)*, 4079–4085, 1972.

Hodges Jr., R. R., and J. H. Hoffman, Implications of atmospheric Ar escape on the interior structure of the Moon, *Proc. Lunar Sci. Conf., 6th*, 3039–3047, 1975.

Hodges Jr., R. R., J. H. Hoffman, T. T. J. Yeh, and G. K. Chang, Orbital search for lunar volcanism, *Journal of Geophysical Research*, *77*, 4079, 1972.

Hodges Jr., R. R., J. H. Hoffman, F. S. Johnson, and D. E. Evans, Composition and dynamics of lunar atmosphere, *Lunar and Planetary Science Conference Proceedings*, vol. 4 of *Lunar and Planetary Science Conference Proceedings*, 2855, 1973.

Hodges, R Richards., and P. R. Mahaffy, Synodic and semiannual oscillations of argon-40 in the lunar exosphere, *Geophysical Research Letters*, *43*, 22–27, 2016.

Hodges, R.R., J.H. Hoffman, and F. S. Johnson, The lunar atmosphere, *Icarus*, *21*, 415–426, 1974.

Hoffman, J. H., R. R. Hodges Jr., and D. E. Evans, Lunar orbital mass spectrometer experiment, *Lunar and Planetary Science Conference Proceedings*, vol. 3 of *Lunar and Planetary Science Conference Proceedings*, 2205, 1972.

Hoffman, J. H., R. R. Hodges Jr., F. S. Johnson, and D. E. Evans, Lunar atmospheric composition results from Apollo 17, *Lunar and Planetary Science Conference Proceedings*, vol. 4 of *Lunar and Planetary Science Conference Proceedings*, 2875–2875, 1973.

Hoffman, JH, Lunar atmospheric composition experiment. final report, 1 jun. 1971-30 sep. 1975, Texas Univ., Dallas (USA). Richardson Center for Advanced Studies, 1975.

Hoffman, J.H., and R.R. Hodges, Molecular gas species in the lunar atmosphere, *The Moon*, *14*, 159–167, 1975.

Holanda, R., Sensitivity of hot-cathode ionization vacuum gauges in several gases; nasa technical report, nasa-tn-d-6815 e-6759, Lewis Research Center, Cleveland, Ohio, 1972.

Horányi, M, JR Szalay, S Kempf, J Schmidt, E Grün, R Srama, and Z Sternovsky, A permanent, asymmetric dust cloud around the moon, *Nature*, *522*(7556), 324–326, 2015.

Huebner, W. F., and J. Mukherjee, Photoionization and photodissociation rates in solar and blackbody radiation fields, *Planetary and Space Science*, *106*, 11–45, 2015.

Huebner, W. F., J. J. Keady, and S. P. Lyon, Solar photo rates for planetary atmospheres and atmospheric pollutants, *Astrophys. Space Sci.*, *195*, 1–289, 1992.

Hunten, DM, TH Morgan, and DE Shemansky, The Mercury atmosphere, *Mercury*, pp. 562–612, 1988.

Hunten, DM, J-C Gerard, and LM Francois, The atmosphere's response to solar irradiation, *The Sun in time*, vol. 1, 463–497, 1991.

Hurley, D. M, G R. Gladstone, S A. Stern, K. D Retherford, P. D Feldman, W. Pryor, A. F Egan, T. K Greathouse, D. E Kaufmann, A J Steffl, *et al.*, Modeling of the vapor release from the lcross impact: 2. observations from lamp, *Journal of Geophysical Research: Planets*, *117*(E12), 2012.

Hurley, D. M., M. Sarantos, C. Grava, J.-P. Williams, K. D. Retherford, M. Siegler, B. Greenhagen, and D. Paige, An analytic function of lunar surface temperature for exospheric modeling, *Icarus*, *255*, 159–163, 2015.

Hurley, D. M., J. C. Cook, M. Benna, J. S. Halekas, P. D. Feldman, K. D. Retherford, R. R. Hodges, C. Grava, P. Mahaffy, G R. Gladstone, Greathouse T., Kaufmann D. E., Elphic R. C., and Stern S. A., Understanding temporal and spatial variability of the lunar helium atmosphere using simultaneous observations from LRO, LADEE, and ARTEMIS, *Icarus*, *273*, 45 – 52, 2016.

Hurley, D M, J C Cook, K D Retherford, T Greathouse, G R Gladstone, K Mandt, C Grava, D Kaufmann, A Hendrix, P D Feldman, Pryor W, Stickle A, Killen R M, and Stern S A,

Contributions of solar wind and micrometeoroids to molecular hydrogen in the lunar exosphere, *Icarus*, *283*, 31–37, 2017.

Inaba, S., G. W. Wetherill, and M. Ikoma, Formation of gas giant planets: core accretion models with fragmentation and planetary envelope, *Icarus*, *166*, 46–62, 2003.

ISRO internal report: ISRO-VSSC-MIP-PFA-001/2008, MIP Post Flight Analysis (PFA) Document; ISRO internal report number ISRO-VSSC-MIP-PFA-001/2008, Vikram Sarabhai Space Centre, ISRO, 2008.

ISRO internal report: ISRO-VSSC-MIP-TR-001/2007, Environmental Level Specifications for Moon Impact Probe (MIP): ISRO internal report number ISRO-VSSC-MIP-TR-001/2007, Vikram Sarabhai Space Centre, ISRO, 2007.

Jacobson, S. A., A. Morbidelli, S. N. Raymond, D. P. O'Brien, K. J. Walsh, and D. C. Rubie, Highly siderophile elements in Earth's mantle as a clock for the Moon-forming impact, *Nature*, *508*, 84–87, 2014.

Jeans, J., *The dynamical theory of gases*, Cambridge University Press, New York, 1923.

Johnson, F. S., J. M. Carroll, and D. E. Evans, Lunar atmosphere measurements, *Proc. Lunar Sci. Conf. 3rd*, pp. 2231–2242, 1972.

Jordan, A P, T J Stubbs, J K Wilson, N A Schwadron, and H E Spence, The rate of dielectric breakdown weathering of lunar regolith in permanently shadowed regions, *Icarus*, *283*, 352–358, 2017.

Kallenbach, R, FM Ipavich, P Bochsler, S Hefti, D Hovestadt, H Grünwaldt, M Hilchenbach, WI Axford, H Balsiger, A Bürgi, *et al.*, Isotopic composition of solar wind neon measured by celias/mtof on board soho, *Journal of Geophysical Research: Space Physics*, *102*(A12), 26895–26904, 1997.

Kamalakar, J.A., K.V.S. Bhaskar, A.S. Laxmi Prasad, P. Selvaraj, K.R.K. Venkateswaran, A. Goswami, and V.L.N. Sridhar Raja, Lunar Laser Ranging Instrument (LLRI): a tool for the study of topography and gravitational field of the Moon, *Current Science*, *96*, 512–516, 2009.

Killen, R. M., Source and maintenance of the argon atmospheres of Mercury and the Moon, *Meteoritics and Planetary Science*, *37*, 1223–1231, 2002.

Killen, RM, AE Potter, DM Hurley, C Plymate, and S Naidu, Observations of the lunar impact plume from the lcross event, *Geophysical Research Letters*, *37*(23), 2010.

Kim, Y.-K., and M. E. Rudd, Binary-encounter-dipole model for electron-impact ionization, *Physical Review. A*, *50*, 3954–3967, 1994.

Kipp, M. E., and H. J. Melosh, Origin of the Moon: a Preliminary Numerical Study of Colliding Planets, *Lunar and Planetary Science Conference*, vol. 17 of *Lunar and Planetary Science Conference*, 420–421, 1986*a*.

Kipp, M. E., and H. J. Melosh, Short note: A preliminary numerical study of colliding planets, *Origin of the Moon*, 643, 1986*b*.

Kobayashi, S., N. Hasebe, E. Shibamura, O. Okudaira, M. Kobayashi, N. Yamashita, Y. Karouji, M. Hareyama, K. Hayatsu, C. D'Uston, S. Maurice, O. Gasnault, O. Forni, B. Diez, R. C. Reedy, and K. J. Kim, Determining the Absolute Abundances of Natural Radioactive Elements on the Lunar Surface by the Kaguya Gamma-ray Spectrometer, *Space Science Review*, *154*, 193–218, 2010.

Kumar, Ashok, R. V. Ramanan, M. Mohan, B. Sunder, A. Varghese, R. Bagavathiappan, S. Aravamuthan, A. K. A. Samad, K. Ramaswamy, D. Muraleedharan, P. Haridasan, G. Sajitha, Padma, S. Joy, M. J. Lal, K. K. Mukundan, G. SunilKumar, S. R. Biju, B. S. SureshKumar, Rajendran, V. Murugesan, Reshmi, S. Chatterjee, M. Manohar, G. Murali, S. Raghavendran, M. Kalavathi, A. S. K. Kumar, S. A. Kuriakose, S. Paul, A. Verma, R. Sridharan, S. M. Ahmed, P. Sreelatha, T. P. Das, P. P. Kumar, G. Supriya, and Neha Naik, The Moon Impact Probe on Chandrayaan-I, *Current Science*, *96*(4), 540 – 543, 2009.

Lawrence, D. J., W. C. Feldman, B. L. Barraclough, A. B. Binder, R. C. Elphic, S. Maurice, and D. R. Thomsen, Global Elemental Maps of the Moon: The Lunar Prospector Gamma-Ray Spectrometer, *Science*, *281*, 1484, 1998.

Lawrence, D. J., W. C. Feldman, B. L. Barraclough, A. B. Binder, R. C. Elphic, S. Maurice, M. C. Miller, and T. H. Prettyman, High resolution measurements of absolute thorium abundances on the lunar surface, *Geophysical Research Letters*, *26*, 2681–2684, 1999.

Lawrence, D. J., W. C. Feldman, B. L. Barraclough, A. B. Binder, R. C. Elphic, S. Maurice, M. C. Miller, and T. H. Prettyman, Thorium abundances on the lunar surface, *Journal of Geophysical Research*, *105*, 20307–20332, 2000.

Lawrence, David J, Richard S Miller, Martin T Ozimek, Patrick N Peplowski, and Christopher J Scott, High-resolution mapping of lunar polar hydrogen with a low-resource orbital mission, *Acta Astronautica*, *115*, 452–462, 2015.

Leblanc, F., and J.Y. Chaufray, Mercury and Moon He exospheres: Analysis and modeling, *Icarus*, *216*(2), 551 – 559, 2011.

Lodders, Katharina, Solar system abundances and condensation temperatures of the elements, *The Astrophysical Journal*, *591*(2), 1220, 2003.

Lotz, W., Electron-impact ionization cross-sections and ionization rate coefficients for atoms and ions from hydrogen to calcium, *Zeitschrift fur Physik*, *216*, 241–247, 1968.

Manka, R. H., and F. C. Michel, Lunar atmosphere as a source of lunar surface elements, *Lunar and Planetary Science Conference Proceedings*, vol. 2 of *Lunar and Planetary Science Conference Proceedings*, 1717, 1971.

Marty, B., The origins and concentrations of water, carbon, nitrogen and noble gases on Earth, *Earth and Planetary Science Letters*, *313*, 56–66, 2012.

McComas, DJ, F Allegrini, P Bochsler, P Frisch, HO Funsten, M Gruntman, PH Janzen, H Kucharek, E Möbius, DB Reisenfeld, *et al.*, Lunar backscatter and neutralization of the solar wind: First observations of neutral atoms from the moon, *Geophysical Research Letters*, *36*(12), 2009.

Melosh, H. J., and M. Kipp, The giant impact theory of the Moon's origin: a computer simulation, *17th Lunar and Planetary Science Conference*, vol. 592 of *LPI Contributions*, 11, 1986.

Melosh, HJ, and CP Sonett, In origin of the moon, eds hartmann, *WK, Phillips, RJ & Taylor, GJ Lunar and Planetary Institute, Houston*, 1986.

Mitrofanov, I. G., A. B. Sanin, W. V. Boynton, G. Chin, J. B. Garvin, D. Golovin, L. G. Evans, K. Harshman, A. S. Kozyrev, M. L. Litvak, A. Malakhov, E. Mazarico, T. McClanahan, G. Milikh, M. Mokrousov, G. Nandikotkur, G. A. Neumann, I. Nuzhdin, R. Sagdeev, V. Shevchenko, V. Shvetsov, D. E. Smith, R. Starr, V. I. Tretyakov, J. Trombka, D. Usikov, A. Varenikov, A. Vostrukhin, and M. T. Zuber, Hydrogen Mapping of the Lunar South Pole Using the LRO Neutron Detector Experiment LEND, *Science*, *330*, 483, 2010.

Mizuno, H., Formation of the giant planets, *Progress of theoretical physics*, *64*, 544–557, 1980.

Montanari, C C, and J E Miraglia, Electron-impact multiple ionization of Ne, Ar, Kr and Xe, *Journal of Physics B: Atomic, Molecular and Optical Physics*, *47*(10), 105203, 2014.

Montmerle, T., J.-C. Augereau, M. Chaussidon, M. Gounelle, B. Marty, and A. Morbidelli, From Suns to Life: A Chronological Approach to the History of Life on Earth 3. Solar System Formation and Early Evolution: the First 100 Million Years, *Earth Moon and Planets*, *98*, 39–95, 2006.

Mukherjee, N.R., Solar-wind interactions: Nature and composition of the lunar atmosphere, *The Moon*, *14*, 169 – 186, 1975.

Nakai, Y., T. Shirai, T. Tabata, and R. Ito, Cross sections for charge transfer of hydrogen atoms and ions colliding with gaseous atoms and molecules, *Atomic Data and Nuclear Data Tables*, *37*, 69, 1987.

Nakamura, Y., G. V. Latham, H. J. Dorman, A.-B. K. Ibrahim, J. Koyama, and P. Horvath, Shallow moonquakes - Depth, distribution and implications as to the present state of the lunar interior, *Lunar and Planetary Science Conference Proceedings*, vol. 10 of *Lunar and Planetary Science Conference Proceedings*, 2299–2309, 1979.

Noordeh, E., P. Hall, and M. Cuk, Simulating the Phases of the Moon Shortly After Its Formation, *The Physics Teacher*, *52*, 239–240, 2014.

Paige, D. A., M. A. Siegler, J. A. Zhang, P. O. Hayne, E. J. Foote, K. A. Bennett, A. R. Vasavada, B. T. Greenhagen, J. T. Schofield, D. J. McCleese, M. C. Foote, E. DeJong, B. G. Bills, W. Hartford, B. C. Murray, C. C. Allen, K. Snook, L. A. Soderblom, S. Calcutt, F. W. Taylor, N. E. Bowles, J. L. Bandfield, R. Elphic, R. Ghent, T. D. Glotch, M. B. Wyatt, and P. G. Lucey, Diviner Lunar Radiometer Observations of Cold Traps in the Moon's South Polar Region, *Science*, *330*, 479–482, 2010*a*.

Paige, D. A., M. C. Foote, B. T. Greenhagen, J. T. Schofield, S. Calcutt, A. R. Vasavada, D. J. Preston, F. W. Taylor, C. C. Allen, K. J. Snook, B. M. Jakosky, B. C. Murray, L. A. Soderblom, B. Jau, S. Loring, J. Bulharowski, N. E. Bowles, I. R. Thomas, M. T. Sullivan, C. Avis, E. M. de Jong, W. Hartford, and D. J. McCleese, The Lunar Reconnaissance Orbiter Diviner Lunar Radiometer Experiment, *Space Science Review*, *150*, 125–160, 2010*b*.

Paulikas, George A, Carle M Pieters, WB Banerdt, JL Burch, A Chaikin, BA Cohen, M Duke, AW England, H Hiesinger, NW Hinners, *et al.*, The scientific context for the exploration of the moon, *National Research Council, Washington*, *140*, 2007.

Pepin, R. O., Evolution of Earth's Noble Gases: Consequences of Assuming Hydrodynamic Loss Driven by Giant Impact, *Icarus*, *126*, 148–156, 1997.

Pieters, C. M., J. N. Goswami, R. N. Clark, M. Annadurai, J. Boardman, B. Buratti, J.-P. Combe, M. D. Dyar, R. Green, J. W. Head, C. Hibbitts, M. Hicks, P. Isaacson, R. Klima, G. Kramer, S. Kumar, E. Livo, S. Lundeen, E. Malaret, T. McCord, J. Mustard, J. Nettles, N. Petro, C. Runyon, M. Staid, J. Sunshine, L. A. Taylor, S. Tompkins, and P. Varanasi, Character and Spatial Distribution of OH/H_2O on the Surface of the Moon Seen by M^3 on Chandrayaan-1, *Science*, *326*, 568, 2009.

Pollack, J. B., O. Hubickyj, P. Bodenheimer, J. J. Lissauer, M. Podolak, and Y. Greenzweig, Formation of the Giant Planets by Concurrent Accretion of Solids and Gas, *Icarus*, *124*, 62–85, 1996.

Poppe, A R, J S Halekas, M Sarantos, and G T Delroy, The self-sputtered contribution to the lunar exosphere, *Journal of Geophysical Research. : Planets*, *118*, 1934–1944, 2013.

Potter, A. E., and T. H. Morgan, Discovery of sodium and potassium vapor in the atmosphere of the moon, *Science*, *241*, 675–680, 1988.

Saito, Y, S Yokota, T Tanaka, K Asamura, MN Nishino, M Fujimoto, H Tsunakawa, Hidetoshi Shibuya, M Matsushima, H Shimizu, *et al.*, Solar wind proton reflection at the lunar surface: Low energy ion measurement by map-pace onboard selene (kaguya), *Geophysical Research Letters*, *35*(24), 2008.

Sanin, AB, IG Mitrofanov, ML Litvak, BN Bakhtin, JG Bodnarik, WV Boynton, G Chin, LG Evans, K Harshman, F Fedosov, D.V. Golovin, A.S. Kozyrev, T.A. Livengood, A.V. Malakhov, T.P. McClanahan, M.I. Mokrousov, R.D. Starr, R.Z. Sagdeev, V.I. Tretyakov, and A.A. Vostrukhin, Hydrogen distribution in the lunar polar regions, *Icarus*, pp. 20–30, 2017.

Scarborough, J. B., *Numerical Mathematical Analysis*, The Johns Hopkins Press, Baltimore, USA, 1966.

Schmidt, Otto, George H Hanna, and A Lebedinsky, *A Theory of the Origin of the Earth: 4 Lectures*, Lawrence & Wishart, 1959.

Senthil Kumar, P., U. Sruthi, N. Krishna, K. J. P. Lakshmi, R. Menon, Amitabh, B. Gopala Krishna, D. A. Kring, J. W. Head, J. N. Goswami, and A. S. Kiran Kumar, Recent shallow moonquake and impact-triggered boulder falls on the Moon: New insights from the Schrödinger basin, *Journal of Geophysical Research (Planets)*, *121*, 147–179, 2016.

Shemansky, DE, and A Lyle Broadfoot, Interaction of the surfaces of the moon and mercury with their exospheric atmospheres, *Reviews of Geophysics*, *15*(4), 491–499, 1977.

Sigmund, P, Theory of sputtering: I. sputtering yield of amorphous and polycrystalline targets, *Physical Review*, *184*(2), 383–416, 1969.

Singer, S Fred, Origin of the moon by capture, *Origin of the moon*, 471–485, 1986.

Smith, G R, D E Shemansky, A L Broadfoot, and L Wallace, Monte Carlo modeling of exospheric bodies: Mercury, *Journal of Geophysical Research: Space Physics*, *83*(A8), 3783–3790, 1978.

Sridharan, R., S. M. Ahmed, T.P. Das, P. Sreelatha, P. Pradeepkumar, N. Naik, and G. Supriya, Direct evidence for water H_2O in the sunlit lunar ambience from CHACE on MIP of Chandrayaan I, *Planetary and Space Science*, *58*, 947–950, 2010*a*.

Sridharan, R., S. M. Ahmed, T.P. Das, P. Sreelatha, P. Pradeepkumar, N. Naik, and G. Supriya, The sunlit lunar atmosphere: A comprehensive study by CHACE on the Moon Impact Probe of Chandrayaan-1, *Planetary and Space Science*, *58*, 1567–1577, 2010*b*.

Sridharan, R., T. P. Das, S. M. Ahmed, G. Supriya, A. Bhardwaj, and J. A. Kamalakar, Spatial heterogeneity in the radiogenic activity of the lunar interior: Inferences from CHACE and LLRI on Chandrayaan-1, *Advances in Space Research*, *51*, 168–178, 2013*a*.

Sridharan, R, T.P. Das, SM Ahmed, and A Bhardwaj, Indicators for localized regions of heavier species in the lunar surface from CHACE on Chandrayaan-1, *Current Science*, *105*(11), 1470–1472, 2013*b*.

Sridharan, R., S. M. Ahmed, T. P. Das, P. Sreelatha, P. Pradeep Kumar, N. Naik, and G. Supriya, Corrigendum to "The Sunlit lunar atmosphere: A Comprehensive study by CHACE on the Moon Impact Probe of Chandrayaan-1" [Planet. Space Sci. 58 (2010) 1567-1577], *Planetary and Space Science*, *111*, 167–168, 2015.

Stern, S. A., The Lunar atmosphere: History, status, current problems, and context, *Reviews of Geophysics*, *37*, 453–491, 1999.

Stern, S. A., K. D. Retherford, C. C. C. Tsang, P. D. Feldman, W. Pryor, and G. R. Gladstone, Lunar atmospheric helium detections by the LAMP UV spectrograph on the Lunar Reconnaissance Orbiter, *Geophysical Research Letters*, *39*, L12202, 2012.

Stern, S. A, J C Cook, J Y Chaufray, P D Feldman, G. R Gladstone, and K D Retherford, Lunar atmospheric H_2 detections by the LAMP UV spectrograph on the Lunar Reconnaissance Orbiter, *Icarus*, *226*, 1210–1213, 2013.

Stevenson, D. J., Formation of the giant planets, *Planetary and Space Science*, *30*, 755–764, 1982.

Summers, R.L., Empirical observations on the sensitivity of hot cathode ionization type vacuum gauges; nasa technical report, nasa-tn-d-5285, Lewis Research Center, Cleveland, Ohio, 1969.

Taylor, GJ, Crystallizing the Lunar Magma Ocean, *Planetary Science Research Discoveries*, 2011.

Test report on CHACE-FM: ISRO internal report, Test report on chace-fm; isro internal report number qdte/tr/773/2008, Vikram Sarabhai Space Centre, ISRO, 2008.

Thampi, S.V., R. Sridharan, T.P. Das, S.M. Ahmed, J.A. Kamalakar, and A. Bhardwaj, The spatial distribution of molecular Hydrogen in the lunar atmosphere – New results, *Planetary and Space Science*, *106*, 142–147, 2015.

Townsend, PD, Photon-induced sputtering, *Surface Science*, *90*(2), 256–264, 1979.

Trilling, Leon, The interaction of monatomic inert gas molecules with a continuous elastic solid, *Surface Science*, *21*(2), 337–365, 1970.

Urey, Harold C, The capture hypothesis of the origin of the moon, in *The Earth-Moon System*, pp. 210–212, Springer, 1966.

Vondrak, R R., Lunar base activities and the lunar environment, *paper LBS-89-098 presented at Lunar Bases and Space Activities in the 21st century, NASA, Houston, Tex.*, 1988.

Vondrak, R.R., Creation of an artificial lunar atmosphere, *Nature*, *248*, 657–659, 1974.

Vorburger, A., P. Wurz, S. Barabash, M. Wieser, Y. Futaana, C. Lue, M. Holmström, A. Bhardwaj, M. B. Dhanya, and K. Asamura, Energetic neutral atom imaging of the lunar surface, *Journal of Geophysical Research (Space Physics)*, *118*, 3937–3945, 2013.

Vorburger, A., P. Wurz, S. Barabash, M. Wieser, Y. Futaana, M. Holmström, A. Bhardwaj, and K. Asamura, First direct observation of sputtered lunar oxygen, *Journal of Geophysical Research: Space Physics*, *119*, 709–722, 2014.

Vorburger, A, P Wurz, S Barabash, Y Futaana, M Wieser, A Bhardwaj, MB Dhanya, and K Asamura, Transport of solar wind plasma onto the lunar nightside surface, *Geophysical Research Letters*, *43*(20), 2016.

Wang, K, and S B Jacobsen, Potassium isotopic evidence for a high-energy giant impact origin of the moon, *Nature*, *538*(7626), 487–490, 2016.

Wang, X D, Q J Zong, J S Wang, J Cui, H Reme, I Dandouras, C Aoustin, X Tan, J Shen, X Ren, J J Liu, W Zuo, Y Su, W B Wen, F Wang, Q Fu, L L Mu, X Q Wang, L Geng, Z B Zhang, J Z Liu, C L Li, and Z Y Ouyang, Detection of m/q=2 pickup ions in the plasma environment of the Moon: The trace of exospheric H_2^+, *Geophysical Research Letters*, *38*, 2011.

Ward, Stanley H, Gamma-ray spectrometry in geological mapping and uranium exploration, *Economic Geology, 75th Anniversary Volume*, pp. 840–849, 1981.

Warren, Paul H, The magma ocean concept and lunar evolution, *Annual Review of Earth and Planetary Sciences*, *13*, 201–240, 1985.

Weber, R. C., P.-Y. Lin, E. J. Garnero, Q. Williams, and P. Lognonné, Seismic Detection of the Lunar Core, *Science*, *331*, 309, 2011.

Wetherill, G. W., Radioactivity of potassium and geologic time, *Science*, *126*(3273), 545–549, 1957.

Wieczorek, M.A., G.A Neumann, F Nimmo, W.S. Kiefer, G.J. Taylor, H.J. Melosh, R.J. Phillips, S.C. Solomon, J.C. Andrews-Hanna, S.W. Asmar, and A.S. Konopliv, The crust of the Moon as seen by GRAIL, *Science*, *339*(6120), 671–675, 2013.

Wieler, R, Noble gases in the solar system, *Reviews in Mineralogy and geochemistry*, *47*(1), 21–70, 2002.

Wieler, R., and V. S. Heber, Noble Gas Isotopes on the Moon, *Space Science Review*, *106*, 197–210, 2003.

Wieser, M, Barabash S, Y Futaana, M Holmström, A Bhardwaj, R Sridharan, MB Dhanya, P Wurz, A Schaufelberger, and K Asamura, Extremely high reflection of solar wind protons as neutral hydrogen atoms from regolith in space, *Planetary and Space Science*, *57*(14), 2132–2134, 2009.

Williams, J-P, D A Paige, B T Greenhagen, and E Sefton-Nash, The global surface temperatures of the moon as measured by the diviner lunar radiometer experiment, *Icarus*, *283*, 300–325, 2017.

Wilson, J. K., M. Mendillo, and H. E. Spence, Magnetospheric influence on the Moon's exosphere, *Journal of Geophysical Research*, *111*, A07207, 2006.

Wood, John A, Moon over mauna loa-a review of hypotheses of formation of earth's moon, *Origin of the Moon*, 17–55, 1986.

Woolfson, M. M., The Solar - Origin and Evolution, *Q. J. R. astr. Soc.*, *34*, 1993.

Wurz, P., U. Rohner, J. A. Whitby, C. Kolb, H. Lammer, P. Dobnikar, and J. A. Martín-Fernández, The lunar exosphere: The sputtering contribution, *Icarus*, *191*, 486–496, 2007.

Wurz, P., D. Abplanalp, M. Tulej, and H. Lammer, A neutral gas mass spectrometer for the investigation of lunar volatiles, *Planetary and Space Science*, *74*, 264–269, 2012.

Yagi, M., O. Leblanc, J.Y. Chaufray, F. Gonzalez-Galindo, S. Hess, and R. Modolo, Mars exospheric thermal and non-thermal components: Seasonal and local variations, *Icarus*, *221*, 682693, 2012.

Yamashita, N., N. Hasebe, R. C. Reedy, S. Kobayashi, Y. Karouji, M. Hareyama, E. Shibamura, M.-N. Kobayashi, O. Okudaira, C. d'Uston, O. Gasnault, O. Forni, and K. J. Kim, Uranium on the Moon: Global distribution and U/Th ratio, *Geophysical Research Letters*, *37*, L10201, 2010.

Yoder, Charles F. (Ed.), *Astrometric and geodetic properties of Earth and the Solar System*, Wiley Online Library, 1995.

Yokota, S, Y Saito, A Kazushi, T Takaaki, M N Nishino, H Tsunakawa, H Shibuya, M Matsushima, H Shimizu, F Takahashi, M Fujimoto, T Mukai, and T Terasawa, First direct detection of ions originating from the Moon by MAP-PACE IMA onboard SELENE (KAGUYA), *Geophysical Research Letters*, *36*, 2009.

Young, D T, Mass Spectrometry for Planetary Science, *Atmospheres in the Solar System: Comparative Aeronomy Geophysical Monograph 130*, pp. 353–365, 2002.

Zhu, M.-H., T. Ma, and J. Chang, Chang'E-1 gamma ray spectrometer and preliminary radioactive results on the lunar surface, *Planetary and Space Science*, *58*, 1547–1554, 2010.